OPTICAL PROPERTIES OF CERIUM ACTIVATED CALCIUM THIOGALLATE AND STRONTIUM SULPHIDE PHOSPHORS

By

DOROTHY JOHN

A DISSERTATION PRESENTED TO THE GRADUATE SCHOOL
OF THE UNIVERSITY OF FLORIDA IN PARTIAL FULFILLMENT
OF THE REQUIREMENTS FOR THE DEGREE OF
DOCTOR OF PHILOSOPHY

UNIVERSITY OF FLORIDA

1997

to my father Professor M Aruldhas, now with the Lord,
whose selfless and loving, yet uncompromising life, and
faith in God has been my greatest human inspiration.

ACKNOWLEDGMENTS

It is with great pleasure that I thank my advisor, Professor D. B. Tanner, for giving me the opportunity to work in his lab and study the interesting material properties detailed in this dissertation, and for his valuable advice and guidance, constant support, patience and encouragement, all throughout my graduate career at the University of Florida. I also thank my chairman, Professor P. Holloway, for his encouragement and support and Professors R. Hummel, J. H. Simmons, R. Singh and Z. Zhang for their willingness to serve on my supervisory committee, and for reading this dissertation.

I am thankful to C. D. Porter, J. Lavaigne, for their assistance with computer software. I am indebted to Dr. M. Quijada, and Dr. A. Zibold for many enlightening and useful discussions. I would like to extend my thanks to N. L. Tache, Y.-D. Yoon, H. L. Liu, V. Boychev, and S. K. Hong for their friendship, useful conversations and cooperation. The technical support of the staff members in the physics department machine shop is greatly appreciated.

I would like to express my gratitude to Dr. S.-S. Sun and Dr. R. T. Tuenge at Planar Systems, and Dr Balu Pathangey at the University of Florida for providing good quality thin films and Drs J. Kane and P. N. Yocom at the David Sarnoff Research Center for providing single crystals. I also gratefully acknowledge DARPA which supported this research through the PTCOE Grant MDA 972-93-1-0030.

Special thanks to my husband, John, daughter Aksha and son Joshua for their love, care and understanding during my graduate studies. I also thank my loving

mother, who was always supportive and always there for me. She has been a tremendous blessing for me and my children, and will always have a special part in our lives. I am thankful to my brothers, Paul and Jacob, for their constant encouragement, support and practical advice throughout my life.

Above all, I thank Almighty God for meeting all my needs and giving me the peace and joy, that surpasses all human understanding. He is the very reason for my being, and I am grateful for His abiding presence that helped me tackle every problem in my life with His strength and direction, confident that problems are not a sign of His absence.

TABLE OF CONTENTS

Page

ACKNOWLEDGMENTS iii

ABSTRACT viii

CHAPTERS

I. INTRODUCTION 1

- Motivation 3
- Phosphor Materials Studied 5
- Organization of the Dissertation 7

II ELECTROLUMINESCENT PHOSPHORS 8

- Historical Survey 9
- Principle of Operation 10
- Materials in EL Device 12
- Other Physical Properties 18

III OPTICAL THEORY OF THIN FILMS 25

- Determination of Optical Constants 26
  - Kramers Kronig Relations 27
  - Combination of Reflectance and Transmittance 29
- Absorption Spectra 30
  - Bandgap 33
  - Photoluminescence 35
- Optical Constants of Thin Films 36

IV EXPERIMENTAL TECHNIQUES 43

Interferometry 45
Optical Spectrometers 48
  Bruker Interferometer 48
  The Perkin-Elmer Monochromator 50
  Microscope Photometer 53

V OPTICAL STUDIES OF UNDOPED AND CERIUM DOPED CALCIUM THIOGALLATE CRYSTALS 63

Results 64
  Photoluminescence Spectra 64
  Reflectance and Transmittance Spectra 65
  Infrared Spectra 66
  Absorption Spectra and Bandgap 72
Discussion 73

VI OPTICAL STUDIES OF THIN FILMS OF CERIUM DOPED CALCIUM THIOGALLATE 88

Results 89
  Optical Properties of Amorphous Thin Films of Ce:$CaGa_2S_4$ 89
  Optical Properties of Polycrystalline Thin Films of Ce:$CaGa_2S_4$ 90
  Photoluminescence spectra 94
Effective Medium Approximation 94
Discussion 99

VII OPTICAL STUDY OF DEVICE STRUCTURE BASED ON CERIUM DOPED CALCIUM THIOGALLATE THIN FILM 114

Results 115
  Reflectance and Transmittance Spectra 115
Optical Properties Corning 7059 Glass 116
Optical Properties of ITO 117
Optical Properties of ATO 121
Optical Properties of ZnS 123
Photoluminescence Spectra 125
Optical Properties of Multilayers on Glass Substrate 126

Discussion 128

VIII. OPTICAL STUDIES OF THIN FILMS OF CERIUM DOPED STRONTIUM SULPHIDE 153

Results 154
Optical Properties of Ce:SrS on Silicon 154
Optical Properties of CeF$_3$:SrS on Glass 154
Optical Properties of ZnS/Ce:SrS/Glass Structure 158
Discussion 159

IX. SUMMARY AND CONCLUSIONS 172

APPENDICES

A FAR INFRARED STUDIES OF LiAlO$_2$ AND LiGaO$_2$ 177
B OPTICAL PROPERTIES OF Mn:ZnS 192

REFERENCES 200

BIOGRAPHICAL SKETCH 210

Abstract of Dissertation Presented to the Graduate School
of the University of Florida in Partial Fulfillment of the
Requirements for the Degree of Doctor of Philosophy

OPTICAL PROPERTIES OF CERIUM ACTIVATED CALCIUM THIOGALLATE AND STRONTIUM SULPHIDE PHOSPHORS

By

Dorothy John

August 1997

Chairman: Dr. P. Holloway
Cochairman: Dr. D.B. Tanner
Major Department: Materials Science and Engineering

The optical properties of phosphors, such as the optical energy gap, absorption coefficient, refractive index, complex conductivity and complex dielectric function provide fundamental information which is necessary for their applications. There are many ways reported in the literature to determine the optical properties of thin films from reflectance and transmittance data. The classical oscillator method was used in this work, since this method provided good values of optical constants from experimental data. The reflectance and transmittance of single films and of multilayer films deposited on a thick substrate were measured over a wide frequency range, and fit simultaneously with the same parameters.

The first material studied was single crystals of undoped and blue-light emitting cerium doped $CaGa_2S_4$. Polarized optical reflectance measurements were taken over a

frequency range from 30 cm^{-1} to 45000 cm^{-1}. The cerium doped $CaGa_2S_4$ is isotropic due to its polycrystalline nature, whereas the undoped single crystals exhibits a very strong anisotropy in optical properties for light polarized parallel and perpendicular to the c axis. $CaGa_2S_4$ is a direct bandgap material with a bandgap of 4.08 eV.

The optical properties of amorphous and polycrystalline thin films of $Ce{:}CaGa_2S_4$ deposited on a glass substrate were determined by fitting both the reflectance and transmittance spectrum. The band gap of the polycrystalline thin films (4.06 eV) was higher than that of the amorphous thin films (3.61 eV) with a corresponding lower refractive index (2.013 versus 2.172 at 25000 cm^{-1}). An increase in scattering in the far infrared absorption (100 cm^{-1} to 500 cm^{-1}) was observed for granular polycrystalline thin films compared to that of the single crystals.

The optical properties of as-deposited and annealed Ce:SrS thin films were also determined from the reflectance and transmittance spectra. Ce:SrS is an indirect bandgap material with a bandgap of 4.28 eV. Finally, the optical properties of a device structure consisting of layers of indium tin oxide, alumina-titania, and $Ce{:}CaGa_2S_4$ or Ce:SrS were studied. In order to model the reflectance and transmittance of the device structure, the reflectance and transmittance of all the intermediate layers were measured and the optical constants were determined. The bandgap of the device structure was determined to be that of the layer which had the lowest bandgap. Photoluminescence measurements performed on these phosphors showed that they emit blue light when excited with UV photons.

CHAPTER I
INTRODUCTION

This dissertation describes a detailed study of the far infrared through the ultraviolet optical properties, of wide band gap alkaline earth sulphide phosphors. The dissertation concentrates on investigations of single-domain crystals of $CaGa_2S_4$+ Ga_2S_3, a cerium doped polycrystalline $CaGa_2S_4$ + Ga_2S_3 single crystal, as well as thin films and devices based on Ce $CaGa_2S_4$ and Ce:SrS. Measurement and analysis of optical transmittance and reflectance as a function of the incident photon frequency (ω) was performed. Much effort in this work has been devoted to studies of phonons, the refractive index in the visible region and the band gap of the material.

The luminescence of rare-earth ions in a sulphur-dominated lattice has received considerable attention, since these ions substitute for the alkaline earth ions in the host lattice, resulting in phosphors that luminesce strongly under ultraviolet rays.[1] Phosphors consist of a host material and a light emitting dopant called an activator. The activator atoms should be incorporated in a substitutional lattice site for it to emit light without losing its energy non radiatively. The activators dominate the optical emission properties of the phosphor layer and the host material dominates the electrical properties of the phosphor layer.

The system, consisting of a host lattice and an activator, can be characterized by measuring the spectral energy distribution of the emission and excitation.[2] A luminescent material will emit radiation following excitation.[3] The photoluminescence process is as follows. The exciting radiation is absorbed by the activator, raising it to an excited state. The activator returns to the ground state by radiative emission, non radiative emission or a combination of radiative and non-radiative emissions.

The ratio of the radiative and non radiative rates of return to the ground state determines the conversion efficiency of the luminescent material. To create efficient luminescent materials it is necessary to suppress the non radiative process. Good crystallinity of phosphor materials insure that the excited luminescent centers release their energy through a radiative process.[4] High temperature anneals are needed to restore the high degree of crystallinity. Semiconductors with fairly wide bandgaps of 3.5–4.5eV, must be used as the host material, so that the system consisting of a host lattice and the activator, can emit visible light without significant absorption.

Thin film electroluminescent displays are the most reliable and longest lasting flat panel display technology on the market. A thin film is a layer with parallel faces whose thickness d is comparable to the wavelength λ of the electromagnetic radiation it receives. The optical properties of thin films deposited on a thick substrate can provide information on both the device and material characterization. For example, the frequency position of the interference minima and maxima depend on the film thickness and the refractive index. Adjusting the film thickness is an important part of tuning the optical characteristics in the visible region.

Several methods are generally used to determine the complex refractive index and the layer thickness of the thin films. Some of these methods use transmittance at normal incidence (unpolarized light).[5,6] Others use transmittance and reflectance at normal or oblique incidence (polarization measurements),[7–10] or different combinations of them.[11–14] Determination of optical constants proceeds by analysis of reflectance and transmittance. Approaches vary from turning point methods that deal only with minima to maxima, to continuous curve analysis that examine all the data.

The frequency dependent real part of complex conductivity, $\sigma_1(\omega)$, and the real part of complex dielectric function, $\epsilon_1(\omega)$, are directly connected to the absorptive and dispersive nature of a material. In the zero frequency limit, $\sigma_1(0)$ is the ordinary dc conductivity and $\epsilon_1(0)$ is the static dielectric constant. $\sigma_1(\omega)$ and $\epsilon_1(\omega)$ cannot be measured directly. Therefore $\sigma_1(\omega)$ and $\epsilon_1(\omega)$ are calculated from the complex index of refraction $N(\omega)$, which is determined experimentally by measuring the reflectance and transmittance as a function of the energy of the incident light radiation. These quantities provide information on the propagation of radiation and on the electronic structure of solids.[18]

Motivation

The work discussed in this dissertation was motivated by several goals. The study of the optical properties of the phosphor materials is very useful for the design of thin film electroluminescent (TFEL) displays with optimum brightness. The brightness of the emitted light depends on the thickness of the phosphor layer. Minimization of absorption and scattering of emitted light by phosphor particles must be considered in determining the optimum thickness of the phosphor layer. To maximize the emitted light, the internal reflections should be minimized. The internal reflection is a function of the refractive index of the host material, and hence the critical angle θ. Light incident at angles larger than θ are reflected back into the phosphor and is seen as light piping.[16] This light trapping decreases the external luminescence efficiency.

The absorption should be very low in the visible region, so that the light emitted is not absorbed in the material. For the phosphor host materials, absorption is very low between the fundamental absorption edge and the restrahlen region. However addition of impurities or luminescent centers to the host material can introduce absorption bands, which would significantly reduce the light output from these films. One of the goals of this study was to characterize the absorption and emission properties of the phosphor materials. Such characterization is a necessary preliminary for the investigation of electroluminescence.

The value of the optical constants and the film thickness obtained depend on the method used and the model assumed for the film.[17] Values of film thickness obtained by weighing and polarimetric methods using oblique incidence are inaccurate since the method of determining thickness may involve systematic errors.[7] The measured thickness is taken as the true thickness although inaccuracies as high as 5% to 10% are usually obtained. The general problem in determining the thin film optical constants is inversion, i.e., finding the index of refraction and thickness of a given film that brings predicted reflectance and transmittance in agreement with the measured reflectance and transmittance. The algebraic expressions needed for prediction can be extremely complicated even for the simplest thin film configuration. Hence numerical solutions to the inversion problem are regarded as both practical and necessary.[6,10,18,19]

All these numerical schemes require an estimate or guess of the desired optical constants as a starting point in the search routine. Inconsistency in the values of the optical constants occurs because when the equations are solved for the transmittance and reflectance in relation to the unknowns, there are often multiple values of the refractive index and extinction coefficient that give the same values either for the reflectance or transmittance.[9,20,21] Moreover, there may not be a solution in some regions of the spectrum.

The motivation for doing this research is to overcome these difficulties, so that the phosphor materials can be characterized better. The difficulties were overcome in the present study, by a combination of two approaches. First, the reflectance and transmittance were measured over a wide range of frequencies, from the far infrared to the ultraviolet. By extending the measurements to the ultraviolet, valuable information about the electronic transitions and energy levels is obtained. By measuring down to the infrared, reflectance and transmittance were fitted independently using a single set of oscillator parameters.

This oscillator fit method analyzes the whole spectrum simultaneously, and considers the dielectric function as a sum of damped oscillators. This method provides the best measurement of the optical properties of the film. In contrast to the other methods, there is no requirement for an initial guess solution, and there are no missing solutions. The multiparameter curve fitting methods further provide the advantage that the measurement and the fit need not extend beyond the spectral range of interest, unlike the case of Kramers-Kronig analysis, where the single bounce reflectance needs to be known at all frequencies, which is very difficult to handle, since the problem of averaging the phase shift due to imperfect geometry becomes evident. However, for samples with very strong absorption behavior, application of curve fitting methods becomes very difficult.

Phosphor Materials Studied

The host materials studied here were calcium thiogallate ($CaGa_2S_4$), strontium sulphide (SrS), and zinc sulphide (ZnS). Luminescent centers suitable for these host materials were different due to differences in energy band structure of the host materials and the luminescent centers. For calcium thiogallate and SrS, cerium is a common activator, for ZnS, manganese is most common.

Cerium activated calcium thiogallates luminesce in the blue spectral region. Calcium sulphide (CaS) has a bandgap of 4.8 eV while gallium sulphide also possesses a relatively large bandgap of 3.31 eV, and is transparent in the visible region of the spectrum.[1] Cerium compounds exhibit valences of either +3 or +4 with the +4 state no longer having a 4f occupation. The final state reached by electron emission or excitation exhibits a multiple peak structure due to $4f^0$, $4f^1$, and $4f^2$ derived states, from which it has been inferred that the initial state also has a intermediate valence character.[22-26] Cerium has a valence of +3 and $CaGa_2S_4$ is composed of +2 valence sites. This leads to a need for the lattice to achieve charge compensation by forming defects which leads to reduced phosphor performance.

SrS (IIa–VIb compound) thin films are also promising host materials to produce color thin film EL devices.[27,28] Rare-earth ions can be used as the activator for these materials. However, their luminance level and EL efficiency are marginal for practical use, especially for blue colors. To overcome these problems, multilayered thin films of $(SrS:Ce/ZnS)_n$ are made use of, which helps in improving the performance of color EL phosphors.[29] For thin films of ZnS, problems encountered are low solubility of rare earth ions into ZnS lattice and concentration quenching. For SrS thin films chemical instability due to its hydroscopic nature is a major problem.

The general advantages of using various multilayer structure are

1. separation of luminescent layer from ZnS electron acceleration layer,[30]
2. suitable host lattice for rare-earth ions other than ZnS,
3. enhancement of energy transfer probability from electron-hole pairs to luminescent centers.

All the above phosphor materials find application in thin film electroluminescent (TFEL) displays. Electroluminescent displays (ELD) can be classified as light-emitting, totally solid state flat panel displays. Compared with a light emitting diode (LED), an ELD is larger and is easier to view. The cost per pixel is lower. Areas that need improvement are color displays, large multipixel displays, light emitting efficiency etc.[31] In flat panel displays, light is emitted following application of an electric field to a thin film phosphor that is deposited onto a glass substrate or transparent film. They are rugged and easy to handle and have been implemented as planar light sources or graphic displays. ELDs have already had great impact and also have future growth potentials.

Organization of the Dissertation

The organization of this dissertation is as follows: Chapter II presents a review of electroluminescence, the principles of operation of the thin film electroluminescent displays, and other physical properties of the phosphor materials. A brief theoretical background for the understanding of the fundamental and physical properties of a thick crystal, and of thin films on thick substrates is presented in Chapter III. A description of the experimental techniques along with the instrumentation used in this investigation is done in Chapter IV.

The results and discussion pertaining to anisotropy between the ab–plane and c axis optical measurements of $CaGa_2S_4$ crystal, and optical and photoluminescent properties of $Ce:CaGa_2S_4$ phosphors are presented in Chapter V. Chapter VI describes the optical properties of thin films of amorphous and polycrystalline $Ce:CaGa_2S_4$ deposited on a glass substrate, and compares these values with that of the single crystals. Optical properties of devices based on $CaGa_2S_4$ thin films are presented in Chapter VII. Chapter VIII contains the results for the optical properties of Ce:SrS thin films and the influence of annealing on the optical properties of the material, as well as optical properties of Ce:SrS device structure. Summary and conclusions are given in chapter IX.

Appendix A contains far infrared optical properties of $LiAlO_2$ and $LiGaO_2$, which are possible substrates for depositing gallium nitride thin films, and appendix B contains the optical and photoluminescent properties of Mn:ZnS deposited on glass substrate. Appendix A and B present results measured on samples which were not included in the text of this dissertation.

CHAPTER II
ELECTROLUMINESCENT PHOSPHORS

Electroluminescence is defined as the light generated by a phosphor under the influence of an electric field. Electroluminescence (EL) can be either injection electroluminescence or high field electroluminescence. In injection electroluminescence, light energy is released upon recombination of minority and majority carriers across the band gap in a single crystal solid, which is the basis of diodes and diode lasers. In high field electroluminescence, emission is due to impact excitation of luminescent centers by charge carriers which have been accelerated by high electric fields within the solid. The electric fields needed are of the order of 1 MV/cm.[32]

High field EL systems are categorized into two groups: powder samples or thin films. They may be excited either by AC or DC voltages. This variety of EL devices arises from different means of achieving the high field and protecting the device from destructive avalanching currents produced by the high field. Extremely high luminance and long lifetime are the advantages of the film structure over the powder structure. The most stable thin film devices utilize high quality dielectric layers on both sides of the phosphor to limit avalanche currents. Therefore these devices must be operated with AC drive voltages, which also provides longer lifetime, greater power efficiency, greater brightness, and currently, increased capability to provide several colors.[33]

The thin film structures are highly transparent which requires an absorbing rear layer for contrast enhancement.[34] Direct matrix addressing is possible due to the highly nonlinear luminance versus applied voltage for thin film EL. This chapter concentrates on AC driven TFEL systems (ACTFEL).

Historical Survey

EL phenomenon was first discovered by G. Destriau of France in 1936 in Cu:ZnS. ZnS was the host and copper the luminescent center.[35] This discovery led to several efforts to apply EL to lighting. During the 1950s and 1960s extensive research was carried out to fabricate EL displays using phosphors made by fusing Cu:ZnS. These devices, based on powder phosphors, were intrinsically unstable and had limited life-time and low brightness. It has been reported that in deteriorated cells, the brightness can be recovered by heat treatments.[36]

Thin film ACEL were first suggested by Halsted and Koller in 1954.[37] Transparent thin film phosphors were made in 1934 by DeBoer and Dippel[38] and the first thin film EL phosphor based on ZnS was devised by Thornton[39] in the late 50s. The device lasted only for a few hours, since it suffered from very rapid degradation. Hence this work was abandoned at that time.

The most advanced thin film devices developed for display application is the three layer, double insulated, AC coupled, ZnS:Mn thin film device first developed by Soxman[40] in the late 60s. In this configuration, which is shown in Fig. 2.1, the active light emitting layer is sandwiched between two transparent, high dielectric strength layers, and interposed between thin film electrodes on a transparent substrate. Luminance over 50cd/m^2 and several thousands hours of life was reported on this device. Since the rear electrodes were reflective, the contrast ratio was poor.

It was suggested that if the rear electrodes could be made transparent and backed with a diffuse black material or if the second dielectric layer were to be made highly absorbing, the unexcited device could appear black, thus providing good contrast in high ambient illumination. The first thin film EL display with a black layer was produced in the 1960s by Soxman and Steel.[34] Luminance in excess of 160 cd/m^2 was reported on these samples. In 1980, Inoguchi et al. presented data on a three layer thin film ZnS:Mn EL display exceeding 10000 hours of life at 340 cd/m^2.[41] Mito et al[42] presented a second paper describing the reproduction of TV imagery on a 108×81 line TFEL panel, which did not include a black contrast layer. Because they used reflective aluminum rear electrodes with a front mounted circular polarizer for contrast enhancement, the visual performance was marginal.

Preparation of stable thin films was demonstrated by Suntola[43] in 1980, using the atomic layer epitaxy (ALE) for depositing the thin films. Very good quality thin films of ZnS having uniform structure and thickness were produced by the Rohiya Company in Finland. The thin films were produced by the deposition of the metal or the metal compound and the non-metal or the non-metal compound, in very rapid succession. The compounds reacted immediately on the surface leaving a perfect stoichiometric compound. Manganese or manganese compounds could be added during the deposition of ZnS yielding the required Mn:ZnS. At Osaka University, light emission of red, yellow, green and blue colors were obtained by controlling the voltage applied to thin laminated electroluminescent colors.

At present the main effort is directed towards the construction of efficient multicolor displays. Most of the phosphor candidates for the multicolor EL displays are various hosts doped with rare earth elements. Rare earth activated EL materials enable the utilization of sharp intra 4f– shell emissions and activation by minority carriers injection. In 1994 Planar Systems[44] introduced a full color ACTFEL device.

Principle of Operation

A thin film electroluminescent display is made up of a sandwich structure of conductors and dielectrics with a luminescent phosphor in the center as shown in Fig. 2.1. The thin films may be deposited on a glass substrate or non–transparent silicon substrate and viewed through an indium tin oxide transparent conductor. The phosphor layer is sandwiched by dielectrics with high electric breakdown strengths followed by the rear conductor. When a high electric field is applied, the phosphor which is also a dielectric, breaks down into avalanche conduction and current flows through it between the encapsulating dielectric interfaces. As the charge builds up on the dielectric, the internal field in the phosphor is reduced and conduction ceases until the field is reversed. Thus a pulsed avalanche conduction of the phosphor is obtained for each field reversal. The breakdown in the phosphor layer is initiated by electrons tunneling out of dielectric/phosphor interface states into the conduction band of the phosphor layer. With an alternating current drive, there may be two light pulses for each cycle.

The semi insulating phosphor layer has a narrower band gap than its surrounding insulator layers. Applying a voltage across the device raises the energy of electrons on the negative side and reduces the electron energy on the positive side causing a tilt in the whole band gap structure. Any electrons in the conduction band would be accelerated downhill resulting in current flow, but there are too few electrons in the conduction band to result in significant current. Increasing voltages steepen the tilt of the bands until the barrier between these interface states and the conduction band becomes sufficiently thin for electrons to tunnel through the barrier into the conduction band. They enter the conduction band with high energy and are further accelerated by the field until they are sufficiently energetic to impact excite the activator atoms in their path. The build up of electrons at the positive interface reduces the internal field reducing or eliminating tunnelling and conduction to a halt until the voltage is reversed.[33]

At the very high fields involved, the electrons excite the electrons of the activator atoms to high energy states and when they return to the ground state, they give off photons, i.e. luminescence. To prevent destructive breakdown under normal operation, the encapsulating dielectric should not conduct. When breakdown occurs in the encapsulating dielectric layers, a destructive runaway current flows through the entire structure and the stored energy from the surrounding capacitance can discharge through the breakdown area causing failure of the layers to occur. As voltage is gradually applied to a newly fabricated display panel, minute defect areas burn out and clear themselves leaving barely visible dark spots in some of the display element areas.[45] In properly designed and fabricated devices, these cleared defects are stable and do not contribute to further degradation of the panel.

Materials Used in EL Device

Substrate

The major properties to be considered for the substrate are surface characteristics, chemical composition, stability and thermal conductivity. The important surface properties are flatness and micro-finish. Corning 7059 have surfaces comparable to, and better than ground surfaces.[46] The substrates also act as a mechanical film support.

The thin films used in ACTFEL device structure are often deposited on transparent substrates. The composition of the substrates depend on the processing temperatures of the devices. Corning 7059 glass is used for devices processed below 650°C due to its low cost and high availability.[47] For phosphors requiring a high annealing temperature in excess of 650°C glass ceramics are used which are 10 times more expensive than Corning 7059 glass.

Electrodes

The transparent electrode used for the front face of the electroluminescent panel is indium tin oxide (ITO). The high transmittance of ITO permits viewing of the emitted light. ITO is deposited on a glass substrate. The electrode used in the back face should have a low resistivity. This is because when the device is driven at high speed, the speed of response is determined by the product of the electrode resistance and the electrostatic capacity of the pixels. Aluminium is commonly used as the rear electrode since its resistance is low. Aluminium also resists electro-migration, when a high electric field is applied.[45] The contrast of the display is affected since aluminium also reflects any external light that penetrates into the device. This reflected light can be suppressed using interference filters.

Insulators

Insulators should have a high dielectric constant, high electric field strength, uniform thickness and be pinhole free. The dielectric constant and electric field strength are inversely proportional to one another. The figure of merit[46] of insulator materials is the product of dielectric constant and electric field strength. The high dielectric constant materials such as $SrTiO_3$ and $PbTiO_3$ that have the highest figure of merit (19-25 μm/cm) also exhibit propagating breakdown.[47] When breakdown initiates in these materials, it catastrophically spreads and destroys the device. Materials with lower dielectric constant and lower figure of merit are more practical for EL devices due to self healing breakdown that inherently isolates the localized breakdown and prevents catastrophic failure. Below the threshold voltage, which is defined as the maximum voltage which marks the onset of Zener breakdown in the semiconductor phosphor, the applied electric field drop across the insulator versus the phosphor is given by:

$$\epsilon_t E_t = \epsilon_p E_p = \epsilon_b E_b \tag{1}$$

where E is the electric field, ϵ is the dielectric constant and subscripts t, p and b represent the top insulator, phosphor and the bottom insulator, respectively. Since the voltage drop across each layer is the product of the electric field and thickness of each layer, the total voltage drop, V, across the device is given by the following equation.

$$V = E_t d_t + E_p d_p + E_b d_b \tag{2}$$

where d is the film thickness. The dielectric constant of the insulator should be as large as possible and the thickness as small as the device reliability will allow in order to maximize the electric field across the phosphor. As the insulator film become thinner, the pinholes in the films cause localized high-field regions that result in permanent dielectric breakdown. Aluminum oxide/titanium oxide can be used as the insulator since it has a high dielectric strength and reasonable dielectric constant. Other dielectrics with higher dielectric constants exhibit lower dielectric strengths.

Phosphor layer:

Requirements for the ACTFEL phosphors are as follows.[50]

1. Should be possible to excite the material by a high electric field of 10^6V/cm.
2. Behaves like an insulator below threshold voltage for luminescence.
3. Should be possible to dope the host material with an activator, so that it emits light at a desired wavelength.
4. Should be possible to deposit the phosphor in thin film form.

Either the red–green–blue displays (patterned phosphor structure) or the color–by–white display (patterned filter structure) can be used to develop a full color ACTFEL display. For the red–green–blue displays, each pixel contains the red, green or blue phosphor. The dopant/host combinations suitable for red, green or blue light are discussed below. In the color–by–white display, each pixel has a phosphor layer that produces white light that is filtered by a red, green or blue filter

Yellow

Monochrome yellow–black panels based on Mn:ZnS which emits yellow light was commercialized in 1983. Mn:ZnS is the most efficient ACTFEL phosphor having a luminous efficiency greater than 5 lm/W. High solid solubility of Mn^{2+} in ZnS is achieved, since Mn^{2+} ions have the same valence and a similar ionic radius. Thus Mn^{2+} readily substitute for the Zn^{2+} ions, without the need for charge compensators. The optimum Mn concentration for luminance is near 1 mol percent. For higher Mn^{2+} concentration the luminance decreases due to non-radiative decay paths resulting from Mn-Mn interactions. The radiative decay time of the Mn^{2+} emission decreases as the number of non-radiative transitions increase with increasing Mn^{2+} concentration. The emission spectra of Mn:ZnS thin film deposited on a glass substrate is shown in Appendix B.

Red

Eu^{2+} doped CaS and Sm^{3+} doped ZnS were studied as candidates for red phosphors.[81-84] The color purity of both the phosphors were good, but the brightness was too low for practical use. This problem was solved by using Cd(S, Se) filtered ZnS:Mn emission.[85,86] Using the CdS_xSe_{1-x} thin film absorption filter, a luminance over 70 cd/m^2 has been reported at 40 V above threshold and a 60 Hz drive frequency. The filter layer reduces the reflected ambient light by reflecting only red wavelength light, thus increasing the contrast ratio of the red pixels. A contrast ratio of 10:1 was obtained in a 500 lux ambient for a red EL panel operating at 60 Hz without any additional filtering. This eliminated the use of a polarizing filter and a contrast enhancing black layer. The luminance and chromaticity depend on the S/Se ratio and film thickness.

Blue

Tm:SrS and multi-layer structures of $(Tm:ZnS/ZnS)_n$, $(Tm:SrS/ZnS)_n$ and $(Tm:ZnS/SrS)_n$ were studied as possible candidates for blue phosphors.[57] The EL luminance of these phosphors was poor. Ce:SrS is one of the best blue phosphors which has a blue green emission. Pure blue EL emission is obtained by using a blue filter. But 80%-90% of the original luminescence is lost. Even with this loss the luminance level is better than Tm:ZnS. It has been reported that a post deposition anneal of Ce:SrS at 630°C has improved the luminance considerably.[58] A luminance of 10 cd/m^2 has been achieved for ZnS/SrS:Ce multi layer phosphor structure.[59]

Green

Tb:ZnS is the brightest and most efficient green phosphor.[60] ALE deposition of Tb:ZnS has resulted in a phosphor which had a luminance of $70cd/m^2$ at 60 Hz.[61] In Tb:ZnS, Tb^{3+} substitutes for Zn^{2+}, resulting in valence mismatch and ionic radius mismatch. Therefore Tb:ZnS is not as efficient as Mn:ZnS. By introducing oxygen and fluorine in Tb:ZnS the device performance was improved.[62] This improvement was due to better crystallinity, which resulted in a decrease in the non-radiative recombination sites.

Other Physical Properties

ZnS, one of the host materials used in this study, is a II-VI semiconductor having a wurtzite structure. The wurtzite structure is a hexagonal close packed lattice and can be constructed by considering two interpenetrating lattices. The nearest neighbors and the next nearest neighbors are the same in the ideal wurtzite structure. The lattice parameters of ZnS are a=3.814 and c=6.257. For the ideal wurtzite case, c/a=1.633. For ZnS, c/a=1.64. There are four atoms per unit cell, and since the volume per atom is the same, a given volume of reciprocal space contains approximately twice as many reciprocal lattice points.

ZnS can also crystallize in the zinc blende structure. For zinc blende structure shown in Fig. 2.2 there are two atoms per unit cell. If the center of the unit cell is chosen so that the position of each atom of the first type moves to the position of an atom of the second type upon spatial inversion, then the structure factors are real. This can be achieved for both zinc blende and wurtzite.

The band structure of ZnS is shown in Fig. 2.3. ZnS has a direct band structure.[63] The 3d bands of zinc fall in the middle of the sp valence band manifold, particularly in the hetero-polar valence band gap. The conduction band minimum at the Γ point, where it is s- like comes from the 4s wave-function of Zn atoms. The valence band maximum at the Γ point , where it is p- like comes from the 3-p wavefunction of S atoms. The occupied Zn $3d^{10}$ level is located at about 7–8eV below the valence band maximum. When Mn atoms are doped in the ZnS lattice, the Mn $3d^5$ level, which is the ground state of d–d transitions, lies about 3–5eV below the valence band maximum.[64] Therefore the $3d^5$ electron configuration in Mn^{2+} ion is well localized and then isolated from the band electrons. This may be one reason why the Mn^{2+} centers in ZnS are mainly excited by direct impact excitation.

The rare-earth (RE) luminescent centers have a stable trivalent state $(RE)^{3+}$. $(RE)^{3+}$ ions have in common an open $4f^n$ shell which is screened by outer electrons in $5s^25p^6$ closed shells. Hence $4f^n$ electrons of $(RE)^{3+}$ ions in the various host materials are hardly influenced by the crystal field. $(RE)^{3+}$ luminescent centers in ZnS offer a wide variety of emission colors attributed to the 4fn electron configuration.[65] But there is a large difference in ionic radius and chemical nature between the $(RE)^{3+}$ and Zn^{2+} ions. Hence solubility of $(RE)^{3+}$ in ZnS is low, and charge compensation is required due to difference in valence numbers.

The ionic radii of Ca^{2+} or Sr^{2+} ions are considerably greater than that of Zn^{2+} and is comparable to that of the $(RE)^{3+}$ ions. The chemical nature of Ca^{2+} or Sr^{2+} ions is close to that of the $(RE)^{3+}$ ions. The alkaline-earth sulphides are thus preferred over ZnS for rare-earth doping.[66]

SrS has an indirect band structure as shown in Fig. 2.4b. The crystal structure of SrS is shown in Fig 2.3. The conduction band minimum at the X point comes from the wave–function of unoccupied 4d wave–function of the Sr atoms,which is therefore d–like.[67] Just like ZnS, the valence band maximum at the Γ point comes from the 3–p wavefunction of S atoms. When Ce^{3+} centers are doped in the SrS lattice, the 4f ground state level lies in the forbidden gap and 5d excited state lies fairly close to the conduction band minimum at the X point. Therefore, it is expected that the 5d excited state of the Ce^{3+} centers will interact well with conduction electrons and the Ce^{3+} ions are impact excited by the electric field.[68] The electroluminescent spectrum of SrS:Ce device shows blue-green color.

Cerium activated $CaGa_2S_4$ is a bright blue phosphor with sufficient color purity and stability to be used in patterned phosphor full color TFEL panels. A luminance of 10 cd/m^2 at 60 Hz for a sputter deposited $Ce:CaGa_2S_4$ was reported.[44] This luminance level was adequate to use this phosphor as the blue component of an RGB patterned full color TFEL panel.

Calcium thiogallate crystallize in the orthorhombic system with the unit cell parameters $a = 20.086Å$, $b = 20.086Å$ and $c = 12.112Å$ and a space group of the orthorhombic system $Fddd$, $z = 32$. It has a band gap of 2.95 eV and a density of 3370 Kg/m.[69] Studies done on single crystals[70] show that $CaGa_2S_4$ is isostructural. Roques et al.[71] determined the atomic positions for $CaGa_2S_4$ using single crystal X-Ray diffractometer data. The calcium atoms are distributed on three different crystallographic sites 8a, 8b and 16c, having point symmetries 222, 222 and 2 respectively. The gallium and sulphur atoms occupy 32-fold general positions. Calcium atoms are 8-fold coordinated, arranged at the center of square antiprisms of sulphur atoms. Gallium is tetrahedrally coordinated to 4 sulphur atoms, while the sulphur atoms are positioned at the center of the deformed Ca_2Ga_2 tetrahedra.

The crystal structure of calcium thiogallate single crystals is shown in Fig. 2.5. This figure shows the structure in a unit cell, which contains 32 formula units. There are 224 atoms per unit cell. The thiogallate structure can be viewed as planes of atoms normal to the <100> direction. Planes containing only Ca atoms are sandwiched by low density planes of sulphur atoms. High density planes containing calcium, gallium and sulphur atoms are interposed between the low density sulphur planes.[71]

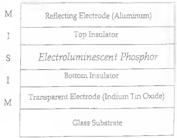
M
Reflecting Electrode (Aluminum)
I
Top Insulator
S
Electroluminescent Phosphor
I
Bottom Insulator
M
Transparent Electrode (Indium Tin Oxide)
Glass Substrate

Fig. 2.1 Schematic diagram of the device structure

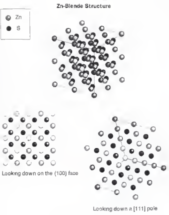

Looking down on the (100) face

Looking down a [111] pole

Fig 2.2. Crystal structure of Zn Blende structure.

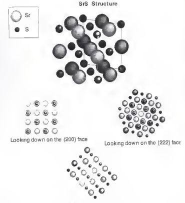
SrS Structure

Looking down on the (200) face

Looking down on the (222) face

Looking down on the (220) face

Fig 2.3. Crystal structure of SrS

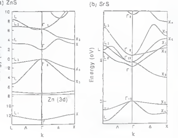

Fig 2.4 Energy band structure of a. ZnS and b SrS (from Ref 29)

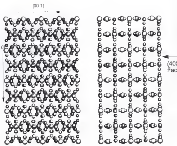

Looking down on the(100) face along the [100]

Looking down the [010]

Fig. 2 5 Crystal structure of $CaGa_2S_4$

CHAPTER III
OPTICAL THEORY OF THIN FILMS

This chapter describes the theoretical background and the techniques of extracting the optical constants of single layers as well as multi-layers, from the measured reflectance $\mathcal{R}(\omega)$ and transmittance $\mathcal{T}(\omega)$. A review of the techniques generally used in obtaining the optical constants of a thick crystal is described followed by the oscillator fit method that was used in this study to obtain the optical constants of thin films on a thick substrate. The details of the optical measurements and the experimental approaches will be given in Chapter IV.

When a beam of light is incident on a material, part of the beam undergoes reflection, part is transmitted through the wafer and the rest of the beam is absorbed in the material. Interaction between photons and electrons or the crystal lattice take place. The nature of this interaction depends on the spectral composition of the light and on the band structure of the semiconductor. When the incident photons interacts with the electrons or ions, electronic transitions take place from occupied states below the Fermi energy (E_F) to unoccupied states above E_F. When the incident photons interact with lattice vibrations, polariton excitations take place.

It is possible to uniquely define the optical properties of a given system by the dielectric response function, $\varepsilon(q,\omega)$, which relates a driven wave of polarization within the solid to a driving electromagnetic wave. The dielectric function depends sensitively on the electronic band structure of a crystal. Studies of the dielectric function by optical spectroscopy are very useful in the determination of the overall band structure of a crystal. In the infrared, visible, and ultraviolet spectral regions the wavevector

q of the radiation is very small compared with the shortest reciprocal lattice vector, and therefore **q** may usually be taken as zero

Determination of Optical Constants of a Thick Crystal

If the crystal is homogeneous, isotropic, linear, and local in its response, the dielectric response may be generally characterized by a frequency-dependent complex dielectric function $\epsilon(\omega)$ which can be written in terms of its real and imaginary parts as

$$\epsilon(\omega) = \epsilon_1(\omega) - i\epsilon_2(\omega) = \epsilon_1(\omega) + \frac{4\pi i}{\omega}\sigma_1(\omega) \tag{3}$$

where the quantity $\epsilon_1(\omega)$ is called the real part of the complex dielectric function and $\sigma_1(\omega)$ is the real part of the complex conductivity. At zero frequency $\epsilon_1(0)$ and $\sigma_1(0)$ becomes the static dielectric constant and the dc conductivity, σ_{dc}, respectively.[72] The dielectric function is not directly accessible experimentally from optical measurements. The directly accessible function is the complex refractive index.[73]

By definition the complex refractive index $N(\omega)$ is related to the refractive index $n(\omega)$, the extinction coefficient $\kappa(\omega)$, and the dielectric function $\epsilon(\omega)$ by

$$N(\omega) = n(\omega) + i\kappa(\omega) = \sqrt{\epsilon(\omega)} \tag{4}$$

The real part of the complex index of refraction $N(\omega)$ is defined as the ratio of the velocities of the electromagnetic wave in vacuum and in the material. When an electromagnetic wave travelling through medium a is normally incident on medium b, the complex amplitude coefficients of the reflected and transmitted electric fields can be determined from the following equations.

$$r(\omega) = \frac{E_r}{E_i} = \frac{N_a - N_b}{N_a + N_b} \tag{5}$$

$$t(\omega) = \frac{E_t}{E_i} = 1 - r = \frac{2N_a}{N_a + N_b} \tag{6}$$

Here $r(\omega)$ is the complex reflectivity coefficient, defined as the ratio of the reflected electric field, E_r, to the incident electric field, E_i, and $t(\omega)$ is the complex transmission coefficient equal to the ratio of the transmitted electric field, E_t, to the incident electric field, E_i. N_a and N_b are the complex refractive indices in medium a and medium b. Since light is usually incident from vacuum onto a sample surface, $N_a = 1$. The power (intensity) reflectance $\mathcal{R}(\omega)$ is then the measured reflectance which is the ratio of the reflected intensity to the incident intensity and is given by:

$$\mathcal{R}(\omega) = rr^* = \rho^2 = \frac{(1-n)^2 + \kappa^2}{(1+n)^2 + \kappa^2} \tag{7}$$

The measured reflectance, $\mathcal{R}(\omega)$, and the phase, $\theta(\omega)$, are related to $n(\omega)$ and $\kappa(\omega)$ by:

$$\sqrt{\mathcal{R}}e^{i\theta} = r = \frac{(1-n) - i\kappa}{(1+n) + i\kappa} \tag{8}$$

where we have separated the amplitude, $\rho(\omega)$, and phase, $\theta(\omega)$, components of the reflectivity coefficient

$$\tan\theta = \frac{-2\kappa}{1 - n^2 - \kappa^2} \tag{9}$$

Kramers-Kronig Relations

By using Kramers-Kronig relations the real part of the response of a linear passive system can be determined if we know the imaginary part of the response at all frequencies and vice versa. It is difficult to measure the phase $\theta(\omega)$ of the reflected wave, but it can be determined using the Kramers-Kronig relations if the single bounce reflectance over a wide frequency range is known.[72-74]

$$\theta(\omega) = \frac{\omega}{\pi}\int_0^\infty \frac{\ln R_s(\omega) - \ln R_s(\acute{\omega})}{\acute{\omega}^2 - \omega^2} d\acute{\omega} \tag{10}$$

Integrating equ.10 by parts, the following equation is obtained.

$$\theta(\omega) = \frac{1}{2\pi}\int_0^\infty \ln\frac{|\acute{\omega} - \omega|}{|\acute{\omega} + \omega|}\frac{d\ln R_s(\acute{\omega})}{d(\acute{\omega})} d\acute{\omega} \tag{11}$$

Eqn.10 shows that far-away spectral regions where $\acute{\omega} \leq \omega$ and $\acute{\omega} \geq \omega$ and regions in which $R_s(\acute{\omega})$ is flat $(dR_s(\acute{\omega})/d\acute{\omega} \approx 0)$ have very small contributions to the integral. Eqn. 11 can be inverted to obtain:

$$n(\omega) = \frac{1 - R_s(\omega)}{1 + R_s(\omega) - 2\sqrt{R_s(\omega)}\cos\theta(\omega)} \tag{12}$$

$$\kappa(\omega) = \frac{2\sqrt{R_s(\omega)}\sin\theta(\omega)}{1 + R_s(\omega) - 2\sqrt{R_s(\omega)}\cos\theta(\omega)} \tag{13}$$

From the real and imaginary part of the complex refractive index, all the other optical constants, namely the complex dielectric function, $\epsilon(\omega) = \epsilon_1(\omega) + i\epsilon_2(\omega)$, the complex conductivity, $\sigma(\omega) = \sigma_1(\omega) + i\sigma_2(\omega)$, absorption coefficient, $\alpha(\omega)$, skin depth, $\delta(\omega)$ and the loss function, -Im$(1/\tilde{\epsilon})$ can be determined from the following equations

$$\begin{cases} \epsilon_1(\omega) = n^2 - \kappa^2 \\ \epsilon_2(\omega) = 2n\kappa. \\ \sigma_1(\omega) = \omega\epsilon_2/4\pi. \\ \sigma_2(\omega) = \omega(1 - \epsilon_1)/4/\pi \\ \delta = c/\omega\kappa. \\ \alpha = 2\omega\kappa/c. \\ -Im(1/\tilde{\epsilon}) = -\epsilon_2(\omega)/(\epsilon_1^2(\omega) + \epsilon_2^2(\omega)) \end{cases} \tag{14}$$

Eqn 10 shows that θ at a single frequency must be determined from R_s at all frequencies and vice versa. In practice, $R_s(\omega)$ can be determined only over a limited frequency range $\omega_1 \leq \omega \leq \omega_2$ Therefore extrapolations beyond the range of the experimental data must be made. The conductivity at frequencies for which there is actual data is not affected significantly by the choice of the low frequency extrapolation. For insulating samples, the reflectance is assumed constant to zero frequency For conducting samples, a Hagen Rubens relation,[75] $R(\omega) = 1 - 2\sqrt{\omega/2\pi\sigma_1(0)}$, is used, which is valid in the far infrared region The high frequency extrapolation has significant influence on the results, primarily on the sum rule derived from the optical conductivity. We terminated the transform above 6 eV by using the reflectance varying as $1/\omega^4$, which is the free electron asymptotic limit

While the Kramers-Kronig method requires that the transmittance or reflectance of the sample be known for a very large spectral region, curve fitting methods provide the advantage that the measurement and the fit need not extend beyond the spectral range of interest The problem is that usually the dispersion relationship of the material investigated is assumed to be known. For samples with dispersion and absorption behavior, the application of curve fitting methods is very difficult.

Combination of Reflectance and Transmittance

The refractive index $N(\omega)$ and the absorption coefficient $\alpha(\omega)$ of a thick crystal can be obtained by measuring the overall transmittance, $\mathscr{T}_x$ and reflectance, $\mathscr{R}_x$ of the material For normal incidence, the equations for $\mathscr{T}_x$ and $\mathscr{R}_x$ of an absorbing material of parallel faces with thickness x are given by the following equations [76]

$$\mathscr{T}_x = \frac{[(1-R_s)^2 + 4R_s \sin^2\theta]e^{-\alpha x}}{[1-R_s e^{-\alpha x}]^2 + 4R_s e^{-\alpha x}\sin^2(\theta+\beta)} \tag{15}$$

$$\mathscr{R}_x = \frac{[1-e^{-\alpha x}]^2 + 4\sin^2\beta e^{-\alpha x}R_s}{[1-R_s e^{-\alpha x}]^2 + 4R_s e^{-\alpha x}\sin^2(\theta+\beta)} \tag{16}$$

where $\beta = n\omega/cx$ and R_s is the single bounce reflectance given by

$$R_s = \frac{(1-n)^2+\kappa^2}{(1+n)^2+\kappa^2} \approx \frac{(1-n)^2}{(1+n)^2} \tag{17}$$

The approximation in the above equation holds when $\kappa = \alpha c/2\omega \ll n$, which is the case for weakly absorbing medium. Equations 15 and 16 incorporate interference effects due to the substrate. In a low resolution measurement, the periodic interference fringes are averaged out. The averages can be found by integrating Eqns. 15 and 16 over $d\beta$, which then reduces to the following form

$$\mathcal{T}_s = \frac{(1 - R_s)^2 e^{-\alpha x}}{1 - R_s^2 e^{-2\alpha x}} \tag{18}$$

$$\mathcal{R}_s = \frac{[1 + (1 - 2R_s e^{-2\alpha x}]R_s}{1 - R_s^2 e^{-2\alpha x}} \tag{19}$$

In the region where the material is transmitting, the single bounce reflectance $R_s(\omega)$ is calculated using equations 18 and 19. This data is then combined with the measured reflectance $\mathcal{R}(\omega)$ in regions of no transmittance, yielding the single bounce reflectance over the whole spectral region. Kramers-Kronig analysis of this single bounce reflectance spectra will yield the optical constants in the entire frequency region measured.

Absorption Spectra

Absorption is the transformation of the energy of the light field into other forms of energy like heat, chemical energy, or electromagnetic radiation which is not coherent, and generally also frequency shifted with respect to the incident beam. The complete absorption spectrum will contain all the energy transfer mechanisms that result from the interaction between light and charges contained in the material. Absorption processes depend on whether the charges are

a. tightly bound, eg. the inner shell electrons of the lattice ions or the lattice ions,

b. loosely bound, eg. the outer shell electrons of the lattice ions,

c. free, eg. the conduction electrons in a metal;

The presence of bound electrons and ions lead to narrow absorption peaks in the ultraviolet and infrared regions of the spectrum. Absorptions corresponding to ionic resonances are referred to as restrahlen absorptions. Absorption by loosely bound charges results from interband excitations. It can only occur between occupied and unoccupied states of energy. This fundamental absorption is characterized by a very broad spectrum since the broad energy bands give a wide choice of transitions.

The Lorentz model is used to describe the bound carrier interband transitions and lattice vibrations. The Lorentz dielectric function ϵ_L can be derived by assuming that the electrons are bound to their cores by harmonic forces and are subjected to viscous damping forces which represent the energy loss mechanism. Then ϵ_L is given by:

$$\epsilon_L = \sum_j \frac{\omega_{pj}^2}{\omega_j^2 - \omega^2 - i\omega\gamma_j}, \tag{20}$$

where ω_j, ω_{pj} and γ_j are the resonant frequency, plasma frequency and damping constant of the j^{th} Lorentzian oscillator. The plasma frequency is defined by $\omega_{pj}^2 = 4\pi N_j e^2/m_j*$, where N_j and m_j* are the number density and effective mass of the bound carriers. Notice that ω_{pj} can also be written as $\sqrt{S_j}\omega_j$, where S_j represents the contribution of the j^{th} oscillator to the static dielectric constant.

From the quantum mechanical point of view, $\hbar\omega_j$ is the transition or gap energy between the initial and excited atomic states, γ_j the inverse life time of the excited carriers or the energy band width due to energy uncertainties in the initial and final excited states. The oscillator strength ω_{pj} is related to the transition probability.

The most important transitions for nonmetallic materials are those between the valence band and the conduction band. Each material is characterized by an energy gap, E_g, so that a minimum photon energy exists which will give excitation resulting in absorption.[77] Below this energy the material is transparent, until the infrared region is reached.

The free electrons in a material are very mobile, interacting readily with an incident electromagnetic wave. Their motion depends on the lattice structure and may interact with a phonon. A loss in energy may result before the charge reradiates the light and hence absorption occurs, which increases with the number of electrons. The absorption coefficient increases as the square of the wavelength becoming more significant in the infrared.

Metals have a very large concentration of free electrons. These electrons lead to free carrier absorption which is large at infrared frequencies. As the frequency increases from the infrared the free carrier absorption decreases, but at ultraviolet frequencies absorption increases again due to the possibility of interband transitions. Depending on the energy band structure of the particular metal, interband and free carrier processes may overlap to give absorption throughout the optical region, or there may be a small window where the absorption is much less.

The Drude model describes the optical response of free carriers in metals. It is a particular case of the Lorentz oscillator, with the resonance frequency equal to zero, since there is on restoring force for free carriers:

$$\epsilon_{Drude} = \frac{-\omega_{pD}^2}{\omega^2 + i\omega/\tau} \tag{21}$$

The Drude plasma frequency is defined by $\omega_{pD}^2 = 4\pi Ne^2/m*$, where N is the charge concentration and $m*$ is the effective mass of the free carriers. The viscous damping mechanism, described by a relaxation time τ, is associated with collisions between electrons (or holes) and impurities or lattice vibrational phonons in metals. The real part of the Drude conductivity is:

$$\sigma_1(\omega)_{Drude} = \frac{1}{4\pi}\frac{\omega_{pD}^2\tau}{1+\omega^2\tau^2} = \frac{\sigma_{dc}}{1+\omega^2\tau^2} \tag{22}$$

The zero frequency limiting value is the dc conductivity, σ_{dc}, defined by

$$\sigma_{dc} = \frac{\omega_{pD}^2 \tau}{4\pi} = \frac{Ne^2\tau}{m*} \tag{23}$$

When $\omega\tau \ll 1$, $\sigma_1(\omega)_{Drude} \rightarrow \sigma_{dc}$ and when $\omega\tau \gg 1$, $\sigma_1(\omega)_{Drude} \propto 1/\omega^2$. Semiconductors possess charges of all kinds, bound and free, so they exhibit some of the optical properties characteristic of each. The most important charges are those associated with the valence band and their excitations by interband transitions to the conduction band.

Bandgap

The difference in energy between the maximum accupied band (valence band) and the minimum of the lowest empty band (conduction band) of a material is defined as the bandgap (E_g) for that material. Band gap measurements consist of measuring the absorption edge. For a direct band gap material the conduction and valence band edges both occur at the same wave vector in the Brillouin zone. This results in an abrupt absorption threshold at the band gap energy. The momentum is automatically conserved and the available optical gain and radiative transition are strong.

For an indirect band gap material, the conduction band edge occurs near the X point and the valence band edge occurs at the zone center. Hence the lowest threshold transition cannot be achieved for a process which involves photons alone. Optical transitions involves phonon or other scattering centers, inorder to conserve momentum and energy.

Photon initiated transitions require a k conserving process inorder that the initial and final states have equal momentum. For indirect transitions in which the k vectors for initial and final states are different, phonon assisted transitions can still conserve momentum. Since three particles (electron, photon and phonon) are involved in an indirect transition, the matrix elements for indirect transitions are much weaker than for direct transitions. Therefore the the band edge absorption is less distinct in indirect band gap materials and the absorption threshold exhibits a long tail into the optical gap region By examining the line shape of the absorption threshold, it is possible to determine whether a gap is direct or indirect [73]

For a direct bandgap material, the energy of an electron in the conduction band is $(\hbar k)^2/2m_e$ and in the valence band is $-E_g-[(\hbar k)^2/2m_h]$, where m_e and m_h are the effective masses for electrons in the conduction band, and holes in the valence band, respectively The total transition rate for electrons excited from the valence band to the conduction band, W_{cv} is given by the following equation [72]

$$W_{cv}=3e^2(2m_r)^{3/2}[2\langle p_{ji}^2\rangle/m\hbar\omega](\hbar\omega-E_g)^{1/2}/m\hbar^2\epsilon_1, \tag{24}$$

where $2\langle p_{ji}^2\rangle/m\hbar\omega$ is an average oscillator strength, and m_r is the reduced mass given by,

$$1/m_r=1/m_e+1/m_h \tag{25}$$

$2m_r=m$, assuming $m_e=m_h=m$

The expression for α is obtained by expressing the power absorption per unit volume as the quantum mechanical transition rate per unit volume, W_{ji}, times the energy $\hbar\omega_{ji}$ absorbed per transition

From Eqn. 25 and the following equation.

$$\alpha_{ji}=\epsilon_1 W_{ji}/nc, \tag{26}$$

the absorption coefficient is obtained as,

$$\alpha_{cv}=3e^2[2\langle p_{ji}^2\rangle/m\hbar\omega][m(\hbar\omega-E_g)]^{1/2}/\hbar^2nc. \tag{27}$$

The bandgap E_g of a material can thus be determined very accurately from the optical absorption coefficient $\alpha(\omega)$ and the incident photon energy, $h\nu$ by using the following equation, which follows from Eqn 26

$$(\alpha h\nu) = (h\nu - E_g)^n \tag{28}$$

For a semiconductor with direct bandgap structure, the value of n is 0.5 and for a semiconductor with an indirect bandgap structure the value of n is 2.[74] This dependence is used to analyze the type of bandgap for different materials.

The bandgap of a ternary compound lies between the energy gaps of its binary compound and is determined by its composition For example, GaAsP has a bandgap between that of GaP and GaAs [79]

Photoluminescence

Optical absorption can give rise to many secondary effects, the majority of which are useful as means for the detection of light The principal processes are photoemission, photoconduction and photoluminescence.[80]

When a material absorbs a photon of energy greater than the bandgap, an electron is promoted to the excited state. Relaxation of the excited state may be characterized as either radiative or nonradiative. An electronic transition from a higher state to a lower state emitting a photon in the process is termed radiative recombination process. This is the reverse process of the photon absorption discussed in the above section.

Optical absorption increases the potential energy of a material as a result of the production of electron-hole pairs or excited impurity ions This state will not last indefinitely, since there is a tendency to revert to the original state. The deexcitation involves the release of energy and this occurs in either or a combination of two ways.

The energy may be transmitted to the lattice as thermal vibrations or be emitted as light. The emission spectra will depend primarily on the nature of the impurity ions which act as the recombination centers.[81-83]

Emission can occur from either an intrinsic band or an impurity level.[84] In band-to-band transition, the electron is promoted to an excited state and the light emitted is reabsorbed. This phenomenon is not generally useful.

Optical Constants of Thin Films on a Thick Substrate

A thin film is a layer with parallel faces whose thickness d is comparable to the wavelength of the electromagnetic radiation it receives. The thin parallel sided film is a special case of a Fabry Perot system of low order. For films whose thickness is of the order of the light wavelength, the path difference introduced are small compared with the coherence length of a monochromatic source. The lateral displacement is $2d\tan\phi$ where ϕ is the angle between the ray in the film and the normal, and is small compared with the breadth of the beam. Therefore the multiply reflected and transmitted beams are regarded as combining coherently.[85]

When a beam of light is incident on a thin film, part of the light is reflected and part of the light is transmitted at the front surface. Fig. 3.1 shows the paths of light rays in multiple reflection between the front and back surface of the thin film. The transmitted part is reflected back and forth between the front and back surfaces as shown in figure. let r be the reflection coefficient and t be the transmission coefficient. If there is no absorption in the thin film, the amplitudes of the successive internally reflected rays are $E_0t, E_0tr, E_0tr^2, \ldots$, and that of the transmitted rays are $E_0t^2, E_0t^2r^2, E_0t^2r^4, \ldots$, where E_0 is the amplitude of the primary ray. The geometric path difference between any two successive transmitted rays is $2d\cos\theta$, where d is the thickness of the thin film and θ is the angle between any internally reflected ray and the surface normal. The corresponding phase difference δ, between any two successive rays is given by:

$$\delta = (4\pi/\lambda) d \cos\theta = (4\pi/\lambda_o) n d \cos\theta, \tag{29}$$

where λ and λ_o are the wavelength in the thin film, and the vacuum wavelength, and n is the refractive index of the thin film, respectively. Summing the amplitudes of the transmitted rays, by taking the phase difference as a factor $e^{i\delta}$, the following equation is obtained.

$$E_T = E_o t^2 + E_o t^2 r^2 e^{i\delta} + E_o t^2 r^4 e^{2i\delta} + \ldots = E_o t^2/(1 - r^2 e^{i\delta}) \tag{30}$$

If the wavelength of the incident light and the thickness of the film are such as to give a phase difference between the reflections of π, then the reflected wavefronts interfere destructively and the overall reflected intensity is a minimum. If the two reflections are of equal amplitude, then the amplitude of this minimum will be zero.

If A is the fraction of the incident energy that is absorbed at each reflection, then by conservation of energy

$$A + R + T = 1 \tag{31}$$

In the absence of absorption or scattering, the lost reflected intensity will appear as enhanced intensity in the transmitted beam, to conserve energy. The sum of the reflected and transmitted beam intensities is always equal to the incident intensity. When the total phase shift between the two reflected wavefronts is equal to zero or multiples of 2π, then the reflected intensity will be a maximum, and the transmitted beam will be reduced accordingly.

In studying the properties of thin films which are supported on a substrate, it is necessary to determine the optical constants of the substrate. The only exception to this requirement is for a heavily absorbing film, for which the attenuation of the light beam in a single transit is virtually complete. In strongly absorbing materials, the transmittance decreases with increasing thickness and does not exhibit oscillations.

Fig. 3.2 shows the case of a single film of thickness l and refractive index n_1 deposited on a thick substrate of refractive index n_T. The amplitude of the electric vector of the incident beam is E_o, that of the reflected beam is $\acute{E}_o$ and that of the transmitted beam is E_T. The electric field amplitude in the film for the forward and backward travelling waves are E_1 and $\acute{E}_1$ respectively.

The electric field E, and magnetic field H, should be continuous at each interface to satisfy the boundary conditions. At the first interface:[56]

$$\begin{cases} E_o + \acute{E}_o = E_1 + \acute{E}_1 \\ H_o - \acute{H}_o = H_1 - \acute{E}_1 \\ n_o E_o - n_o \acute{E}_o = n_o E_1 - n_o \acute{E}_1 \end{cases} \tag{32}$$

At the second interface:

$$\begin{cases} E_1 e^{(ikl)} + \acute{E}_1 e^{(ikl)} = E_T \\ H_1 e^{(ikl)} - H_1 e^{(-ikl)} = H_T \\ n_1 E_1 e^{(ikl)} - n_1 \acute{E}_1 e^{(-ikl)} = n_T E_T \end{cases} \tag{33}$$

The phase factors $e^{(ikl)}$ and $e^{(-ikl)}$ results from the wave travelling a distance l from one interface to the other. Eliminating E_1 and $\acute{E}_1$ from Eqs. 32 and 33, the following equations are obtained

$$1 + \acute{E}_o/E_o = (\cos kl - i(n_T/n_1)\sin kl)(E_T/E_o) \tag{34}$$

In matrix form,

$$\begin{pmatrix} 1 \\ n_o \end{pmatrix} + \begin{pmatrix} 1 \\ -n_o \end{pmatrix} \acute{E}_o/E_o = M \begin{pmatrix} 1 \\ n_T \end{pmatrix} E_T/E_o \tag{35}$$

where, M is the transfer matrix and is given by:

$$M = \begin{pmatrix} \cos kl & -(i/n_1)\sin kl \\ -in_1 \sin kl & \cos kl \end{pmatrix} \tag{36}$$

If there are N layers numbered 1, 2, 3 ... N, having indices of refraction $n_1, n_2, n_3, \ldots n_N$, then the reflection coefficient and transmission coefficients of the multi layer film are related by the following equation

$$\begin{pmatrix} 1 \\ n_s \end{pmatrix} + \begin{pmatrix} 1 \\ -n_s \end{pmatrix} \acute{E}_s/E_s = M_1 M_2 M_3 \ldots M_N \begin{pmatrix} 1 \\ n_T \end{pmatrix} t = M \begin{pmatrix} 1 \\ n_T \end{pmatrix} t, \tag{37}$$

where M_1, M_2, M_3, ... M_N are the transfer matrices of the various layers. M is the overall transfer matrix; r and t can be solved from Eqn. 37

In the present study, two classical models, (Drude and Lorentz) were used to describe the optical properties of the thin films on the thick substrate. The free-carrier component was fit to a Drude model, while the bound carrier interband transitions and lattice vibrations were fit by Lorentzian oscillators. The dielectric function can thus be modelled by a sum of three terms:

$$\epsilon = \epsilon_D + \epsilon_L + \epsilon_\infty \tag{38}$$

where ϵ_D and ϵ_L are the Drude and Lorentz dielectric function, and ϵ_∞ is the contribution from the high frequency absorption beyond the measured range

The experimental reflectance and transmittance data can thus be fitted with a combined Drude–Lorentz model of the following equation to extract the optical parameters:[37]

$$\epsilon(\omega) = \epsilon_1(\omega) + \frac{4\pi i}{\omega}\sigma_1(\omega) = \frac{-\omega_{pD}^2}{\omega^2 + i\omega/\tau} + \sum_j \frac{\omega_{pj}^2}{\omega_{oj}^2 - \omega^2 - i\omega\gamma_j} + \epsilon_\infty \tag{39}$$

where ω_{pD} and $1/\tau$ are the plasma frequency and relaxation rate of the Drude carriers, ω_{oj}, $\omega_{pj}^2/\omega_{oj}^2$, and γ_j are the center frequency, strength, and width of the j^{th} Lorentzian contribution, and ϵ_∞ is the high energy limiting value of $\epsilon(\omega)$ The optical constants obtained by fitting both the reflectance and transmittance is very accurate compared to the other methods of extracting the optical constants, namely the fringe analysis method etc. The thickness of the thin films can also be accurately determined, since thickness is an input parameter for fitting the measured data.

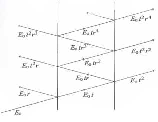

Fig. 3.1. Paths of light rays in multiple reflection between the front and back surface of the thin film.

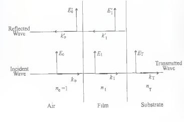

Fig. 3.2 Wave vectors and their associated electric fields for the case of normal incidence of a thin film deposited on a thick substrate.

CHAPTER IV
EXPERIMENTAL TECHNIQUES

This chapter describes the experimental methods and spectrometers used in the measurement of reflectance and transmittance at near normal incidence over a wide frequency range, from about 20 cm^{-1} to 48,000 cm^{-1} (2.5 meV–5.95 eV). The complete spectrum of a given source comprises all the frequencies that the source emits. Since no single universal frequency resolving instrument exists, the various regions of the electromagnetic spectrum was investigated by using a variety of optical spectrometers, light sources and detectors. Table. 4.1 shows the electromagnetic spectrum in the infrared, visible and ultraviolet region, expressed in frequency, wavelength and photon energy.

The spectrometers used to measure the optical spectra of the samples in the far-infrared (20–600 cm^{-1}) and mid-infrared (500–3,000 cm^{-1}) region was a fast-scan Model 113v Bruker Fourier-Transform Interferometer. A Perkin Elmer 16U Grating Monochromator, and a MPM 800 Microscope Photometer were used to collect data at higher frequencies of 1000–40,000cm^{-1}). The Microscope Photometer was also used to measure the photoluminescence of the phosphor samples.

The optical constants of solids can in principle be determined in two ways, either from intensity measurements (unpolarized light) or from polarization measurements (oblique incidence). The former can be performed either at normal or near normal incidence or at oblique incidence. Advantages of measuring reflectance and transmittance at near normal incidence are:[88]

1. The data analysis is relatively easy.

Table. 4.1 The electromagnetic spectrum expressed in frequency, wavelength and photon energy

Region	Frequency (cm^{-1})	Frequency (THz)	Wavelength (nm)	Photon energy (eV)
Far IR	24-298	0.75-9	400,000-33,000	0.003-0.037
Mid IR	298-2,226	9-67	33,000-4,500	0.037-0.276
Near IR	2,226-12,825	67-385	4,500-780	0.276-1.59
Red	12,825-16,051	385-482	780-622	1.59-1.99
Orange	16,051-16,777	482-503	622-597	1.99-2.08
Yellow	16,777-17,342	503-520	597-577	2.08-2.15
Green	17,342-20,326	520-610	577-492	2.15-2.52
Blue	20,326-21,939	610-659	492-455	2.52-2.72
Violet	21,939-25,650	659-769	455-390	2.72-3.18
Near UV	25,650-50,000	769-1500	390-200	3.18-6.20
Vacuum UV	50,000-250,000	1,500-7,500	200-40	6.20-31.0

2. The reflectance in most cases is insensitive to any polarization introduced by the monochromator

3. The reflectance is insensitive to the angle of incidence for angles within about 10° of normal incidence.[19]

For nearly all materials the average of the reflectances measured parallel and perpendicular to the plane of incidence, differed by less than ±0.0001 from that at normal incidence, even for angles as large as 10°. Thus, reflectance measurements made at nearly normal incidence were insensitive to both the convergence angle of the incident radiation and the average angle of incidence.

Interferometry

Fourier-transform spectroscopy is a valuable tool in the far infrared where the signal to noise ratio with conventional spectrometers is very poor.[30] An interferogram is the output of an interferometer as the optical path difference is varied. The interferogram is the Fourier-transform of the spectrum of the input radiation. High photometric accuracy is essential for precise measurements of optical properties. The photometric accuracy of spectra measured by using FTIR is determined by the temperature stability of the interferometer, source and detector, detector linearity and the technique of sampling and data processing.[31]

The principle of the FTIR is based on the Michelson interferometer shown in Fig. 4.1. The electromagnetic radiation emitted from the source is focused onto the beamsplitter, which divides this light into two beams. One beam is reflected and the other is transmitted. The reflected beam is reflected by a stationary mirror back to the beam splitter and the transmitted beam is reflected back to the beamsplitter by a moveable mirror. These two beams recombine in the beamsplitter and is sent into the sample chamber and then into the detector. When the two-sided mirror moves at a constant speed, v, a path difference $x = 4vt$ is introduced, where t is the time since the mirror is at the zero-path difference position. The intensity of the radiation reaching the detector versus the optical path difference represents the interferogram of the radiation emitted by the source.

The interferogram is written as

$$I(x) = I_{\infty} + \int_{-\infty}^{\infty} S(\omega) e^{(-i2\pi x\omega)} d\omega \qquad (40)$$

where x is the path difference, $S(\omega)$ is the spectral distribution function and I_∞, the intensity at infinite path difference is called the dc level. For the ideal case, $I(x)$ is symmetric about $x=0$, where x varies from $-\infty$ to $+\infty$. Sampling is carried out continuously as a function of path difference. If the light is a monochromatic wave, of wavenumber ν_o so that

$$S(\nu) = S_0(\delta(\nu - \nu_o) + \delta(\nu + \nu_o)) \tag{41}$$

then, Eq. 40 gives

$$I(t) = I_0 \cos 2\pi f_a t \tag{42}$$

where $I_0 = 2S_0$ and $f_a = 4v\nu_o = (4v/c)f_o$

The spectrum itself can be found by integrating the inverse Fourier transform of the interferogram.

$$S(\omega) = \int_{-\infty}^{\infty} (I(x) - I(\infty))e^{(i2\pi\omega x)} dx \tag{43}$$

The digital data is transferred into the Aspect computer system and is Fourier-transformed into a single-beam spectrum as shown in Fig. 4.3, after corrections such as apodization and phase correction.[92,93]

The advantages of Fourier-transform spectrometers are due to the major concepts known as the Fellgett advantage and the Jacquinot advantage. An interferometer measures information from the entire range of a given spectrum during each time element of a scan, whereas a conventional grating spectrometer measure only that part of the spectrum which passes through the exit slit of the instrument. Fellgett emphasized that FTIR spectrometers utilize less time than conventional spectrometers to measure all the spectrum, and so this measurement is characterized by better signal/noise ratio. This advantage is called the Fellgett advantage.[94]

The ability of interferometers to collect large amounts of energy at high resolution is called the throughput advantage or the Jacquinot advantage of interferometers over spectrometers.[96] In addition, Fourier transform spectroscopy has several advantages over conventional grating based spectroscopy including stability, the ability to easily average multiple scans, high wavenumber accuracy, absence of stray light and high scan rate.[96]

It is impossible to measure a continuous interferogram over a infinite path difference. Instead, a finite number of discrete points up to some maximum path difference x_m is sampled so that the Fourier integral is replaced by a Fourier series. Truncation of the interferofram at $x = \Delta$ introduces distortions in sharp features of the computed spectrum. In addition, the finite maximum path difference approximation introduces sidelobes near sharp spectral structures, if the central peak falls between two calculated points.[96] These sidelobes are introduced in the wings of unresolved lines by the $\sin(2\pi\nu\Delta)/(2\pi\nu\Delta)$. This problem can be overcome by applying the apodization technique, which removes the side lobes.[95] This is done by multiplying the interferogram by the apodization function, $A(x, \Delta)$, which goes to zero at $x = \Delta$, and is zero for x greater than Δ. The cost of this procedure is a further line broadening and loss of resolution. Another issue, caused by the discrete sampling, is the aliasing effect which must be reduced by using some cut-off filters to suppress the high frequency components, and by choosing the sampling interval in accordance with the Nyquist criterion, $x \leq (\lambda_{max}/2)$, where $(\lambda_{min}/2)$ is the shortest wavelength.[96]

If the interferogram is not symmetric about its central position, the result is a phase error. This translates into $S(\omega)$ becoming complex in the spectral distribution function which is unreasonable. In order to eliminate the phase error, the zero path difference of the movable mirror should be accurately determined and phase correction techniques employed.

Optical Spectrometers

Bruker Interferometer

The reflectance and transmittance measured in the far infrared region is obtained by using an IBM-Bruker fast scan Fourier transform interferometer (FTIR). The principle of this interferometer is that of a Michelson interferometer, although there are some modifications.[37] The frequency range covered is 20–5,000 cm^{-1}.

Fig. 4.2 shows the FTIR which is divided into four chambers: the source, interferometer, sample and the detector chambers. The sample chamber contains two identical channels, one for reflectance and the other for transmittance measurements. For reflectance measurements, an optical stage, shown in the top part of Fig. 4.2 is placed in the sample chamber. The entire system is evacuated to avoid H_2O and CO_2 absorption during measurements. An Hg arc lamp is used as the source in the far infrared (20–700 cm^{-1}) and a globar source is used in the mid infrared (400–5,000 cm^{-1}).

Eqns. 42 and 43 shows that the optical frequency of the radiation, f_o, is reduced by a factor of $4v/c$. Hence the detector sees a signal with an audio frequency f_a instead of the much higher optical frequency f_o. This signal is amplified by a wide-band audio preamplifier and then digitized by a 16-bit analog-to-digital converter. The weak infrared signals requires a high sensitivity detector. The detectors used in the far infrared region is a liquid helium cooled 4.2 K Si bolometer and in the mid infrared region a liquid helium cooled 4.2 K Si:B photocell or a room temperature pyroelectric deuterated triglycine sulfate (DTGS) detector. The liquid helium cooled detectors have much better signal-to-noise (S/N) ratio as compared with the DTGS. The bolometer system consists of three main parts: detector, liquid helium (LHe) dewar, and preamplifier.

Fig. 4.4 shows the schematic diagram of the bolometer detector mounting and the LHe dewar (HD-3). A diffusion pump reduces the pressure in the dewar to $\sim 10^{-6}$ torr, after which it is pre-cooled with liquid nitrogen for about an hour. The nitrogen can is filled with nitrogen. The pre-coolant is then removed and the liquid helium is transferred into the helium can to maintain the detector at 4.2 K. A temperature as low as 1.2 K can be achieved by reducing the vapor pressure above the liquid helium. A thermal radiation shield is placed between the helium can and the case to reduce the head load on the cold area. The Si detector is mounted on a cold surface under the helium can. The optical signal is guided by the pipe along the optical axis through a window (polyethylene for FIR, KRS-5 for MIR) and optical filters before it finally arrives at the detector. The output electric signal from the detector is amplified and sent to the A/D converter of the Bruker interferometer.

Table 4.2 shows the parameters used in the Bruker spectrometer.

Table 4.2 Bruker FTIR Operating Parameters

Range cm^{-1}	Beam Split. Material	Opt. Filt. Material	Source Material	Pol.	Detect
35-90	Mylar	Black PE	Hg arc	1	bolometer
80-400	Mylar	Black PE	Hg arc	1	bolometer
100-600	Mylar	Black PE	Hg arc	1	bolometer
450-4,000	Germanium on KBr	none	Globar	2	DTGS, photocell

PE = polyethylene. Polarizer 1 = wire grid on oriented polyethylene; polarizer 2 = wire grid on AgBr

Perkin-Elmer Monochromator

Optical spectra from midinfrared through the visible and ultraviolet (UV) frequencies of 1,000–40,000 cm^{-1} (0.12–5 eV) were measured using a model 16U Perkin-Elmer (PE) monochromator. At these frequencies, the Fellgett advantage diminishes due to the availability of stronger sources and more sensitive detectors. Therefore a grating spectrometer is an excellent choice at frequencies in the near infrared, visible and UV regions. Fig. 4.5 shows the layout of the modified Perkin-Elmer 16U monochromator. The three light sources that are used are a globar source for the midinfrared, a quartz tungsten lamp for the near infrared, and a deterium arc lamp for the UV region. The measurements were done in vacuum to prevent water absorption.

The light from the source was passed through a chopper and a series of filters. The chopper generates a square wave signal for lock in detection. The filters reject the unwanted higher order diffraction from the grating, which occur at the same angle as the desired first-order component. The light beam passes through an exit slit, into a grating where the different wavelengths are diffracted according to the formula:

$$2d\sin\theta = n\lambda \tag{44}$$

where n is the n^{th} order of the diffracted light, (n=1 here) λ is the wave length, θ is the angle of incidence, and d is the spacing between the grating lines. The angle of incidence is changed at predetermined intervals consistent with the necessary spectral resolution by rotating the grating with a stepper motor controller. This allows access to different wavelengths sequentially. The steps in angle of rotation together with the exit slit width determine the resolution of the monochromator.[98] Increasing the slit widths increases the intensity of the emerging radiation (higher S/N ratio) at cost of lower resolution.

Mirror M_1 is a reference mirror which can be rotated or replaced by a sample for reflectance measurements. For transmission measurements, the sample is mounted in a sample rotator, as indicated in Fig. 4.5. The positions of the sample on the rotator and of the detector are the two focal points of an ellipsoidal mirror. Three detectors are used to cover the different photon energy regions are a thermocouple used in the region 0.11–0.9 eV, a lead sulphide (PbS) photoconductor for the region, 0.5–2.5 eV, and a silicon photodiode in the region 2.2–5 eV. Table. 4.3 lists the parameters used to cover each frequency range.

The electric signal from the detector is amplified by an Ithaco model 393 lock in amplifier. The output signal from the lock in system is then averaged over a given time interval and converted into digital data by an integrating digital voltmeter.

In order to resolve the dielectric tensor along the principal axes of the single crystals used in this work, the electric field of the light was polarized. Since the radiation generated at the source is randomly polarized, the polarization of the light was accomplished by inserting a polarizer in the path of the beam. The characteristics of the polarizers vary depending on the frequency range of interest. In the infrared, the polarizers used were made of a gold wire grid, vapor deposited on a substrate. For the midinfrared spectral range (300–4,000 cm^{-1}) a silver bromide substrate was used, while in the far infrared (30–600 cm^{-1}), the substrate was polyethylene.

Dichroic and plastic polarizers were used in the near infrared, visible and UV. In both the Bruker and Perkin-Elmer spectrometers, the desired polarization of the light was achieved by mounting the polarizer in the path of the beam using a gear mechanism that also allowed rotation from the outside without breaking the vacuum in the spectrometers. This in situ adjustment of the polarizers greatly reduced the uncertainty in the relative anisotropy of the reflectance (better than ±0.25%). This

Table 4.3 Perkin Elmer Grating Monochromator Parameters

Frequency (cm^{-1})	Grating[a] (line/mm)	Slit width (micron)	Source[b]	Detector[c]
891–965	101	2,000	GB	TC
905–1,458	101	1,200	GB	TC
1,403–1,752	101	1,200	GB	TC
1,644–2,612	240	1,200	GB	TC
2,467–4,191	240	1,200	GB	TC
4,015–5,105	590	1,200	GB	TC
4,793–7,977	590	1,200	W	TC
3,829–5,105	590	225	W	PbS
4,793–7,822	590	75	W	PbS
7,511–10,234	590	75	W	PbS
9,191–13,545	1,200	225	W	PbS
12,904–20 144	1,200	225	W	PbS
17,033–24,324	2,400	225	W	576
22,066–28,050	2,400	700	D_2	576
25 706–37,964	2,400	700	D_2	576
36,386–45,333	2 400	700	D_2	576

[a] Note the grating line number per cm should be the same order of the corresponding measured frequency range in cm^{-1}

[b] GB Globar; W Tungsten lamp; D_2 Deuterium lamp

[c] TC Thermocouple; PbS Lead sulphide; 576 Silicon photocell

was specially important when the relative anisotropy in the optical response of the crystal was not very large.

MPM 800 Microscope Photometer

The MPM 800 Microscope Photometer is a system for spot measurement, area scan and spectral scan using a grating monochromator from the UV to the NIR region, to measure transmittance, reflectance and photoluminescence spectra. The corresponding grating monochromators disperse light from a frequency of 4,100 cm^{-1} to 48,000 cm^{-1}. The microscope photometer offers major convenience of operation by retroreflection of the measuring diaphram into the binocular tube and electrical switching between observation and measurement.

Measurement spot size on the sample is selected by a variable rectangular diaphram which has a minimum spot size of 1 μm. Independent of the spot size the spectral bandwidth may be selected from 1 to 20 nm. The system comprises of an illumination side monochromator to provide incident light. Polarising optics are available for the frequency region, from 4,100 cm^{-1} to 1,200 cm^{-1}. The second VIS/IR monochromator at the detector side covers the range upto 48,000 cm^{-1} and may be used for transmittance and reflectance spectra. The spectral resolution is 1nm and the smallest diaphram allows a spatial resolution of 1 μm. The software can handle an electronic scanning stage which enables multi point spectral scans at preprogrammed sample areas for statistical evaluation.

Fig. 4.8 shows the MPM 800 Microscope Photometer for photoluminescence measurements. The xenon lamp is used a the source of optical excitation. The light from the xenon lamp illuminates the sample via the incident light path, through a blue filter or an UV filter exciting the electrons in the valence band to the conduction band, so that they are in a non equilibrium state. When the electrons return to the lower energy states, through radiative recombination, photons of various energies are emitted The emitted light is analyzed by a the second monochromator to obtain the photoluminescence spectrum.

Increasing the numerical aperture (N A) of the objective leads to an increase in luminescence intensity by $(N.A.)^4$ The object spectra was corrected to eliminate any system specific effects The light path which has to be corrected is the emission pathway, beginning at the objective, passing the monochromator and terminating at the photomultiplier (path I in fig 4 6) This is done by measuring light path II separately The basic formula for calculation of spectral correction for photoluminescence measurements at wavelength λ is

$$Q(\lambda) = \frac{O(\lambda) - P(\lambda)}{S(\lambda)} \times R(\lambda) \tag{45}$$

where

Q (Quotient) is the luminescence spectra after spectral correction.

O (Object) is the measured value of the luminescence intensity

S (Standard) is the measured value of the tungsten light source

P (Parasitic) is the measured value of the parasitic light

R (Reference) is the calculated data for the theoretical spectral properties of the standard.

Fig 4 7 shows the beam path of MPM 800 Microscope Photometer for transmitted and reflected light Reflectance and transmittance can be measured within a selected spectral range at fixed wavelength intervals and at selected object points. A xenon lamp is used as the light source in the spectral range 4,000 cm^{-1} to 12,000 cm^{-1} and a tungsten lamp is used from 11,800 cm^{-1} to 45,000 cm^{-1} The detector is a photomultiplier tube (PMT). The detector amplifier, scanning stage, monochromator, light shutters and diaphragms and order-sorting filters for grating monochromators are all software controlled. The basic formula for calculation of spectral correction for transmittance measurements at wavelength λ is

$$Q(\lambda) = \frac{O(\lambda)}{S(\lambda)}. \tag{46}$$

The basic formula for calculation of spectral correction for reflectance measurements at wavelength λ is:

$$Q(\lambda) = \frac{O(\lambda) - P(\lambda)}{S(\lambda) - P(\lambda)} \times R(\lambda). \tag{47}$$

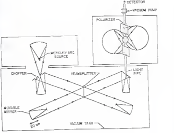

Fig. 4.1 Schematic diagram of the Michelson interferometer.

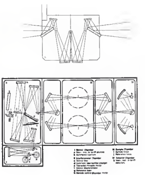
I Source Chamber
a Near-, mid- or far-IR sources
b Automatic aperture
II Interferometer Chamber
c Optical filter
d Automatic beamsplitter changer
e Two-sided movable mirror
f Control interferometer
g Reference laser
h Remote control Chamber motor
III Sample Chamber
i Sample focus
j Reference focus
IV Detector Chamber
k Near-, mid- or far-IR detectors

Fig. 4.2. Schematic diagram of the IBM IR/98 BRUKER interferometer. The top part of the figure (enlarged scale) is an optical stage setup for measuring reflectance

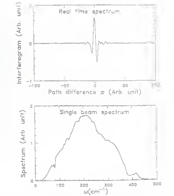

Fig. 4.3 The interferogram $D(x)$ (upper panel), and its Fourier transformation $S(\nu)$ (lower panel) measured by a fast-scanning Bruker interferometer. (Note we have used ω instead of ν to label the frequency axis for all figures throughout this dissertation for consistency.)

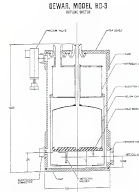

Fig 4 4 Schematic diagram of a bolometer detector. The dimensions are in inches

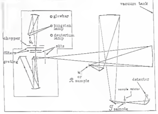

Fig. 4.5 Schematic diagram of the Perkin-Elmer monochromator spectrometer.

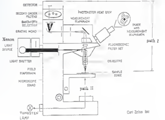

Carl Zeiss Inc

Fig 4 6 MPM 800 Microscope Photometer for photoluminescence measurements

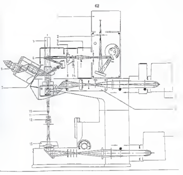

Schematic beam path of MPM 800 Microscope Photometer for transmitted and reflected light

1 Detector unit PMT with/without PbS cell
2 Grating monochromator
3 Motorized filter changer
4 Intermediate image plane with measuring diaphragms
5 TV/photo port
6 Switching mirror TV/measurement
7 Beam splitter in photometer tube
8 Image-forming beam path of measuring diaphragms
9 Intermediate image plane in eyepiece
10 Objective
11 Specimen
12 Condenser
13 Luminous field diaphragm for transmitted light
14 Pilot lamp
15 HBO illuminator with fast shutter
16 Aperture and luminous field diaphragms for reflected light
17 Halogen illuminator with light shutter

Fig. 4.7 Schematic beam path of MPM 800 Microscope Photometer for transmitted and reflected light

CHAPTER V

OPTICAL STUDIES OF UNDOPED AND CERIUM DOPED CALCIUM THIOGALLATE CRYSTALS

In this chapter, the optical properties of undoped single crystals of $CaGa_2S_4$ and $CaGa_2S_4$ doped with 6 mole % cerium, for light polarized parallel and perpendicular to the c axis is discussed. The room temperature reflectance, $\mathcal{R}(\omega)$, and transmittance, $\mathcal{T}(\omega)$, was measured over a wide frequency range of 30–48,000 cm^{-1} (4 meV–5.95 eV). In the region where the material was transmitting the optical constants were obtained by the inversion of equations for reflectance and transmittance. The single bounce reflectance in this region was then combined with the single bounce reflectance in the region where the material was non-transmitting. Kramers-Kronig analysis was performed on these single bounce reflectance spectra, to obtain the optical conductivity and other optical constants.

An extensive optical study was done on the infrared dynamics of the single crystals. There are two kinds of information available from a study of the optical properties of a crystal at lattice vibrational frequencies, which are the forces coupling the sublattices together, determined from the resonant frequencies and the apparent charges of the sublattices determined from the resonant strengths. This is done by calculating a theoretical reflectivity using a set of oscillator parameters and adjusting it to produce as good a fit as possible to the measured reflectance.

In addition to this, the influence of doping on the photoluminescence spectra of the single crystals was also studied. This was done by studying the absorption spectra and the emission spectra when the single crystals are excited with ultraviolet radiation. From the optical absorption spectra, the band gap energy was determined

Material synthesis

The phosphor was prepared by J Kane and P N Yocom at the Sarnoff Corporation The phosphor powder was prepared by firing a mixture of calcium sulphide, gallium sulphide and cerium sulphide in the appropriate stoichiometric quantities at 940 °C A small quantity of the phosphor powder was placed on a polished sapphire wafer and heated in a quartz tube in a hydrogen sulphide/nitrogen atmosphere to a temperature above the melting point The furnace was cooled slowly at 3°/minute in the region of the melting point The single crystals prepared in the above manner does not adhere to the sapphire

Results

Photoluminescence Spectra

The emission spectra for the unactivated and cerium activated phosphors when excited with uv light at 365 nm is shown in Fig 5.1 The unactivated phosphor exhibited photoluminescence but not electroluminescence. The intensity of the light emitted was very low resulting in a noisy spectra. Tiny holes could be seen on the surface of the crystallized sample, when viewed through the optical microscope. The material inside these holes appeared to be a Ga-poor, S-rich compound, or a mixed phase which was responsible for the light emission. The emission spectra of the cerium activated phosphor showed overlapping double bands which has a peak intensity at 475 nm (2 61 eV) This energy is characteristic of the radiative transition from the ^2D excited state of the cerium atom to the $4f(^2F_{5/2})$ ground state, and the low energy shoulder is due to the ^2D-$^2F_{7/2}$ electronic transition

The cerium atom ground state configuration is $(Kr)4d^{10}4f^{1}5d^{1}6s^{2}$ where the Ce^{3+} ion has the configuration $(Kr)4d^{10}4f^{1}$ When excited, the $4f^1$ electron is excited into the empty 5d level which leads to the d to f transition.[18] The outermost shell is the 5d, and the excited electron is referred to as the unshielded electron. Unshielded electrons can be influenced by the surrounding environment, which is the crystal field effect. The emission peaks from such activators tend to be broad and shift as a function of its host environment.[100]

Fig. 5.2 shows the absorption and broad emission spectra of the cerium activated thiogallate phosphor. The absorption spectrum shows a maximum at 425 nm which corresponds to the absorption of cerium into its excited ^2D energy level. This maximum absorption value is obtained from the Kramers Kronig analysis of the reflectance spectrum, which is the single bounce reflectance spectrum since there was no transmittance at this wavelength. Below 380 nm the absorption again increases since the spectrum approaches the bandedge. An overlap is observed between the excitation and emission spectra, which attenuates the cerium emission. One reason for the large shift to longer emission peak wavelengths observed for the cerium activated thiogallates could be selective absorption of the shorter emission wavelengths by the cerium ion with subsequent reemission at longer wavelengths. The emission band is located at longer wavelengths than are generally observed for cerium in oxide hosts. This spectral shift is a consequence of the nephelauxetic effect.[101]

Reflectance and Transmittance Spectra

Fig. 5.3 a and b shows the room temperature reflectance for light polarized parallel to the c axis and perpendicular to the c axis, respectively, for a 45 μm thick unactivated $CaGa_2S_4 + Ga_2S_3$ single crystal. Between 100 cm^{-1} and 400 cm^{-1}, the reflectance is dominated by phonon modes. The results show a very strong anisotropy in the phonon region between the two directions of polarization. From the crystal structure, we see that the lattice parameters are different along the a–b plane and c axis, which shows that this anisotropy is not surprising. The low frequency results are characterized by a reflectance that is higher along the c axis by 10–15%

Fig. 5.4 a and b shows the room temperature transmittance of the unactivated single crystals for light polarized parallel to the c axis and perpendicular to the c axis, respectively. The transmittance is essentially zero for the single crystal in the phonon region. The transmittance spectrum shows strong absorption bands below 1,200 cm^{-1}, which is the absorption due to water molecules. This result shows that calcium thiogallate single crystals are hygroscopic in nature. In the mid infrared region, the transmittance decreases drastically and in the visible region the transmittance is very low. This is because the unactivated $CaGa_2S_4$ + Ga_2S_3 single crystals looked very cloudy and there is considerable amount of scattering within the single crystals.

Fig. 5.5 a and b shows the reflectance and transmittance the Ce^{3+} doped $CaGa_2S_4$ + Ga_2S_3 phosphor for light polarized parallel and perpendicular to the c axis, respectively, in the uv/visible region of the spectrum (300—700nm). A very strong absorption can be seen between 405 nm and 445 nm which is the absorption of cerium into its excited ^2D energy level. Below this energy the material is transparent. This absorption is also seen in the reflectance spectrum of the doped sample. The emission band for cerium is located at longer wavelengths than are generally observed for Ce^{3+} in oxidic hosts.

The reflectance and transmittance spectra for the undoped single crystals shown in fig. 5.4 do not show any absorption at this frequency, indicating the absence of cerium. A luminescent material will emit radiation only when the excitation energy is absorbed. Hence only the doped phosphor emits light, since it absorbs energy.

Infrared Spectra

The atoms in a crystal are not static, but are in constant motion about their average position. The vibrational energy associated with any given atomic displacement cannot be isolated in one cell, and the resulting lattice vibration wave is called a phonon.

If there are N atoms in a unit cell, there are 3N different vibrational excitations possible. This is due to the fact that three independent vector components are necessary to specify the displacements of every atom from its average position. When two or more branches cross at some point, the vibrations involved are different. Only the excitation energies associated with them happen to be the same. There are always three branches which provide the mechanism for the transmission of sound waves through the crystal. These are the acoustic branches. The remaining 3N−3 branches describe the optic phonon modes.

Fig. 5.6 shows the real part of optical conductivity in the far infrared region for the unactivated calcium thiogallate single crystals. Kramers-Kronig analysis of the single−bounce reflectance spectrum was done by following the high and low frequency extrapolation as described in Chapter III, to obtain the conductivity. The phonon modes were seen more clearly in the conductivity spectra. Kramers−Kronig analysis revealed that the conductivity is dominated by a total of six infrared−active modes each along the a−b plane and c axis. The results indicated a ratio in the far-infrared conductivity of roughly 2:1, with the higher value corresponding to the c axis. The dashed line shows the conductivity, obtained from the Kramers-Kronig analysis, and the solid line shows the Drude Lorentzian fit on the conductivity.[102]

The intensity ω_{pj} in each phonon line is related to the effective charge that is carried by each ion. In addition these intensities are also related to the splitting between the transverse optical (TO) and longitudinal optical (LO) phonon frequencies. Since the TO frequencies involve transverse vibrations of the atoms, they were obtained directly from the peak position in the absorption, as the peak position in the real part of optical conductivity. Table. 5.1 shows the oscillator parameters and the TO and LO phonon frequencies for the undoped $CaGa_2S_4 + Ga_2S_4$ single crystals, for light polarized parallel and perpendicular to the c axis, respectively, with an accuracy of ± 0.1 cm^{-1}

Low frequency modes are made up of the vibrations due to heavier atoms and high frequency modes are made up of the vibrations due to lighter atoms. In the optical conductivity spartra shown in Fig. 5.6, for the undoped single crystals, the phonon mode centered at 380 cm^{-1}, for light polarized parallel to the c axis, and 374 cm^{-1} for light polarized perpendicular to the c axis were due to the stretching of the sulphur atom. The phonon mode centered at 206 cm^{-1}, for light polarized parallel to the c axis, and 204 cm^{-1} for light polarized perpendicular to the c axis were due to vibrations of the calcium atoms. The triple mode at 308 cm^{-1}, 321 cm^{-1}, and 338 cm^{-1}, for light polarized parallel to the c axis, and 295 cm^{-1}, 320 cm^{-1} and 338 cm^{-1}, for light polarized perpendicular to the c axis were due to the bending of the Ga_2S_3 tetrahedron. The phonon mode centered at 276 cm^{-1}, for light polarized parallel to the c axis, and 274 cm^{-1}, for light polarized perpendicular to the c axis were the vibrations of the gallium atoms.

Fig. 5.7 shows the real part of dielectric constant in the far infrared region. The static dielectric constant of the undoped single crystals were 10.8 and 8.24 for light polarized parallel to the c axis and perpendicular to the c axis, respectively. A quantitative analysis of the intensity and linewidth of each phonon mode led to a model of the reflectance using a dielectric function consisting of six Lorentz oscillators given by equation 20 plus a core dielectric constant ϵ_∞ to account for contributions at higher frequencies.

Fig. 5.8 shows the far−infrared loss function for the unactivated single crystals obtained from the Kramers Kronig analysis. LO frequencies involve long−range changes in the dipole moment along the direction of phonon propagation in the crystal. In

Table. 5.1. Parameters of Lorentz fit to the far infrared reflectance of $CaGa_2S_4 + Ga_2S_4$ single crystals, for light polarized parallel and perpendicular to c axis.

Oscillators	ω_{pj} (cm^{-1})	$\omega_j(\omega_{TO})$ (cm^{-1})	γ_j (cm^{-1})	ω_{LO} (cm^{-1})
c axis	94	129.2	3.5	131.2
	67	139.8	4	141.8
	40	149.9	5	–
	50	190.3	200	–
	420	205.9	15	244.9
	180	276.3	10	284
	205	307.6	6	313.9
	160	320.6	6	329.3
	150	336	6	352
	160	380.4	10	407.6
a–b plane	32.6	120	1.7	122.5
	58.3	150	4.2	158.6
	50.7	155.6	113	171.6
	78.6	203.5	3.5	212.6
	720.3	180	1771.6	212.6
	116.6	294.6	6	303.6
	104.6	319.7	15.4	323
	51.4	338	2.9	347
	135.6	374	7.5	381.9

formation about the center frequencies of these LO oscillations were obtained from the peak positions in the loss function. The Lyddane–Sachs–Teller relation, which is given below, was used in determining the TO–LO splitting in lattice vibrations

$$\omega_{pj}^2 = (\omega_{jL}^2 - \omega_{jT}^2)\epsilon_\infty \tag{48}$$

Eqn. 48 is valid only for single or independent oscillators. For multi-phonon materials, a least square fit to the reflectance data using the following factorized expression for $\epsilon(\omega)$ was performed.

$$\epsilon(\omega) = \epsilon_\infty \prod_{j=1}^{6} \frac{\omega_{jL}^2 - \omega^2 + i\gamma_{jL}\omega}{\omega_{jT}^2 - \omega^2 - i\omega\gamma_{jT}} \tag{49}$$

The fitting procedure was started by first determining the TO frequencies from the peak maxima of $\sigma_1(\omega)$and using equation 1. After determining and fixing all the TO frequencies, the reflectance data were fitted using a program that minimized $\chi^2 \sim (R - R_{fit})^2$ by adjusting the other parameters in Equ. 20. The TO and LO frequencies should be next to each other with the TO frequency heving a lower value. For light polarized parallel to the c axis, since the TO mode at 206 cm^{-1} carries most of the spectral weight, the corresponding LO mode was at a much higher frequency.

Fig. 5.9 a and b shows the reflectance in the far infrared region and the real part of dielectric constant for light polarized parallel to the c axis and perpendicular to the c axis, respectively, for the cerium activated calcium thiogallate phosphor. Due to the polycrystalline nature of the cerium activated phosphor, only isotropic properties were observed for polarized measurements in the sample. Kramers–Kronig analysis revealed that the conductivity was dominated by a total of 18 infrared–active modes. Fig. 5.10(a) shows the real part of conductivity and and Fig. 5.10(b) shows the loss function. The dashed line shows the conductivity obtained from the Kramers Kronig analysis and the solid line shows the Drude/Lorentzian fit on the conductivity

Table 5.2. Parameters of Lorentz fit to the far infrared reflectance of Ce $CaGa_2S_4 + Ga_2S_4$ phosphor.

Oscillators	ω_{pj} (cm^{-1})	$\omega_j(\omega_{TO})$ (cm^{-1})	γ_j (cm^{-1})	ω_{LO} (cm^{-1})
	50	107.5	10	108
	74	120.5	4	124
	59	129	3.2	131
	60	140	4	142
	79	150	5.8	153
	62.5	157	5.8	160
	424	186	2290	190
	211	206	8.3	216
	193	224	18	250
	125	232	21	250
	165	276	12	284
	172	295	10.5	304
	130	309	8	314
	145	319	6.4	326
	177	335	9.9	335
	150	365	4700	364
	250	375	16	373
	80	380	10	425

Table 5.2 shows the oscillator parameters and the TO and LO phonon frequencies for the cerium doped Ce $CaGa_2S_4 + Ga_2S_4$ phosphor

For the doped phosphors the phonon modes observed above 350 cm^{-1}, were the stretching of the sulphur atoms, between 250 cm^{-1} and 380 cm^{-1} were the bending of the gallium sulphide tetrahedron, at 275 cm^{-1} were the vibrations of the gallium atoms and between 200 cm^{-1} and 240 cm^{-1} were the vibrations of the calcium atoms.

Absorption Spectra and Bandgap

The optical energy gap, E_g, of the single crystals can be determined from the square of the product of the optical absorption coefficient, $\alpha(\omega)$, and the incident photon energy $h\nu$ versus the photon energy $h\nu$ by Eqn. 28. The optical absorption of the $CaGa_2S_4 + Ga_2S_3$ single crystal, in the fundamental absorption edge increased sharply, which indicates that the single crystals have a direct energy band gap structure.

The variation of $(\alpha h\nu)^2$ as a function of the incident photon energy $h\nu$ is shown in Fig. 5.11 (a) for the $CaGa_2S_4 + Ga_2S_3$ single crystals. A weak absorption tail is seen below the exponential part of the absorption edge. Its strength and shape were reported to be dependent on the preparation and purity of the material[103–105]. By extrapolation to zero, the bandgap of the undoped single crystals were found to be 32,900 cm^{-1} (4.08 eV).

Fig. 5.11 (b) shows the variation of $(\alpha h\nu)^2$ as a function of the incident photon energy $h\nu$. A strong absorption is seen between 22,000 cm^{-1} and 25,500 cm^{-1}, which is the absorption of cerium into its ^2D excited state, which is not seen in the undoped single crystals. Above 27,000cm^{-1} the absorption of the doped phosphor again increases. This is the absorption near the bandedge of the impurity, Ga_2S_3, which is lower than the bandedge of the host crystal. By extrapolation, the optical energy bandgap of the Cerium activated $CaGa_2S_4 + Ga_2S_3$ phosphor is found to be 28,000 cm^{-1} (3.47 eV) with an accuracy of ± 0.02 eV. The reason for plotting $(\alpha h\nu)^2$ as the ordinate rather than α^2 was explained in Chapter III.

Fig. 5.12 shows the refractive index and the extinction coefficient for the cerium activated phosphors (upper panel), and for the unactivated single crystals (lower panel). In the midinfrared region and the visible region the refractive index were found to be nearly constant at 2.0, with the refractive index of the undoped single crystals being slightly lower than that of the doped phosphors, which is associated with the higher bandgap of the undoped single crystals.

Discussion

In this chapter, a set of frequency-dependent optical spectral functions from the far infrared through the ultraviolet region for the unactivated and the cerium activated calcium thiogallate phosphors were presented. X-Ray diffraction studies on the crystal shew that calcium thiogallate is an orthorhombic crystal with lattice parameters a=20.087Å, b=20.087Å and c=12.112Å. Group theory studies show that there are 224 atoms per unit cell. Hence there are 669 optical phonon modes, out of which some are Raman active and some are infrared active.

The phonon modes of lighter atoms are seen at higher frequencies and heavier atoms are seen at lower frequencies.[106] Gallium and sulphur form a tetrahedron, and sulphur being the lightest, its phonon mode is observed at a higher frequency compared to gallium. In between the phonon modes of gallium and sulphur, a triple mode is seen, which is due to the reduced mass of gallium and sulphur, in the gallium sulphide tetrahedron. Vibrations of the calcium atoms are observed at even low frequencies, compared to gallium and sulphur.

Far infrared reflectance spectra of the doped sample reveal isotropic properties. Since the lattice parameter c is different from a and b, the reflectance and transmittance measured parallel to the c axis should be different from the reflectance and transmittance measured perpendicular to the c axis or parallel to the c axis. But the measured reflectance in the far infrared region was very similar, for both the directions of polarizations as seen in Fig 5 9(a). This is because, in the doped samples, the grains were oriented in random directions, which shows that the doped samples are polycrystalline in nature The undoped single crystals show a very strong anisotropy in the far infrared region, as can be seen in Fig 5.3(a) and (b). This shows that the undoped crystals are single domain crystals.

The optical absorption spectra shown in Fig. 5 11(b) for the Ce CaGa$_2$S$_4$ shows very strong absorption between 22 000 cm^{-1} and 25,000 cm^{-1}, which is the impurity optical absorption peak due to the cerium dopant, which can be seen in both the reflectance and transmittance spectra for the doped crystals in this frequency region. This absorption peak which arises from the electron transitions between the energy levels of the Ce^{3+} ion, explains the luminescent nature of the cerium doped single crystals In the optical absorption spectra shown in Fig 5 11(a) for the unactivated CaGa$_2$S$_4$ +Ga$_2$S$_3$ single crystals, no absorption was seen in this frequency region Since emission is followed by absorption, only the doped CaGa$_2$S$_4$ can emit light. The emission band of calcium thiogallate is located at longer wavelengths than are generally observed for cerium in oxide hosts. This spectral shift is a consequence of the nephelauxetic effect [101]

Form the width of the absorption band, it is possible to estimate how large the difference in chemical bonding between the excited state and the ground state (ΔR) is. The value of ΔR measures the strength of the interaction between the electrons and vibrations of the luminescent center The absorption band of cerium in calcium thiogallate is very broad, showing that the coupling is strong.

In addition to this cerium absorption, another strong absorption was seen above 27,500 cm^{-1}, for the doped phosphor which is the absorption near the band edge of the impurity Ga$_2$S$_3$, present in the Ce:CaGA$_2$S$_3$ The bandgap of the undoped single crystals obtained from the absorption spectrum was 4.08 eV, whereas for the doped phosphors the bandgap was at 3.47 eV. The impurity present in Ce:CaGa$_2$S$_4$ is Ga$_2$S$_3$, which has a bandgap of 3.31 eV.[1] Hence the bandgap of Ce:CaGa$_2$S$_4$ is much lower than that of CaGa$_2$S$_4$.

One reason for the shift in the bandgap towards lower or higher frequencies is the stress on the crystal due to the presence of impurity atoms. In a perfect infinite crystal, there are no electron energy levels in the forbidden band. However, there are always some departure from a perfect periodic field, due to the presence of impurity atoms. Such impurity atoms, although their density is significantly lower than that of the crystal atoms, can introduce stress on the crystal, due to difference in radii of the host and the impurity. The levels making up the valence band maximum can shift up and down independently. The valence band maximum can become nondegenerate in some stress states. The conduction band minimum can also shift independently of each other.[79] There is an abundance of literature on the studies of doping on other degenerate semiconductors such as germanium[107] and InSb[108]. These authors have observed shifts in the absorption edge both toward shorter and longer wavelength as the impurity doping increases.

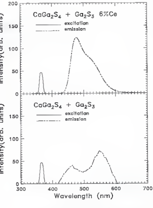

Fig 5.1 Excitation and emission spectra for (a) Cerium doped $CaGa_2S_4$ + Ga_2S_3 single crystal (b) unactivated $CaGa_2S_4$ + Ga_2S_3 single crystal.

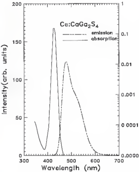

Fig 5.2 The absorption and emission spectra for the Cerium activated $CaGa_2S_4 + Ga_2S_3$ single crystal

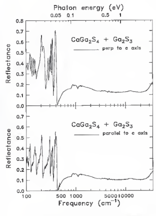

Fig. 5.3 Room temperature reflectance spectrum of a 45 μm thick $CaGa_2S_4$ + Ga_2S_3 single crystal (a) measured along the c axis (b) measured on the same sample on the ab plane.

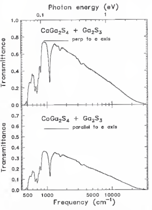

Fig. 5.4. Room temperature transmittance spectrum of a 45 μm thick $CaGa_2S_4 + Ga_2S_3$ single crystal (a) measured along the c axis (b) measured on the same sample on the ab plane

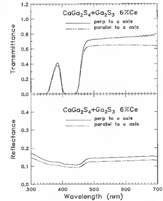

Fig 5.5 (a) Room temperature transmittance spectrum of a 50 μm thick $CaGa_2S_4$ + Ga_2S_3 single crystal activated with Cerium (b) reflectance spectrum measured on the same sample.

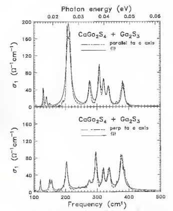

Fig. 5 6 The real part of the optical conductivity of the unactivated $CaGa_2S_4$ + Ga_2S_3 single crystal in the far infrared region The dashed line represents the conductivity obtained by Kramers Kronig analysis and the solid line represents the Drude Lorentz fit on the conductivity

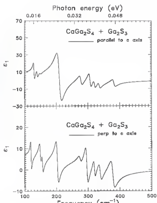

Fig 5.7 The real part of the dielectric constant of the unactivated $CaGa_2S_4$ + Ga_2S_3 single crystal in the far infrared region

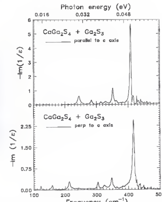

Fig 5.8 The loss function of the unactivated $CaGa_2S_4 + Ga_2S_3$ single crystal in the far infrared region

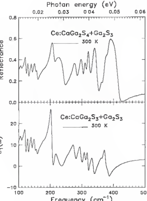

Fig 5.9 (a) The reflectance of the cerium activated $CaGa_2S_4 + Ga_2S_3$ single crystal in the far infrared region (b) The real part of dielectric constant obtained from Kramers Kronig analysis on the same sample

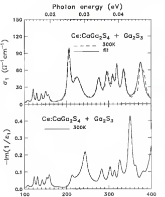

Fig 5 10 (a)The real part of the optical conductivity of the cerium activated $CaGa_2S_4 + Ga_2S_3$ single crystal in the far infrared region. (b) Loss function of the same sample

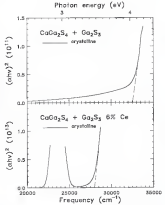

Fig 5.11: Absorption spectra of $CaGa_2S_4 + Ga_2S_3$ single crystal.(a) unactivated (b) activated with Cerium.

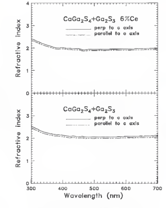

Fig 5.12 Refractive index for the (a) Cerium activated $CaGa_2S_4$ + Ga_2S_3 single crystal (b) unactivated $CaGa_2S_4$ + Ga_2S_3 single crystal

CHAPTER VI

OPTICAL STUDIES OF THIN FILMS OF CERIUM DOPED CALCIUM THIOGALLATE

This chapter discusses the optical properties of the amorphous and polycrystalline thin films of cerium doped $CaGa_2S_4$. The characteristics of the thin films are not identical with those of the bulk material from which it is prepared. The optical properties of the thin films depend on the conditions of formation of the film, for example the substrate temperature.[100] From the optical studies on single crystals, amorphous thin films and polycrystalline thin films, the effects of crystallinity, bandgap and the vibrational features of the thin films versus the bulk crystalline material can be studied.[110-113] The optical constants were determined from the reflectance and transmittance measured over a wide frequency range, from the far infrared to the ultraviolet.

Transmittance and reflectance of a thin film is usually complicated due to the fact that the film is deposited on a substrate. The quantities which are desired are the transmittance and reflectance of light through/by the film. But the measured transmittance and reflectance are the transmittance and reflectance of light through/by the film and the substrate. Hence, in this study, the transmittance and reflectance of the substrate were measured over the same frequency region as that of the film on the substrate and the optical properties were determined before the analysis of the properties of the thin films.

Annealing of the as-deposited $CaGa_2S_4$ thin films resulted in polycrystalline films, in which the experimentally measured spectra show a complicated mixture of in-plane and out-of-plane response. The infrared phonons of these samples showed many interesting features which were explained based on the behaviors of the c-axis phonons in oriented single crystals. The spectra of polycrystalline films are very much dependent on factors such as material preparation techniques,[114] surface treatments[115] and degree of orientation. The optical response of the thin films were characterized by an effective average contribution from the single crystal ab-plane and c axis directions. This was done by a comparison of the experimental data with theoretical calculation predicted by a model of effective medium approximation.

Thin films of $CaGa_2S_4$ doped with cerium ion were prepared by rf magnetron sputtering from the respective thiogallate targets. The films were amorphous as deposited. Crystallization and activation were achieved by post deposition annealing at 500°C for two hours in nitrogen atmosphere.

Results

Optical Properties of Amorphous Thin Films of Ce,$CaGa_2S_4$.

Fig. 6.1 shows the transmittance and reflectance spectra of the 2.45 μm thick cerium doped $CaGa_2S_4$ film as deposited on a 0.1cm thick glass substrate. The dashed line is the experimental data and the solid line shows the calculated value obtained from a single set of oscillator parameters which fit independently both the reflectance and the transmittance. Above 2,000 cm^{-1}, fringes were seen in the reflectance and transmittance spectra. These were due to multiple internal reflectance from the front and back surface of the film. The measured optical properties of the glass substrate were used in the calculation. The details of the optical properties of the substrate will be discussed in Chapter VII.

In Fig. 6.1(a), no transmittance is observed below 2,000cm^{-1}. This is because the substrate, which is glass, is opaque below 2,000 cm^{-1}. Above 29,000 cm^{-1} the transmittance started decreasing drastically, since the band edge of the thin film is approached. The far infrared reflectance is dominated by phonon modes, as seen in fig 6.1(b). The optical features at 689 cm^{-1} and 1,040 cm^{-1} are the phonon modes of glass.

Fig. 6.2 (a) and (b) shows the far infrared reflectance and the optical conductivity of the amorphous thin films. The optical conductivity is obtained from the set of oscillator parameters used in fitting the reflectance and transmittance spectra. Table. 6.1 shows the oscillator parameters and the TO and LO phonon frequencies for the amorphous cerium doped $CaGa_2S_4$ films. ω_{pj}, ω_j, and γ_j are the oscillator strength, center frequency and line width of the jth oscillator, which were discussed in section V. ω_{TO} and ω_{LO} are the TO and LO phonon frequencies.

The reflectance of amorphous cerium doped $CaGa_2S_4$ film is dominated by a total of five phonon modes. These phonon modes are at 130 cm^{-1}, 140 cm^{-1}, 206 cm^{-1}, 339 cm^{-1} and 350 cm^{-1}. The phonon modes at 350 cm^{-1} and 206 cm^{-1} are the stretching of the sulphur atom, and the vibrations of the calcium atom respectively. The phonon modes at 339 cm^{-1} is the bending mode of the Ga_2S_3 tetrahedron.

Optical Properties of Polycrystalline Thin Films of $Ce{:}CaGa_2S_4$.

Fig. 6.3 (a) and (b) shows the transmittance and reflectance of the polycrystalline thin films of $Ce{:}CaGa_2S_4$ deposited on glass substrate. The reflectance and transmittance are plotted on a logarithmic frequency scale. Around 25,000 cm^{-1}, fringes disappear and an absorption feature is seen in both the reflectance and transmittance spectra. This is the absorption of the cerium ion into its ^2D excited state. The far infrared reflectance is very high, compared to that of the amorphous thin films and a total of fifteen phonon modes are seen in the far infrared reflectance spectrum.

Fig. 6.4 shows the far infrared reflectance and the real part of conductivity, of the polycrystalline thin films of $Ce{:}CaGa_2S_4$. The conductivity in the far infrared region

Table 6.1 Parameters of Lorentz fit to the reflectance of amorphous thin films of Ce:CaGa$_2$S$_4$

Oscillators	ω_{pj} (cm^{-1})	$\omega_j(\omega_{TO})$ (cm^{-1})	γ_j (cm^{-1})	ω_{LO} (cm^{-1})
Phonon transitions	61	130	60	322
	290	140	300	433
	190	206	75	474
	300	339	75	543
	340	350	80	606
Interband transitions	2,800	30,000	800	
	5,060	31,600	3,800	
	3,000	33,000	2,000	
	1,000	39,000	40,000	

Thickness = 2.45 μm

$\epsilon_\infty = 4.0$

was obtained from the set of oscillator parameters used in fitting the reflectance. Table. 6.2 shows the oscillator parameters and the TO and LO phonon frequencies for the polycrystalline Ce:CaGa$_2$S$_4$ thin films in the far infrared region. The phonon modes observed above 340 cm^{-1} are the stretching of the sulphur atoms. The phonon modes observed at 210 cm^{-1} and 227 cm^{-1} are the vibrations of the calcium atoms. The phonon modes observed between 240 cm^{-1} and 340 cm^{-1} are the bending modes of the Ga$_2$S$_3$ tetrahedron.

Table 6.2. Parameters of Lorentz fit to the reflectance of polycrystalline Ce:CaGa$_2$S$_4$ thin films

Oscillators	ω_{pj} (cm^{-1})	$\omega_j(\omega_{TO})$ (cm^{-1})	γ_j (cm^{-1})	ω_{LO} (cm^{-1})
Drude	30	0	30	
Phonon	32	98	12	99
transitions	77	120	18	123
	45	140	12	141
	43	150	9	151
	80	204	7	235
	220	210	20	–
	80	227	10	–
	114	273	12	277
	113	290	12	302
	72	309	7	310
	140	321	8	325
	182	333	10	348
	180	360	40	–
	152	380	20	403
Interband	1000	12000	10000	
transitions	1500	23500	5000	
	2800	33000	1000	
	5000	34000	700	
	1000	42000	40000	

Thickness=2.65 μm

$\varepsilon_\infty = 4.0$

Optical Properties in the Visible Region

The minimum energy between the valence and conduction bands in the crystal is the band gap. The absorption edge associated with the electronic transitions between the valence and conduction bands in the crystal begin at the absorption edge. In Fig. 6.5 (a) and (b), $(\alpha h\nu)^2$ are plotted as a function of the phonon energy for the amorphous and the polycrystalline thin films. Since the increase in $(\alpha h\nu)^2$ as a function of the photon energy $h\nu$ is very sharp at the absorption edge, these materials were direct band gap materials.

The band gap for the amorphous and polycrystalline thin films are abtained from the spectra shown in Fig. 6.6(a) and (b), respectively, by a linear extrapolation of $(\alpha h\nu)^2$ to zero. The bandgap is 29,100 cm^{-1} (3.61 eV) and 32,900 cm^{-1} (4.08 eV), for the amorphous and polycrystalline thin films respectively.

Fig. 6.6 (a) and (b) shows the refractive index and extinction coefficient of the amorphous and polycrystalline thin films of Ce:CaGa$_2$S$_4$ in the visible region. The refractive index increased slightly with frequency. For the polycrystalline thin films, the refractive index is 2.008 at 10,000 cm^{-1} and 2.013 at 25,000 cm^{-1}, whereas for the amorphous thin films these values are 2.155 at 10,000 cm^{-1} and 2.172 at 25,000 cm^{-1}. The refractive index for the polycrystalline thin films was very similar to the refractive index of the Ce:CaGa$_2$S$_4$ bulk crystal discussed in Chapter V. The lower refractive index of the polycrystalline thin films compared to the amorphous thin films is associated with a shift of the fundamental absorption spectra towards higher frequencies. The extinction coefficient for the thin films is very low in the visible region due to the transparent nature of the thin film. For the polycrystalline thin films the extinction coefficient was 0.00081 at 16,000 cm^{-1} and 0.0039 at 25,000 cm^{-1}, whereas for the amorphous thin films these values were 0.00035 at 10,000 cm^{-1} and, 0.0047 at 25,000 cm^{-1}.

Fig. 6.7(a) and (b) shows the real part of dielectric constant of thin films of amorphous and polycrystalline Ce:CaGa$_2$S$_4$. The static dielectric constant of the amorphous thin films is 11.75 and that of the polycrystalline thin films is 7.46. The static dielectric constant is obtained from the set of oscillator parameters, used in fitting the measured data, after removing the Drude parameters. The optical dielectric constant of the thin films, which is the dielectric constant at high frequencies is obtained by fitting the reflectance and transmittance, and is found to be 4.0.

Photoluminescence

The photoluminescence spectra of the polycrystalline thin films of Ce:CaGa$_2$S$_4$ and for comparison the photoluminescence of the Ce:CaGa$_2$S$_4$ bulk crystals are shown in Fig. 6.8. These samples were excited at 365 nm using a xenon lamp and a UV filter. No photoluminescence was observed in the amorphous thin films.

The emission spectra of the polycrystalline thin films are blue shifted when compared to that of the bulk crystals. This is because the 5d excited state of the cerium ion has a strong interaction with the crystal field of the host. Hence a change in the surroundings of the cerium ion will have a distinct influence in the emission spectrum. The presence of oxygen in the thin films will also result in blue shift in thiogallates, since oxygen replaces the sulphur ligands.[118]

Effective Medium Approximation

The far infrared spectra of the single crystals of CaGa$_2$S$_4$ has a very strong anisotropy for light polarized parallel and perpendicular to the c axis. For these crystals $\epsilon_a \approx \epsilon_b \neq \epsilon_c$. The infrared spectra of a CaGa$_2$S$_4$ polycrystalline thin film can be regarded as a randomly inhomogeneous media consisting of a mixture of grains polarized parallel and perpendicular to the c axis. An effective medium is the equivalent uniform material that exhibits the same dielectric properties over a limited wavelength range as the microscopically inhomogeneous material it represents.

The propagation of an electromagnetic wave in an inhomogeneous medium involves the scattering of the wave by the inhomogenities. If the wavelength is large compared with the size of the inhomogenities, the wave is unable to resolve the individual scattering centers and the medium appears to be homogeneous and the medium can be treated as if it were uniform with an effective dielectric function $\epsilon_{eff}(\omega)$ to describe its average response to the applied fields. In this case only forward scattering occurs.

For large inhomogenities, the scattered intensity has an angular dependence. In an anisotropic material, which can be taken as a uniaxial crystal, let the wave vector of the propagating light q make an angle θ with the c axis. The dielectric function is then given by[117,118]

$$\epsilon_{eff}(\theta) = \frac{\epsilon_{\parallel}\epsilon_{\perp}}{\epsilon_{\perp}\cos^2\theta + \epsilon_{\parallel}\sin^2\theta} \tag{50}$$

$$\frac{1}{\epsilon_{eff}(\theta)} = \frac{\cos^2\theta}{\epsilon_{\parallel}} + \frac{\sin^2\theta}{\epsilon_{\perp}} \tag{51}$$

where $\epsilon_{\parallel}$ and $\epsilon_{\perp}$ are the ab-plane and the c-axis dielectric function, respectively. At $\mathbf{q} \parallel \mathbf{c}$, $\theta = 0$, the propagation is along the c-axis and the $\mathbf{E}$ field is polarized in the ab-plane, so that $\epsilon_{eff} = \epsilon_{\parallel}$. When $\theta = \pi/2$ ($q \perp \mathbf{c}$), the propagation is perpendicular to the c-axis and the $\mathbf{E}$ field is polarized in the c-axis or perpendicular to the ab-plane, so that $\epsilon_{eff} = \epsilon_{\perp}$.

A polycrystalline thin film can be considered as a collection of large number of crystallites. The c axis of the i^{th} crystallite makes an angle θ_i with the wave vector $\mathbf{q}$. Let us assume that the response of the system can be characterized by an ensemble average angle θ, from which the dielectric function can be calculated from Eqn. 38 and 39 The reflectance is then determined by

$$R_{eff}(\theta) = \left| \frac{1 - \sqrt{\epsilon_{eff}}}{1 + \sqrt{\epsilon_{eff}}} \right|^2 . \tag{52}$$

The $\epsilon_{\parallel}$ and $\epsilon_{\perp}$ derived from the Kramers-Kronig transformations of the ab plane reflectance and the c axis reflectance of the single crystals were used to calculate the effective dielectric function.

Fig 6 9 shows the calculated reflectance at $\theta = 10°$, 0° and 30° according to Eqn. 52 at room temperature, and the measured reflectance of the polycrystalline thin films It turned out that the calculated results at $\theta = 10°$ give a reasonable good fit throughout the far infrared region to the measured reflectance.

The approach discussed above is appropriate if $\lambda < d$, where d is the grain size. If the wavelength of the incident light is less than the grain size ($\lambda \ll d$) in the polycrystalline thin film, then the effective total reflectance can also be approximated by averaging over the individual reflectivities of the randomly orientated grains:

$$R_{eff}(\omega) = \frac{1}{3}\mathcal{R}_{\perp} + \frac{2}{3}\mathcal{R}_{\parallel} \tag{53}$$

Fig 6.10(a) and (b) shows the measured reflectance for the polycrystalline thin films deposited on glass substrate and the reflectance measured for the bulk phosphor The solid line shows the effective reflectance calculated from the reflectance of the single crystals of calcium thiogallate, for light polarised parallel and perpendicular to the c axis, respectively

If the size of an individual grain is large compared with atomic dimensions, but small compared to the wavelength of far infrared radiation (50-1000 μm), then on the scale of the wavelength, the inhomogeneous media appear to be homogeneous and have a well defined effective dielectric response function.[28] The derivation of an effective medium model proceeds as follows:

1. The properties of the individual grains of the inhomogeneous medium are expressed in terms of their dielectric functions

2. The electrostatics problem of a uniform field applied to the mixture in terms of the microscopic electric and displacement fields is solved

3. The volume is averaged to calculate the observed properties

Suppose a laminar sample consists of separate regions of dielectric functions, ϵ_a and ϵ_b, with the field E applied parallel to the laminations. By the boundary conditions on tangential E, the microscopic field everywhere in the sample is equal to the applied field $e(r) = E$. But the local displacement is either $\epsilon_a E$ or $\epsilon_b E$ depending on whether the point r is located within material a or material b. Since the macroscopic displacement field D is the average,

$$\epsilon_{eff} = f\epsilon_a + (1-f)\epsilon_b, \tag{54}$$

where f is the volume fraction of the a phase. The same calculation is repeated for the field perpendicular to the laminations in which case the microscopic electric field, $e(r) = D/\epsilon_a$ or D/ϵ_b depending on whether r is in a or b. The average is

$$1/\epsilon_{eff} = f/\epsilon_a + (1-f)/\epsilon_b \tag{55}$$

The purpose of the effective medium model is to account for the effects of the screening charges that accumulate on boundaries between regions in a microscopically inhomogeneous medium. A typical inhomogeneous system is represented by the standard effective medium expression

$$(\epsilon_{eff} - \epsilon_h)/(\epsilon_{eff} + 2\epsilon_h) = f(\epsilon_a - \epsilon_h)/(\epsilon_a + 2\epsilon_h) + (1-f)(\epsilon_b - \epsilon_h)/(\epsilon_b + 2\epsilon_h), \tag{56}$$

where ϵ_h is a host dielectric function that takes the values ϵ_a or ϵ_b if the composite consists of isolated inclusions of b in a or of a in b, respectively, or ϵ_{eff} if the phases are randomly mixed. The corresponding expressions are the "effective medium approximation" (EMA)[119,120] introduced by Bruggeman, and "Maxwell Garnett theory" (MGT)[121] due to Garnett. Both these models provide an expression for the dielectric function of a homogeneous medium with properties identical to those of the inhomogeneous medium.

For two constituent media having dielectric functions $\epsilon_\parallel$ and $\epsilon_\perp$ and assuming the volume fraction of $\epsilon_\parallel$ be f, the dielectric function in the EMA and MGT models are given by

$$\epsilon_{MGT} = \epsilon_\perp + \epsilon_\perp \frac{3f(\epsilon_\parallel - \epsilon_\perp)}{(1-f)(\epsilon_\parallel - \epsilon_\perp) + 3\epsilon_\perp} \tag{57}$$

$$\epsilon_{EMA} = B/4 \pm 1/4\sqrt{B^2 + 8\epsilon_\parallel \epsilon_\perp} \tag{58}$$

where

$$B = (3f-1)\epsilon_\parallel + (2-3f)\epsilon_\perp \tag{59}$$

The sign is chosen so that $\mathrm{Im}\,\epsilon_{EMA}$ is greater than or equal to zero. The difference between MGT and EMA is the way in which the medium surrounding the grain under consideration is treated. In the MGT, it is assumed that the medium surrounding the grains is one of the constituents of the mixture. The MGT treats the two constituents in the mixture differently. In the EMA, the medium surrounding the grain is assumed to be characterized by the effective properties of the inhomogeneous medium.

Fig. 6.11 and Fig. 6.12 shows the measured and calculated reflectance using the EMA or MGT models respectively. Here f_{ab} is the fraction of ab-planes probed by the incident electric field E. The best fit for the EMA and MGT model is obtained when the fraction $f_{ab} = 0.1$.

Discussion

The sharp vibrational features observed for the polycrystalline samples in Fig. 6.5 are due to the existence of long range order of the atoms. If the long range crystalline order was destroyed, the sharp structural detail which is typical for crystals would disappear. This can be seen for the amorphous thin films in Fig. 6.2. The broad features were due to only short range order being present in amorphous thin films. The general features of the optical conductivity of both the amorphous (Fig. 6.2(b)) and polycrystalline (Fig. 6.5(b)) thin films curves were similar and the agreement can be made better by broadening the vibrational spectra of the polycrystalline thin film by properly chosen parameters. Thus the density of states of vibrations in these films are not significantly changed by long range order.

In addition to the increased breadth of the vibrational features, the short range order in amorphous thin films also results in fewer phonon modes as compared to the polycrystalline thin films. There are only five phonon modes in the amorphous thin films as compared to the fifteen phonon modes identifiable in the polycrystalline thin films. In amorphous materials all the absorption bands should be seen at approximately the maxima of the crystalline phonon density of states curves.[121] But this did not happen for the vibrational spectra of the amorphous thin films of cerium doped calcium thiogallate thin films due to the broadening of the vibrational spectra. From Table. 6.1, it can be seen that the linewidth γ_j of the phonon modes for the amorphous thin film is very large as compared to the polycrystalline thin films in Table 6.2. The broadening is so large that some of the bands disappear, which explains the reduced number of phonon modes detectable in the amorphous thin films.

From Fig. 6.2 we see that the strongest phonon modes are observed at 190 cm^{-1} and 350 cm^{-1}. These vibrations can be interpreted as consisting of rigid sublattice motions, with each sulphur atom vibrating opposite to its two neighboring calcium and gallium atoms, and each calcium or gallium atom vibrating opposite to the sulphur atoms. Such vibrations can be expected to retain their character in the amorphous thin film because they are dominated by short range order, whereas other infrared active crystalline vibrations which are more dependent on unit cell structure and symmetry are not observed in Table. 6.2

No photoluminescence was observed in the Ce:CaGa$_2$S$_4$ amorphous thin films. Cerium as an activator in the amorphous thin films appears to be unimportant from the point of view of absorption in the thin films. This is because in the amorphous state the structure adjusts itself so that all the valence bands are satisfied.[78] The distinct absorption peak associated with cerium doping seen in Fig. 6.6(b) for the polycrystalline thin film is absent for the amorphous thin film. Instead, in the amorphous thin films, the luminescent center only contributes to fluctuations of the internal potential. In the optical spectra, doping increases the absorption near the absorption edge, for the polycrystalline thin films. This can be seen from the transmittance and reflectance spectra shown in Fig. 6.3. Fringes disappear due to strong impurity absorption, between 20,000 cm^{-1} and 25000 cm^{-1}.

The absorption edge of an amorphous material shifts either towards lower or higher energies, when it is crystallized. From Fig. 6.5(a) and (b), the absorption edge shifts towards lower energies, for amorphous versus crystalline Ce:CaGa$_2$S$_4$. The bandgap for the polycrystalline thin films were 4.08 eV, whereas the bandgap of amorphous thin films were 3.61 eV, which is associated with a higher value for the refractive index as compared to the polycrystalline thin films. The bandgap of the bulk crystalline material is 4.03 eV, which was discussed in Chapter V. The bandgaps for the polycrystalline thin films were significantly higher than that of the amorphous thin films, but very close to that of the bulk single crystals. This shift in the absorption edge of the amorphous thin films might be due to the voids present or due to impurities present in the ambient gas forming dangling bonds on the void surfaces.[123]

The far infrared properties of inhomogeneous materials are in agreement with the ideas of the effective medium approximation. The effective complex dielectric function that characterizes these materials depends on the concentrations of the constituents, the properties of the individual constituents, their sizes and the method of preparation of the sample. Both scattering and absorption remove energy from a beam of light traversing the medium. If light traverses a perfectly homogeneous medium, it is not scattered. Only inhomogeneities cause scattering. As can be seen from figures 6.11 and 6.12, the calculated reflectance using both EMA and MGT approaches is essentially higher than the experimental data, because scattering is not included in these models.

In polycrystalline thin films, grain boundary scattering is the dominant scattering mechanism.[124] The contribution due to ionized impurity scattering and optical lattice scattering were calculated and it was found that the contribution due to these two scattering mechanisms are small. The measured reflectance in the far infrared region for the polycrystalline thin films were lower than the calculated reflectance due to absorption in the thin films arising from surface roughness and grain boundary scattering.

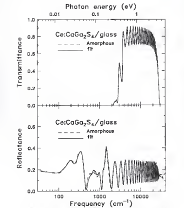

Fig. 6.1 Room temperature transmittance and reflectance of a 2.45 μm thick amorphous Ce:CaGa$_2$S$_4$ film deposited on a glass substrate. The dashed line represent the measured data and the solid line represents the calculated data.

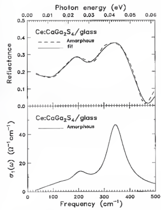

Fig. 6.2 Far infrared reflectance and conductivity of amorphous Ce:CaGa$_2$S$_4$ thin film on glass substrate

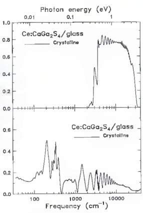

Fig 6.3 Reflectance and transmittance in the entire measured range of a 2.45 μm thick polycrystalline Ce:$CaGa_2S_4$ film. Note the logarithmic frequency scale.

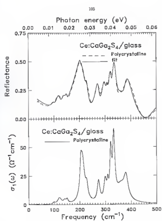

Fig. 6.4. Far infrared reflectance and real part of optical conductivity of polycrystalline Ce:CaGa$_2$S$_4$ film.

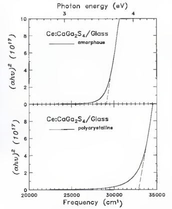

Fig 6.5 $(\alpha h\nu)^2$ as a function of frequency of (a) amorphous Ce.CaGa$_2$S$_4$ thin film. (b) polycrystalline Ce:CaGa$_2$S$_4$ thin film.

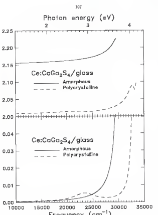

Fig 6.6 Refractive index and extinction coefficient of thin films of amorphous and polycrystalline Ce:CaGa$_2$S$_4$

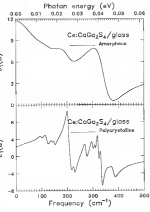

Fig 6.7 Real part of dielectric constant of thin films of amorphous and polycrystalline Ce:CaGa$_2$S$_4$.

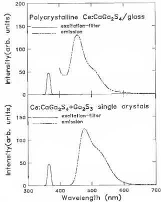

Fig. 6.8 Photoexcitation and emission spectra of (a) polycrystalline thin films of $Ce:CaGa_2S_4$ on glass substrate (b) single crystals of $Ce:CaGa_2S_4$

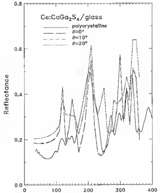

Fig 6.9 The solid lines show the reflectance in the far infrared region of polycrystalline thin films of Ce:CaGa$_2$S$_4$. The dashed line represents the calculated reflectance using Eqn 52.

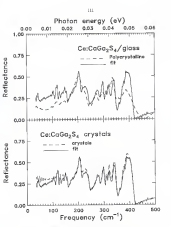

Fig. 6.10 The solid lines show the reflectance in the far infrared region of the polycrystalline thin films of Ce:CaGa$_2$S$_4$. The dashed line represents the calculated reflectance using Eqn. 6.3

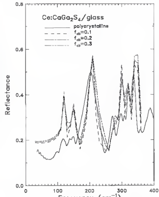

Fig 6.11 The solid lines show the reflectance in the far infrared region of polycrystalline thin films of Ce:CaGa$_2$S$_4$. The dashed line represents the calculated reflectance using the EMA theory

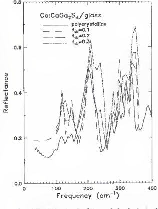

Fig 6.12 The solid lines show the reflectance in the far infrared region of polycrystalline thin films of Ce-CaGa$_2$S$_4$. The dashed line represents the calculated reflectance using the MGT theory

CHAPTER VII
OPTICAL PROPERTIES OF CERIUM DOPED CALCIUM THIOGALLATE DEVICE

This chapter describes the optical properties of layered device structure based on Ce:CaGa$_2$S$_4$ phosphor. Thin film electroluminescent (TFEL) devices used for flat panel displays are based on a MISIM (metal-insulator-semiconductor-insulator-metal) heterostructure, which was discussed in Chapter II, and shown in Fig. 2.1. The high electric field accelerates the electrons through the phosphor layer, exciting the luminescent centers on their path, causing them to generate light. Insulators provided on either side of the phosphor layer limit the current transported across the devices. The top and bottom electrodes make electrical contact to the drive electronics thereby completing the device structure. The bottom electrode is normally transparent to permit viewing of the emitted light.

Corning 7059 glass was used as the substrate for the present samples. Indium tin oxide (ITO) and aluminum oxide/titanium oxide (ATO) were the electrode and the insulator, respectively. A 0.03 μm thick zinc sulphide (ZnS) nucleation layer was used to initiate the growth of crystalline calcium thiogallate films.

To model the measured reflectance and transmittance of the device, the optical constants of the substrate and all the intermediate layers were determined. The optical constants of thin films of ITO, ATO, and ZnS were determined independently, by measuring the reflectance and transmittance of these films deposited on a glass substrate. The reflectance and transmittance were fitted using a set of oscillator parameters as discussed in Chapter III, from which all the optical constants were determined. The photoluminescence spectra of the device structure was also measured and compared with that of the Ce:CaGa$_2$S$_4$ single crystals and thin films of Ce:CaGa$_2$S$_4$ deposited on glass substrate.

Results

Reflectance and Transmittance Spectra

Fig. 7.1 shows the reflectance and transmittance of the Ce:CaGa$_2$S$_4$ based device structure, measured from 30 cm^{-1} to 48,000 cm^{-1}. In the layered device structure studied, Ce:CaGa$_2$S$_4$ is deposited on an ITO coated glass, with ATO and ZnS layers in between. No transmittance was observed below 4,000 cm^{-1}, as can be seen from Fig. 7.1(a). This is because of the ITO layer which is opaque in the far infrared region. Above 30,000 cm^{-1}, the transmittance decreased since the bandgap of the device was approached. Between 7,000 cm^{-1} and 30,000 cm^{-1}, the transmittance is very high. Interference fringes are observed in this region due to multiple internal reflectance.

The reflectance in the far infrared region is very high as can be seen from Fig. 7.1(b) due to the presence of free carriers in the ITO layer. In addition to this, phonon modes from the different layers are also seen in the reflectance spectrum. Above 7,000 cm^{-1}, the reflectance is very low and a complex fringe pattern is observed due to multiple internal reflectance, from the interfaces of the various layers.

Fig. 7.2 shows $(\alpha h\nu)^2$ as a function of the photon energy. From the absorption spectrum, it is seen that above 32,000 cm^{-1} the film becomes absorbing since the fundamental absorption edge of the device is reached. The band gap is obtained by a linear extrapolation of $(\alpha h\nu)^2$ to zero. The TFEL device studied had a band gap of 32,900 cm^{-1} (4.08eV), and is shown in Table. 7.5. The bandgap of the TFEL device is expected to be the bandgap of the layer having the lowest bandgap. In order to model the measured reflectance and transmittance of the device structure, it is necessary to know the optical constants of all the intermediate layers and the substrate. Hence the reflectance and transmittance of ITO/glass, ATO/glass and ZnS/glass were measured in the same frequency region as that of the device structure.

Optical Properties of Corning 7059 Glass

Fig. 7.3(a) and (b) shows the reflectance and transmittance of substrate, glass. The transmittance is zero in the far infrared region and is very high in the visible region. In the region where glass is opaque, the optical constants were determined from Kramers-Kronig analysis of the single bounce reflectance spectrum, as discussed in Chapter III. In the region where glass is transparent the reflectance and transmittance were determined by the inversion of equations for reflectance and transmittance.

In the far infrared region, the optical constants can also be determined from the oscillator parameters used in fitting the reflectance spectrum. Table 7.1 shows the oscillator parameters and the TO and LO phonon frequencies for glass in the far infrared region, with an accuracy of ± $0.1\mathrm{cm}^{-1}$.

Fig. 7.4(a) and (b) shows the refractive index and extinction coefficient of glass. The refractive index is almost constant at 1.54 in the visible region, varying slightly as the frequency increases. Glass has absorption bands in the far infrared region, and absorption is strongest at the resonance frequency. The index of refraction is larger at lower frequencies and increases with frequency as the resonance frequency is approached. This is normal dispersion. At or near the resonance frequency, where absorption is maximum, the refractive index decreases as the frequency increases, which is anomalous dispersion.

Fig. 7.5 shows $(\alpha h\nu)^2$ as a function of the photon energy. Corning 7059 studied has a band gap of 35 500 cm^{-1} (4.40 eV), and is tabulated in Table. 7.6. The bandgap

Table. 7.1 Parameters of Lorentz fit to the reflectance of Corning 7059 glass in the far infrared region

Oscillators	ω_{pj} (cm^{-1})	$\omega_j(\omega_{TO})$ (cm^{-1})	γ_j (cm^{-1})	ω_{LO} (cm^{-1})
Phonon	127	90	107	102
transitions	415	445	106	500
	262	689	164	716
	150	780	100	787
	819	1,060	168	1,178
	387	1,374	150	1,427
	387	2,433	578	2,722

Thickness =0.118 cm

was determined by extrapolating $(\alpha h\nu)^2$ to zero. The sharp increase of $(\alpha h\nu)^2$ as a function of photon energy shows that the glass studied is a direct bandgap material.

Optical Properties of Indium Tin Oxide

Thin films of indium tin oxide (ITO) have been extensively used in a variety of electronics and optoelectronics applications due to high transmittance in the visible region, high infrared reflectance and low electrical resistivity.[126-127] This simultaneous occurrence of high optical transparency and high electrical conductivity does not occur in metals or in intrinsic stoichiometric materials. The typical way to obtain good transparent conductors is to create electron degeneracy in a wide bandgap oxide by controllably introducing non stoichiometry and/or appropriate dopants. These conditions are conveniently obtained in oxides of cadmium, tin, indium, zinc and other alloys in thin film form prepared by a number of deposition techniques. ITO films used in this study were prepared by a commercial r.f. magnetron sputtering system.

Undoped tin oxide (TO) films are polycrystalline with a grain size of about 200-300Å and retain the tetragonal rutile structure of bulk SnO_2.[124,125] Pure SnO_2 films exhibit a direct optical bandgap of 3.87–4.3eV.[129,130] The visible and near IR transmittance is about 80 %.[131] The refractive index is fairly constant in the visible region and ranges typically between 1.8 and 2.0.[132] These films are extremely stable under typical environmental conditions and are extremely resistant to chemical etching. The films are etched only by nascent hydrogen produced by reaction of zinc powder with HCl. Their adhesion to glass or porcelain is very high. Hence the film is possibly attached to the substrate by chemical bonds.[133]

Undoped indium oxide (IO) films are polycrystalline with a grain size of about 100Å for reactively sputtered films, and a cubic bixbyte structure, for the bulk material.[134] The superiority of IO over TO films as transparent conductors is due to the higher mobility in IO. IO films exhibit a direct optical bandgap which lies between 3.55 and 3.75eV.[135,136] The bandgap increases with increasing carrier concentration. The optical transmittance in the visible and near infrared regions is about 75%–90%.[74,137,138] The refractive index in the visible region is between 1.9 and 2.08.[134,138]

ITO films retain the bulk structure of IO, but exhibit a slight increase in the lattice constant and a strong (100) or (111) orientation depending on the deposition parameters.[139-142] The electrical and optical properties are independent of the orientation effects.[140,141] The grain size of ITO ranges between 400 and 600Å. The resistivity of these films decreases initially with increasing tin concentration, but starts increasing at still higher concentration. ITO films generally etch more easily than

TO films However the chemical stability of ITO is adequate for many sophisticated applications[143]

Fig 7.6(a) and (b) shows the optical transmittance and reflectance and the fits to the experimental data, over the frequency range from 30 cm^{-1} to 48,000 cm^{-1}, for ITO on glass substrate. The reflectance and transmittance were fitted independently using the same set of oscillator parameters In the visible region a transmittance of 80% to 90% was observed and in the far infrared region the reflectance is almost 78% This high reflectance is due to the high density of free electrons The presence of free carriers in the film results in the Drude type absorption edge in the infrared region of the spectrum. In the near infrared region, the reflectance decreases drastically and the transmittance increases due to the plasma effect resulting from high concentration of mobile carriers. Table. 7.2 shows the oscillator parameters used in fitting the reflectance and transmittance, of the ITO thin film. The many oscillators in the UV region are required to fit the actual sharp absorption edge at the bandgap These follow the joint density of states of the interband transitions

The film thickness can be very accurately determined, since thickness is also an input parameter in fitting the reflectance and transmittance spectra. The thickness of the ITO films used in this study was found to be 0.14 μm. Fig. 7.7(a) and (b) shows the real part of complex conductivity and real part of complex dielectric function of ITO. The conductivity of thin films of ITO is very high in the infrared region and in the ultraviolet region From Fig. 7.7(b), the region where the dielectric constant ϵ_1 crosses the zero cutoff frequency ω_{p_1} is the region where metal like infrared (IR) reflectance changes to dielectric like visual transmittance. For frequencies less than ω_p, ϵ_1 is negative and the film becomes highly reflective.

Fig. 7.8(a) and (b) shows the refractive index and extinction coefficient of ITO, obtained from a set of oscillator parameters (shown in Table 7.2) used in fitting the

Table. 7.2 Parameters of oscillator fit to the reflectance and transmittance of of ITO

Oscillators	ω_{pj} (cm^{-1})	$\omega_j(\omega_{TO})$ (cm^{-1})	γ_j (cm^{-1})
Phonon transitions	5,232	150	330
	8,400	225	1,186
	3,000	450	200
	2,932	1,000	701
	9,485	1,100	1,215
Interband transitions	4,000	30,000	5,000
	4,282	32,000	9,460
	11,500	35,000	2,031
	7,833	36,500	422
	7,000	38,000	527
	4,389	39,000	68.3
	9,726	40,000	898
	10,727	41,000	009
	14,524	42,000	397

Thickness = 0.14 μm

$\epsilon_{\infty} = 3.6$

reflectance and transmittance. The refractive index varies between 1.05 and 2.40 in the visible region. At 12,000 cm^{-1} the refractive index is 1.65 and at 30,000 cm^{-1}, the refractive index is 2.14. Refractive index in the visible region as obtained by various authors exhibits a marked scatter between 1.8 and 2.1 [144-147].

Fig. 7.9 shows $(\alpha h\nu)^2$ as a function of the photon energy. Above 33,000 cm^{-1} the film becomes absorbing since the fundamental absorption edge of the material is reached. It was observed that $(\alpha h\nu)^2$ increased sharply with photon energy which shows that ITO is a direct band gap material. ITO films studied have a band gap of 34,000 cm^{-1} (4.22 eV). This is tabulated in Table. 7.6

Optical Properties of Aluminum oxide/Titanium oxide

Thin films of aluminum oxide/titanium oxide (ATO) was used as the insulator in the Ce $CaGa_2S_4$ device structure. Fig. 7.10(a) and (b) shows the optical transmittance and reflectance and the fits to the experimental data of ATO deposited on glass substrate over the frequency range from 30 cm^{-1} to 48,000 cm^{-1}. In the visible region, a transmittance of 80% to 90% was observed. In the far infrared region the reflectance was dominated by a total of nine phonon modes.

The reflectance and transmittance were fitted independently using nine oscillators. The thickness of the ATO films obtained from the fit is 0.23μm. Table 7.3 shows the oscillator parameters used in fitting the reflectance and transmittance, and the TO and LO phonon frequencies of the ATO thin films.

Low frequency modes are made up of vibrations due to heavier atoms and high frequency modes are made up of lighter atoms. The phonon modes observed at higher frequencies are the stretching mode and bending modes of the aluminum-oxygen bonds, since aluminum is lighter than titanium. The phonon modes observed at lower frequencies are the stretching and bending modes of the titanium-oxygen bonds. In sapphire, which is Al_2O_3, two strong phonon modes are reported[148] at 660 cm^{-1} and 450 cm^{-1}, which were assigned to the stretching and bending modes of Al_2O_3. Since titanium is heavier than aluminum, the phonon modes of the titanium-oxygen bonds should be at a lower frequency than that of the aluminum-oxygen bonds. The

Table 7.3 Parameters of oscillator fit to the reflectance and transmittance of ATO

Oscillators	ω_{pj} (cm^{-1})	$\omega_j(\omega_{TO})$ (cm^{-1})	γ_j (cm^{-1})	ω_{LO} (cm^{-1})
Drude	2,000	0	1,000	
Phonon	850	340	200	399
transitions	500	430	50	571
	600	650	200	697
	650	700	100	
	460	770	70	835
	600	900	170	
	800	990	150	
	1,100	1,020	100	1,377
	500	1,040	20	-

Thickness = 0.23 μm

$\epsilon_{\infty}=3.3$

phonon mode observed at 340 cm^{-1} is therefore the stretching of the titanium oxygen bond.

Fig. 7.11(a) and (b) shows the refractive index and extinction coefficient of ATO, obtained from a set of oscillator parameters used in fitting the reflectance and transmittance. The refractive index remained nearly constant in the visible region and had a value of 1.8 at 12,000 cm^{-1} and 1.81 at 25,000 cm^{-1}. The extinction coefficient was very low and had a value of 0.0007 at 12,000 cm^{-1}, and 0.00007 at 25000 cm^{-1}. Fig. 7.12(a) and (b) shows the real part of complex conductivity and real part of dielectric function of ATO. From Fig. 7.12(b) the static dielectric constant is found to be 12.0. The bandgap of ATO is higher than that of the substrate. As a result it was not possible to determine the bandgap of ATO.

Optical Properties of ZnS

Zinc sulphide is a wide band gap semiconductor material that finds applications in light emitting diodes, electroluminescent displays, multi-layer dielectric filters, optical phase modulation systems in integrated optics, etc.[149] Its energy bandgap is large enough for this material to be used as host matrix for a large variety of dopants. The luminescent properties of ZnS doped with manganese is adequate for electroluminescent applications. For the MISIM device in this study, ZnS is used as the nucleation layer for growth of the thiogallate thin film.

Fig. 7.13(a) and (b) shows the optical transmittance and reflectance and the fits to the experimental data, over the frequency range from 30 cm^{-1} to 48,000 cm^{-1}, for thin films of ZnS on glass substrates. The far infrared reflectance is dominated by a strong phonon mode at 273 cm^{-1}. Above 2,500 cm^{-1}, fringes are observed in the reflectance and transmittance spectra due to multiple internal reflectance from the front and back surface of the film. The thickness of the ZnS used in this study is 0.63 μm. The reflectance and transmittance were fitted independently using the same set of oscillator parameters. Table 7.4 shows the oscillator parameters used in fitting the reflectance and transmittance spectrum, and the TO and LO phonon frequencies for the thin films of ZnS.

Fig. 7.14(a) and (b) shows the dispersion of refractive index and extinction coefficient of ITO, obtained from a set of oscillator parameters used in fitting the reflectance and transmittance. The refractive index was constant in the visible region. The refractive index at 10,000 cm^{-1} is 2.23 and at 30,000 cm^{-1} is 2.3.

Table. 7.4 Parameters of the oscillator fit to the reflectance and transmittance of ZnS thin films

Oscillators	ω_{pj} (cm^{-1})	$\omega_j(\omega_{TO})$ (cm^{-1})	γ_j (cm^{-1})	ω_{LO} (cm^{-1})
Phonon transition	470	273	13	345
Interband transitions	7,000	32,000	1,500	
	5,000	32 500	1,500	
	6,073	35 000	4,389	
	20,000	39,145	8,000	

ϵ_∞=4.8

Thickness=0.63 μm

The real and imaginary parts of the complex dielectric response function and complex conductivity in the far infrared region are shown in Fig. 7.15(a) and (b) respectively. There are two characteristic optical phonon frequencies, the LO and TO phonon frequencies. The difference between the LO and TO modes indicate the ionicity of the compound. The LO phonon frequency was determined using the Drude model, which consists of finding the frequency at which the real part of the dielectric function, goes through zero frequency. The TO phonon frequency was determined from the position of the maximum in the imaginary part of the dielectric response function. The values of the TO and LO frequencies so obtained are at 273 cm^{-1} and 345 cm^{-1}, which are in excellent agreement with those reported for the single crystals of ZnS.[160] The values reported by this author was 273 cm^{-1} for the TO phonon frequency and 350 cm^{-1} for the LO phonon frequency.

The static dielectric constant (ϵ_0) and the optical dielectric constant, (ϵ_∞) are related through the Lyddane-Sachs-Teller relation,[106]

$$\epsilon_0 = \epsilon_\infty(\frac{\omega_{LO}}{\omega_{TO}})^2 \tag{56}$$

The experimental determination of ϵ_0 is unambiguous, since it is the limit for long wavelengths. But ϵ_∞ is not so well defined, because in the high frequency region, there is an overlap with the dielectric contribution from electronic oscillators. The values obtained for ϵ_0 and ϵ_∞ were 7.9 and 4.8, by fitting the experimental reflectance and transmittance from the phonon oscillator and from the electronic transitions. These values satisfy the Lyddane-Sachs-Teller relation.

Fig. 7.16(b) shows $(\alpha h\nu)^2$ as a function of the photon energy. From the absorption spectrum, it is seen that above 32,000 cm^{-1} the film becomes absorbing since the fundamental absorption edge of the material is reached. It was observed that $(\alpha h\nu)^2$ increased sharply with photon energy which shows that ZnS is a direct band gap material. ZnS has almost no absorption from the fundamental direct bandgap down to the infrared region at around 373cm^{-1}, where strong absorption occurs due to phonon absorption. The ZnS films studied have a band gap of 32,500 cm^{-1} (4.03 eV). This value is tabulated in Table 7.6. The value of the bandgap for thin films of ZnS reported in literature varies between 3.48 eV and 3.70 eV.[161,162]

Photoluminescence Spectra

Fig. 7.17 shows the photoluminescence spectra of Ce:$CaGa_2S_4$ based device structure, polycrystalline thin films of Ce:$CaGa_2S_4$ on glass substrate and single crystals of Ce:$CaGa_2S_4$, which emits blue light. It was observed that the emission spectra of the single crystals had a peak at 475 nm and a low energy shoulder at 530 nm. For the thin films on glass substrate, these values were at 456 nm and 511 nm, respectively

Table 7.5. Peak values of the emission spectra.

Materials	^2D-$^2F_{5/2}$ (nm)	^2D-$^2F_{7/2}$ (nm)
Ce:CaGa$_2$S$_4$ (crystals)	475	530
Ce:CaGa$_2$S$_4$ (thin films)	456	511
Ce:CaGa$_2$S$_4$ (device)	444	500

and that of the device were at 444 nm and 500 nm, respectively. Table 7.5 shows the peak values of the emission spectra for the bulk crystals, polycrystalline thin films and for the device strucure based on Ce:CaGa$_2$S$_4$

Optical Properties of Multilayers on Glass Substrate

The optical parameters of the multilayered structure were obtained by fixing all the parameters for the individual layers obtained by the oscillator fit method, and varying only the thickness until the best fit is obtained. Fig. 7.18 shows the transmittance, reflectance and fits of the multi-layered structure ATO/ITO/Glass. The parameters obtained from the oscillator fit method for the thin films of ATO and ITO are shown in Table. 7.2 and 7.3 respectively. The best fit for the reflectance and transmittance occurs when the thickness of the ATO and ITO layers are 0.3504 μm and 0.3500 μm respectively.

Fig. 7.19 shows the transmittance, reflectance and fits of the multilayered structure ZnS/ITO/Glass. The parameters obtained from the oscillator fit method for the thin films of ZnS is shown in Table 7.4. The best fit for the reflectance and transmittance were obtained when the thickness of the ZnS and ITO layers were 0.66 μm and 0.14 μm respectively. However the calculated reflectance and transmittance were much higher than the measured reflectance and transmittance. The sample was not transparent, and due to surface roughness, there was considerable amount of scattering from the surface of the film, which results in a lower value for the measured reflectance and transmittance.

In order to make the surface smooth, a drop of oil was added on the sample surface, and the transmittance measurements were repeated for the same sample. It was observed that the transmittance increased by 20% and was similar to that of the calculated value. The fringes disappeared since the new thickness, which is the sum of the thickness of the film layer and the oil layer, has a very high value. Thus, it is believed that the fit would describe the transmission of a smooth film accurately.

Fig. 7.20 shows the transmittance, reflectance and fits of the multilayered structure ZnS/ATO/ITO/Glass. The best fit for the reflectance and transmittance were obtained when the thicknesses of the ZnS, ATO and ITO layers were 0.003 μm, 0.2278 μm and 0.37002 μm, respectively.

Fig. 7.21 shows the transmittance, reflectance and fits of the amorphous multilayered structure Ce:$CaGa_2S_4$/ZnS/ATO/ITO/glass. The parameters obtained from the oscillator fit method for the thin films of amorphous Ce:$CaGa_2S_4$ are shown in Table 6.1. The best fit for the reflectance and transmittance is obtained when the thicknesses of the Ce:$CaCa_2S_4$, ZnS, ATO and ITO layers were 0.4878 μm, 0.003 μm, 0.2818 μm and 0.3176 μm, respectively. This sample was annealed and the measurements and analysis were repeated. Fig. 7.24 shows the transmittance, reflectance and fits of the polycrystalline multilayered structure Ce:$CaCa_2S_4$/ZnS/ATO/ITO/glass

The parameters obtained from the oscillator fit method for the thin films of amorphous Ce:CaGa$_2$S$_4$ are shown in Table 6.2.

Discussion

The optical properties of the TFEL device based on calcium thiogallate thin films were determined by measuring the reflectance and transmittance. In order to model the measured reflectance and transmittance, the reflectance and transmittance of the substrate and the intermediate layers, ITO, ATO and ZnS were measured and the optical constants were determined. The bandgap of the substrate, Corning 7059 glass, was determined from the absorption spectra, by the method described in chapter III, and was found to be 4.4 eV.

The bottom electrode which is ITO had a bandgap of 4.22 eV. The high reflectance in the far infrared region for the ITO films indicate the presence of free carriers in this layer. ATO, the insulator had a bandgap which was much higher than the bandgap of the substrate. The far infrared region of ATO was dominated by phonon modes. ZnS layer in the TFEL device structure has a thickness of 30Å which was obtained by fitting the reflectance and transmittance of the thin films. Thin films of ZnS studied had a bandgap of 4.03 eV. The bandgaps of the materials used in the TFEL structure is tabulated in Table. 7.6.

The bandgap of ZnS reported in literature, (3.48 eV to 3.70 eV), is lower than that of the MOCVD grown ZnS thin films characterized in the present study. This is because those investigators calculated bandgap by using α as the ordinate. More accurate values can be obtained by using $(\alpha h\nu)^2$ as the ordinate. For instance, in the case of manganese doped ZnS, the bandgap should decrease with increasing manganese concentration, since the bandgap of ZnS is higher than the bandgap of MnS.[153] However an increase in bandgap with manganese doping was reported by Bylsma et al.[154] In the present study we have abseved a decrease in the bandgap due to manganese

Table. 7.6. Bandgap of the materials studied.

Materials	Frequency (cm^{-1})	Photon energy (eV)
Corning 7059 glass	35,500	4.40
ITO (thin film)	34,000	4.22
ATO (thin film)		
ZnS (thin film)	32,500	4.03
Ce:CaGa$_2$S$_4$ (amorphous films)	29,100	3.61
Ce:CaGa$_2$S$_4$ (polycrystalline films)	32,900	4.08
Ce:CaGa$_2$S$_4$ (crystals)	28,000	3.47
Ce:CaGa$_2$S$_4$ (TFEL)	32,900	4.08

doping as expected, but contrary to what was reported by Bylsma et al., by using a better approach for obtaining the bandgap which is discussed in Appendix B.

From Fig. 7.1 it was observed that the reflectance is very high in the far infrared region, for the TFEL device. This showed the presence of free carriers, which comes from the ITO layer. The band gap for the TFEL device is at 32,900 cm^{-1} (4.08 eV), as shown in Fig. 7.2. The band gap of polycrystalline thin films of calcium thiogallate were 4.08 eV, which was discussed in chapter VI. Thus it can be seen that the band gap for the thin film device is the band gap of the layer which has the lowest band gap, which was the thin film of polycrystalline calcium thiogallate doped with cerium. Thus the far infrared properties of the thin film device structure was dominated by ITO and the band gap was determined by the cerium doped calcium thiogallate layer.

For a single layer of thin film on glass substrate the calculated reflectance and transmittance are in excellent agreement with the measured reflectance and transmittance. For multilayers on glass substrate, the fringe spacing of the calculated spectra and the measured spectra were in excellent agreement which showed that the thickness assumed for the various layers were accurate. But the calculated spectra deviated slightly from the measured spectra, due to the fact that the fit used an abrupt interface model. A better fit needs additional spatial variation near the interface.

For multi layers of ATO/ITO/glass and TFEL device, a very strong phonon mode was observed at 1,020 cm^{-1}, which is the phonon mode from the ATO layer. But in the measured spectra, this phonon was screened by the free carriers. The far infrared reflectance spectra of the ATO/ITO/glass and amorphous TFEL were very similar. This shows that with the addition of a third or fourth layer, the values of lattice and free carrier parameters in each layer became satisfactorily close to the measured results. But the measured reflectance of the crystalline TFEL device was much lower than the calculated reflectance in the far infrared region which shows that annealing of the TFEL device reduced the total number of free carriers in the device.

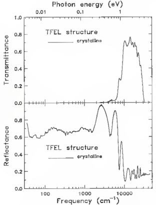

Fig 7.1(a) The upper panel shows the measured transmittance of the device structure at 300k. (b) The lower panel shows the reflectance measured on the same sample

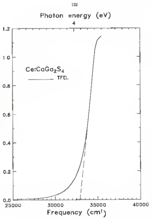

Fig. 7.2 $(\alpha h\nu)^2$ as a function of photon energy of device.

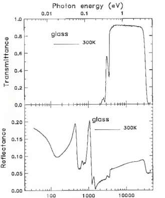

Fig. 7.3(a) The upper panel shows the measured transmittance of Corning 7059 glass substrate at 300 K. (b) The lower panel shows reflectance measured on the same sample.

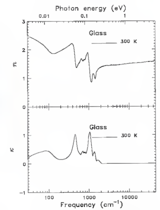

Fig 7 4(a) The upper panel shows the refractive index of Corning 7059 glass
(b) Lower panel shows the extinction coefficient of the same sample

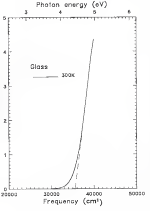

Fig. 7.5 $(\alpha h\nu)^2$ as a function of photon energy of glass

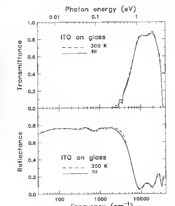

Fig. 7.6(a). The upper panel shows the measured transmittance and oscillator fit of a 0.14 μm thick ITO film on glass substrate at 300 K. (b) The lower panel shows the fit and the reflectance measured on the same sample.

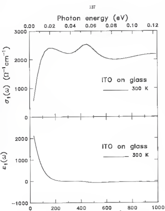

Fig. 7.7(a) The upper panel shows the real part of the complex conductivity
(b) The lower panel shows the real part of the complex dielectric function.

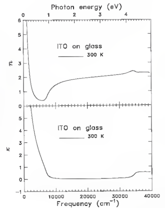

Fig 7 8(a) The upper panel shows the refractive index. (b) Lower panel shows the extinction coefficient in the visible region

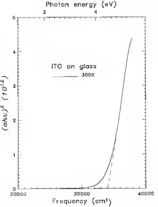

Fig 7.9 $(\alpha h\nu)^2$ as a function of photon energy of ITO

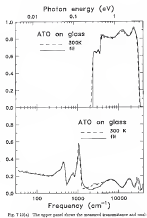

Fig. 7 10(a) The upper panel shows the measured transmittance and oscillator fit of a 0 23 μm thick ATO film on glass substrate at 300 K (b) The lower panel shows the fit and the reflectance measured on the same sample

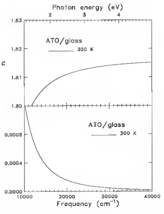

Fig 7 11(a) The upper panel shows the refractive index. (b) Lower panel shows the extinction coefficient in the visible region

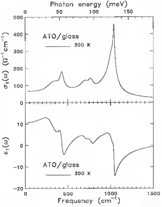

Fig 7.12(a) The upper panel shows the real part of the complex conductivity
(b) The lower panel shows the real part of the complex dielectric function

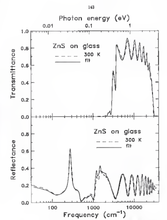

Fig 7.13(a) The upper panel shows the measured transmittance and oscillator fit of a 0.66μm thick ZnS film on glass substrate at 300 K. (b) The lower panel shows the fit and the reflectance measured on the same sample

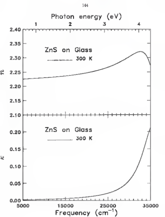

Fig. 7.14(a). The upper panel shows the refractive index. (b) Lower panel shows the extinction coefficient in the visible region.

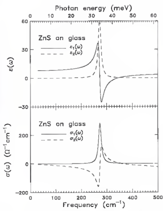

Fig. 7.15(a) The upper panel shows the complex dielectric function. (b) The lower panel shows the complex conductivity

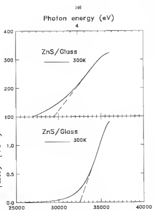

Fig. 7.16(a) α as a function of photon energy (b) $(\alpha h\nu)^2$ as a function of photon energy

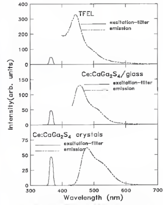

Fig 7.17(a) Photoexcitation and emission spectra of Ce:CaGa$_2$S$_4$ based device structure (b) Photoexcitation and emission spectra of thin films of Ce:CaGa$_2$S$_4$ on glass substrate (c) Photoexcitation and emission spectra of single crystals of Ce:CaGa$_2$S$_4$

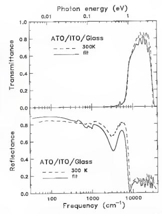

Fig 7.18(a) The upper panel shows the measured transmittance and oscillator fit of the multilayer ATO/ITO/glass at 300 K (b) The lower panel shows the fit and the reflectance measured on the same sample.

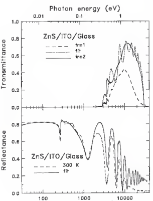

Fig. 7 19(a) The upper panel shows the measured transmittance and oscillator fit of the multilayer ZnS/ITO/glass at 300 K (b) The lower panel shows the fit and the reflectance measured on the same sample

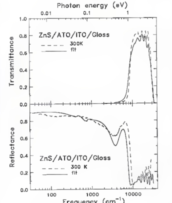

Fig. 7.20(a)- The upper panel shows the measured transmittance and oscillator fit of the multilayer ZnS/ATO/ITO/glass at 300 K (b) The lower panel shows the fit and the reflectance measured on the same sample.

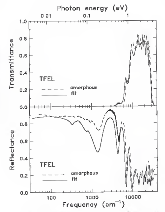

Fig 7.21(a) The upper panel shows the measured transmittance and oscillator fit of the multilayer Ce CaGa$_2$S$_4$/ZnS/ATO/ITO/glass (amorphous) at 300 K (b) The lower panel shows the fit and the reflectance measured on the same sample

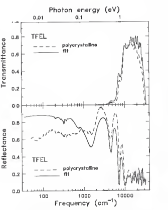

Fig. 7.22(a). The upper panel shows the measured transmittance and oscillator fit of the multilayer Ce CaGa$_2$S$_4$/ZnS/ATO/ITO/glass (polycrystalline) at 300 K. (b). The lower panel shows the fit and the reflectance measured on the same sample.

CHAPTER VIII
OPTICAL STUDIES OF THIN FILMS OF CERIUM DOPED STRONTIUM SULPHIDE

SrS (IIa–VIb) is a promising host material for color thin film electroluminescent devices. Ce:SrS is an efficient blue light emitting phosphor. Devices based on these materials have demonstrated a luminous efficiency of 1.6 lm/W. The reflectance and transmittance of thin films of Ce:SrS sputter deposited on a silicon substrate was measured in the infrared region for the as deposited SrS thin films, doped with 0.1 at wt% cerium. It had been reported that post deposition annealing improves the luminance and efficiency of the Ce:SrS thin films [155]. Annealing of the SrS thin films deposited on silicon substrate was done in hydrogen sulphide atmosphere at 350 °C for 3 hours. Measurements were repeated on the same sample after annealing to study the effect of annealing on the optical characteristics of the Ce:SrS thin films. From the infrared spectra, the optical phonon frequencies and other related dispersion parameters were determined.

In addition to Ce:SrS on silicon substrate, the reflectance and transmittance for the thin films of CeF$_3$:SrS deposited on a glass substrate and a CeF$_3$:SrS based device structure were also measured over the frequency range between far-infrared and visible. The measured reflectance and transmittance were then modelled to determine the thickness, optical properties and other parameters of the thin films. The bandgap obtained from the absorption spectra was compared with the results reported by Kaneko et al [156] for the strontium sulphide single crystals.

The Ce:SrS devices have a double-insulating sandwich structure, similar to that shown in Fig 2.1. The phosphors were grown on glass substrates and had layers of sputtered ITO followed by ATO insulator films. The Ce:SrS phosphor layer was sandwiched between ZnS layers to provide a buffer between SrS and the oxide layers. SrS has high oxygen affinity and hence the ZnS buffer layers isolates SrS from the oxide insulators, and from air [107] Thickness of the ZnS layer on the ATO side is 20Å and on the other side is 1000Å

Results

Optical Properties of Ce:SrS Deposited on Silicon Substrate

Fig. 8.1 shows the far infrared transmittance and reflectance of the as deposited Ce SrS thin films deposited on silicon substrate and the fits to the experimental data, obtained from a set of oscillator parameters using the classical oscillator method Fig 8.2 shows the reflectance, transmittance and fits to the experimental data for the same sample after annealing. A very strong phonon was observed so the reflectance and transmittance spectra at 190 cm^{-1} for the unannealed thin film, whereas the phonon mode was shifted towards higher frequency region by 6 cm^{-1} for the annealed thin film

The real and imaginary part of the complex dielectric function obtained using the oscillator parameters used to fit the reflectance and transmittance in the far infrared region are shown in Fig. 8.3. The LO frequency was determined using Drude's model which consists of finding the frequency at which the real part of the dielectric function goes through zero The TO frequency was determined from the position of the maximum in the imaginary part of the dielectric response function. The values of TO and LO frequencies so obtaiand are at 190 cm^{-1} and 237 cm^{-1} for the as-deposited thin film, and 196 cm^{-1} and 255 cm^{-1} for the annealed Ce:SrS thin films The static dielectric constant of the as deposited SrS Ce thin films is 7.12 and that of the annealed SrS thin films is 7 82

Table. 8.1 Parameters of Lorentz fit to the far infrared reflectance and transmittance of Ce:SrS

Oscillators	ω_{pj} (cm^{-1})	$\omega_j(\omega_{TO})$ (cm^{-1})	γ_j (cm^{-1})	ω_{LO} (cm^{-1})
Ce:SrS as deposited $\epsilon_\infty=4$ Thickness=3500Å	300	190	18	237
Ce:SrS after annealing $\epsilon_\infty=4$ Thickness=10000Å	350	196	12	255

Table. 8.1 shows the oscillator parameters used in fitting the reflectance and transmittance in the far infrared region, and the TO and LO phonon frequencies for the as-deposited and annealed Ce:SrS thin films.

The optical constants of the silicon substrate were determined in the same frequency region prior to the analysis of the film by measuring the reflectance and transmittance, which is shown in Fig. 8.4. In the far-infrared region, fringes appear due to multiple internal reflectance in the substrate. The thickness of the silicon substrate can be precisely determined from a fit with the interference spectrum, and is found to be 0.030 cm. The refractive index and extinction coefficient of the silicon substrate were obtained by the inversion of the equations for reflectance and transmittance and are shown in Fig. 8.5. Refractive index of silicon reported is 3.42 at 3000 cm^{-1},[78] whereas the refractive index of the silicon substrate characterized in the present study is 3.59 eV at 3000 cm^{-1}.

Optical Properties of SrS:CeF$_3$ Deposited on a Glass Substrate

The reflectance and transmittance of SrS:CeF$_3$ thin films deposited on glass substrates were measured over a wide frequency range from 30 cm^{-1} to 45 000 cm^{-1} (4 meV to 5.58 eV) using the Bruker 113v Fourier-transform spectrometer and the microscope photometer with grating monochromators. The classical oscillator model is used to determine the optical properties of the thin film, which permits the determination of the optical constants from the experimental data with a very good accuracy. This was done by fitting the measured reflectance and transmittance using the same set of oscillator parameters from which the thickness and other optical constants of the thin films were determined.

Fig. 8.6 shows the transmittance and reflectance of SrS:CeF$_3$ deposited on glass substrate and the fits to the experimental data. The substrate optical constants were determined in the same frequency region prior to the analysis of the film, by measuring the reflectance and transmittance. The substrate used was Corning 7059 and the optical properties of this substrate were discussed in Chapter VII. In the far-infrared region, a very strong phonon at 197 cm^{-1} is observed. Above 1000 cm^{-1} fringes appear due to multiple internal reflectance in the thin film. The optical feature at 689 cm^{-1} and 1040 cm^{-1} are the phonon modes of the substrate. The thickness of the thin film is precisely determined from a fit with the interference spectrum. It was found that the thickness for this sample was not uniform. In the region where the reflectance was measured the thickness of the sample was found to be 11,400Å and in the region where the transmittance was measured, the thickness was found to be 9,200Å.

The real and imaginary part of the complex dielectric function obtained using the above data in the far infrared region are shown in Fig. 8.7. The longitudinal optic phonon (LO) and the transverse optic phonon (TO) frequencies along with the fitting oscillator parameters are tabulated in Table. 8.2. The LO frequency was determined using Drude's model using the techniques described previously. The values of TO and LO frequencies are at 197 cm^{-1} and 304 cm^{-1}. The values obtained for ϵ_∞ and ϵ_0 are 4 and 8.4, respectively, which are obtained by fitting the experimental reflectance and transmittance. These values satisfy the Lyddane-Sachs-Teller relation given by Equ. 42. Table. 8.2 shows the oscillator parameters and the TO and LO phonon frequencies for the CeF$_3$ SrS thin film deposited on glass substrate.

Table. 8.2. Parameters of oscillator fit to the reflectance and transmittance of CeF$_3$ SrS thin film deposited on glass substrate

Oscillators	ω_{pj} (cm^{-1})	$\omega_j(\omega_{TO})$ (cm^{-1})	γ_j (cm^{-1})	ω_{LO} (cm^{-1})
Phonon transition	459	197	16.8	304
Interband	3,000	35,000	500	
transitions	5,000	37,000	3,000	
	5,000	38,000	2,000	
	5,000	43,000	40,000	
ϵ_∞=4.0				
thickness=0.82 μm				

The dispersion of refractive index and extinction coefficient SrS CeF$_3$ is shown in Fig. 8.8. The refractive index had a value of 2.014 at 12,000 cm^{-1} and 2.022 at 25,000 cm^{-1}. The extinction coefficient was very low in the visible region, since there is very little absorption. The extinction coefficient is 0.0012 at 12,000 cm^{-1} and 0.0039 at 25,000 cm^{-1}.

The optical energy gap E_g of SrS:CeF$_3$ was determined from the optical absorption coefficient $\alpha(\omega)$ and the incident photon energy $h\nu$ using Eqn. 2.4. SrS:CeF$_3$ had an indirect energy band gap structure, since $(\alpha h\nu)^{0.5}$ increased sharply as a function of the incident photon energy, which is shown in Fig. 8.9. Extrapolation to zero gives an estimate of optical energy bandgap of 34,500 cm^{-1} (4.28 eV). This is tabulated in Table. 8.3. SrS:CeF$_3$ has almost no absorption from the fundamental bandgap down to the infrared region at around 197 cm^{-1} where strong absorption from the optical phonon occurs.

Table 8.3 compares the LO and TO phonon frequencies and bandgap for the Ce:SrS thin films deposited on silicon substrate, SrS:CeF$_3$ thin films deposited on glass substrate, and SrS single crystals reported by Kaneko et al.[156] The thin films of CeF$_3$:SrS agrees with the single crystals of SrS better than the SrS:Ce thin films deposited on silicon substrate. This shows that there is stress developed in the thin films of Ce:SrS deposited on silicon substrate.

Optical Properties of Ce:SrS Based Device Structure

(SrS/ZnS)$_n$ is a new multi layered thin film electroluminescent phosphor material which shows superior electrical and optical characteristics when compared to individual ZnS and SrS thin films.[69,168] The main problem in rare earth doped ZnS thin films is the low solubility of the rare earth ions in the ZnS host lattice. In SrS thin films, chemical instability due to its hydroscopic nature becomes the problem. These problems were overcome in the SrS:Ce device structure in which there are three semiconductor layers, ZnS/Ce:SrS/ZnS. ZnS protects the SrS layer from the underlying oxide layers, and from air, since SrS has a high affinity for oxygen.

The optical properties of ZnS/ATO/ITO/glass were discussed in Chapter VII. Fig. 8.10 shows the reflectance and transmittance and fits to the experimental data

Table. 8.3 Parameters of Lorentz fit to the reflectance and transmittance of Ce:SrS and CeF$_3$:SrS thin films and SrS single crystals

	ϵ_∞	ϵ	Bandgap eV	ω_{TO} (cm^{-1})	ω_{LO} (cm^{-1})
As deposited					
Ce:SrS thin film	4	7.12	-	190	237
Annealed					
Ce:SrS thin film	4	7.82	-	196	255
Single crystals					
of SrS	4	9.47	4.32	185	282
As deposited					
CeF$_3$:SrS	4	9.4	4.36	197	304

of the ZnS/SrS:Ce multilayered structure, deposited on a glass substrate. The reflectance and transmittance were fitted by fixing the optical parameters of ZnS shown in Table. 7.4 and the optical parameters of Ce:SrS shown in Table. 8.2 and varying only the thicknesses.

Fig. 8.11 shows the variation of $(\alpha h\nu)^2$ as a function of frequency, for the SrS:Ce based device structure. By extrapolation to zero, the optical energy bandgap of the thin films of SrS:CeF$_3$ was found to be 32,000cm^{-1} (3.98 eV). This is the bandgap of the layer which has the lowest bandgap, which is ZnS.

Discussion

The far infrared optical properties of Ce:SrS deposited on silicon substrate were determined. The results show a higher degree of crystallinity for the Ce:SrS thin films deposited on silicon substrate, than before annealing. For the as deposited thin films, the phonon mode observed was at 190 cm^{-1}. For the annealed thin films, the phonon was shifted towards the higher frequency region by 6 cm^{-1}. The sharp vibrational feature of the annealed films show that there is long range crystalline order. This shows that the annealed thin films have a higher degree of orientation of the SrS grains. The phonon mode in the annealed films had a higher density of states and was sharper than that of as-deposited SrS thin films. The oscillator strength is greater and the linewidth is lower for the annealed versus as deposited thin films.

The bandgap of the SrS:CeF$_3$ thin films deposited on glass substrate was very close to the bandgap of the SrS single crystals. This is because cerium centers doped in the SrS lattice have the 4f ground state level in the forbidden gap and the 5d excited states were fairly close to the conduction band minimum at the X point. Hence doping SrS with cerium centers does not alter the bandgap of strontium sulphide significantly.

For the SrS:Ce based device structure, a direct bandgap is expected. For multilayered structure, the observed bandgap is that of the layer having the lowest bandgap. Since ZnS had a lower bandgap compared to Ce:SrS, the bandgap was expected to be that of ZnS. This expectation is correct since the ZnS/SrS:Ce/glass was found to have a bandgap of 33,000 cm^{-1} (4.08 eV), which is the same as that of ZnS.

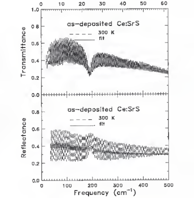

Fig. 8.1. The upper panel shows the measured transmittance and oscillator fit of a as-deposited 3500Å thick Ce:SrS thin film on silicon substrate at 300 K. The lower panel shows the fit and the reflectance measured on the same sample

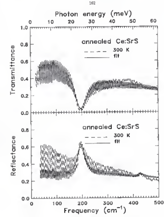

Fig 8 2 The upper panel shows the measured transmittance and oscillator fit of a annealed 8500Å thick Ce SrS thin film on silicon substrate at 300 K The lower panel shows the fit and the reflectance measured on the same sample.

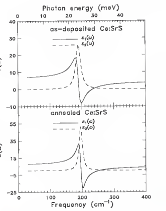

Fig. 8.3 The real and imaginary part of the complex dielectric function of as-deposited and annealed Ce:SrS thin films

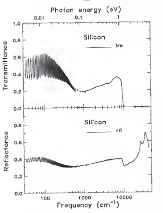

Fig 8 4 The transmittance and reflectance of the 0.03 cm thick silicon substrate

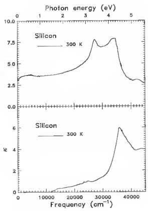

Fig 8.5 The refractive index and extinction coefficient of the silicon substrate

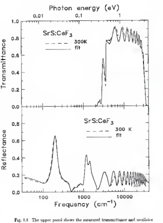

Fig. 8.6 The upper panel shows the measured transmittance and oscillator fit of a SrS:CeF$_3$ film on glass substrate at 300 K. The lower panel shows the fit and the reflectance measured on the same sample.

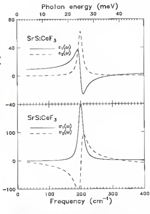

Fig. 8.7 The upper panel shows the real and imaginary part of the complex dielectric function of SrS CeF$_3$ and the lower panel shows the real and imaginary part of the complex conductivity of SrS CeF$_3$

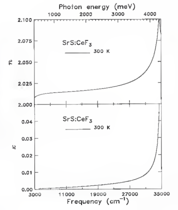

Fig. 8.8 The upper panel shows the refractive index n and the lower panel shows the extinction coefficient κ of the SrS CeF$_3$ thin films

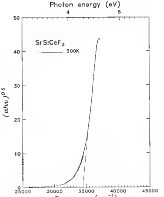

Fig 8.9 $(\alpha h\nu)^{0.5}$ as a function of frequency for SrS CeF$_3$

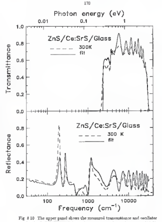

Fig 8 10 The upper panel shows the measured transmittance and oscillator fit of a ZnS/SrS:Ce multilayered structure on glass substrate at 300 K The lower panel shows the fit and the reflectance measured on the same sample.

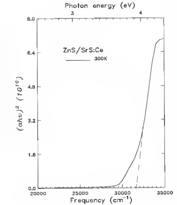

Fig 8.11 $(\alpha h\nu)^2$ as a function of frequency for ZnS/SrS:Ce

CHAPTER IX
SUMMARY AND CONCLUSIONS

This dissertation is devoted to an extensive study of the infrared and optical properties of cerium doped calcium thiogallate and strontium sulphide phosphors, by measuring the reflectance and transmittance from 30 cm^{-1} to 48000 cm^{-1}. The objective of this study was to characterize the thin films of these phosphor materials by developing a model for the reflectance and transmittance of a single layer of thin film deposited on a thick glass or silicon substrate, as well as multilayers. The optical properties of the thin films were then compared with that of the bulk crystalline phosphor material. The bandgap energies and type of the materials studied are summarized in Table. 9.1.

Measurements were done on both the undoped and cerium doped single crystals of $CaGa_2S_4$. The undoped single crystals were strongly anisotropic, whereas the doped crystals were isotropic due to its polycrystalline nature. The photoluminescence of the undoped crystals was very noisy and the intensity was very low, compared to that of the doped crystals. The emission occurred from regions where there was an excess of sulphur and deficiency of gallium. The emission spectra of the doped single crystals showed overlapping double bands from the radiative transition of cerium from its excited state to the ground state.

The absorption spectra of the doped calcium thiogallate crystals showed a very strong absorption between 22,000 cm^{-1} and 25,000 cm^{-1} which is the absorption of cerium into its excited state. Since emission follows absorption, the strong absorption of the doped samples explains the luminescent nature of the cerium doped crystals. In addition to the cerium absorption, a very strong absorption was seen for the doped

Table 9.1 Bandgap of the materials studied

Materials	Frequency (cm^{-1})	Photon energy (eV)	Type
Corning 7059 glass	35,500	4.40	Direct
ITO (thin film)	34,000	4.22	Direct
ATO (thin film)			Direct
ZnS (thin film)	32,500	4.03	Direct
Mn ZnS (thin film)	30,000	3.72	Direct
Ce:$CaGa_2S_4$ (amorphous films)	29,100	3.61	Direct
Ce:$CaGa_2S_4$ (polycrystalline films)	32,900	4.08	Direct
Ce:$CaCa_2S_4$ (crystals)	28,000	3.47	Direct
$CaCa_2S_4$ (single crystals)	32,500	4.03	Direct
Ce:$CaGa_2S_4$ (TFEL)	32,900	4.08	Direct
Ce:SrS (thin films)	34,500	4.28	Indirect
ZnS/Ce:SrS (multilayer)	31,750	3.94	Direct

crystals above 27,500 cm^{-1}, which was the absorption near the bandedge of the impurity, Ga_2S_3. For the undoped $CaGa_2S_4$ single crystals, the direct bandgap obtained from optical measurements was 4.03 eV. The bandgap of the cerium activated phosphor was much lower at 3.47 eV, which is close to the bandgap of Ga_2S_3, (3.31 eV), a known impurity in the $Ce:CaGa_2S_4$. The lower bandgap of the doped phosphor resulted in a higher refractive index compared to that of the undoped single crystals, due to this impurity.

Calculation of the optical constants of a thin film is complicated since the film is deposited on a substrate. We were successful in developing a model to fit the reflectance and transmittance of a single layer of a thin film on a thick substrate. Accurate values of optical constants were obtained for thin films of phosphors deposited on a thick substrate. These values were obtained from a set of classical oscillator parameters used to fit both the reflectance and transmittance. The thickness of the thin films were also precisely determined, since the thickness was also an input parameter in fitting the measured data.

The bandgap of the amorphous cerium doped calcium thiogallate thin films deposited on a glass substrate is 4.08 eV, which is very close to that of the bulk crystals. The bandgap of the amorphous thin films is 3.61 eV, which is lower than that of the polycrystalline thin films and led to a higher refractive index of 2.16 for the amorphous thin films. Sharp vibrational features were observed for the polycrystalline thin films which indicated good long range order of the atoms. In addition to the breadth of the features observed, amorphous thin films had fewer phonon modes as compared to the polycrystalline thin films. The calculated reflectances of the polycrystalline thiogallate thin films were higher than the measured reflectances. This difference between the measured and the calculated values is a result of scattering, due to surface roughness and grain boundary scattering in the polycrystalline thin films.

In order to determine the optical properties of the TFEL device based on calcium thiogallate thin films, the reflectance and transmittance of the substrate and the intermediate layers (ITO, ATO and ZnS) were measured and the optical constants were determined. The bandgap of the substrate, which is Corning 7059 glass, was determined from the reflectance and transmittance spectra and found to be 4.40 eV. The bottom electrode, ITO, had a bandgap of 4.22 eV. The high reflectance in the far infrared region for the ITO films indicate the presence of free carriers in this layer. ATO, which is the insulator, had a bandgap which was much higher than the bandgap of the substrate. The far infrared region of ATO was dominated by phonon modes. It was observed that the far infrared properties of the thin film device structure was dominated by ITO and the band gap was determined by the Ce:$CaGa_2S_4$ thin films, since this material has the lowest bandgap.

ZnS layer in the TFEL device structure had a thickness of 30 Å, and these layers help nucleate the growth of the polycrystalline phosphor layer. Thin films of ZnS studied had a bandgap of 4.03 eV. This value of bandgap determined in the present study was higher than the bandgap reported in the literature for ZnS, (3.6 eV for Zinc blende and 3.7 for wurtzite). One reason for the lower bandgap reported was due to the calculation of bandgap from α by these investigators. A better value for the bandgap is obtained by taking $(\alpha h\nu)^2$ as the ordinate. A lower value for the bandgap of ZnS was obtained by plotting α as the ordinate, as shown in Fig. 7.16(a).

The bandgap of the SrS:CeF_3 thin films deposited on glass substrate were determined to be 4.36 eV, which is similar to that of the SrS single crystals, reported by Kaneko et.al.(4.28 eV). This is because when cerium centers were doped in the SrS lattice, the 4f ground state level lies in the forbidden gap and the 5d excited states were fairly close to the conduction band minimum at the X point. Hence doping SrS with cerium centers did not alter the bandgap of strontium sulphide.

The far infrared optical properties of Ce:SrS deposited on a silicon substrate before and after annealing were determined. The sharp vibrational feature of the annealed films showed that there is long range crystalline order in the annealed films. A shift in the phonon mode of the annealed thin films towards higher frequency region was observed which shows that they have a higher degree of orientation of the SrS grains compared to the as deposited thin films. From the absorption studies of the multilayered structure, ZnS/SrS:Ce/glass, the bandgap was 33,000 cm^{-1} (4.08 eV) which is determined by ZnS.

For a single layer of thin film on a glass substrate, the calculated reflectance and transmittance were in excellent agreement with the measured reflectance and transmittance. The fringe spacing of the calculated spectra and the measured spectra were in good agreement, for the multi layered structure which showed that the thickness assumed for the various layers were accurate. But the calculated spectra deviated slightly from the measured spectra, due to the fact that the fit used an abrupt interface model. A better fit needs additional spatial variation near the interface. The difference between the calculated reflectance and the measured reflectance is a function of the absorption at the interface between the different layers.

The model was successful in calculating the bandgap of the device structure consisting of layered thin films. For the case of the multilayered structure, ZnS/ITO/Glass shown in Fig. 7.19, initial calculation for the bandgap would lead to erroneous results (3.47 eV), since the transmittance is very much decreased by scattering arising from surface roughness. Since the optical properties of each layer constituting the structure is known, we were able to obtain a better value for the bandgap, (4.03 eV) by repeating the measurements, taking scattering into account

APPENDIX A

OPTICAL PROPERTIES OF $LiAlO_2$ and $LiGaO_2$

Appendix A describes the experimental studies on the infrared optical properties of two perovskite materials $LiAlO_2$ and $LiGaO_2$. $LiAlO_2$ and $LiGaO_2$ are possible substrates for depositing thin films of gallium nitride (GaN). Room-temperature reflectance and transmittance measurements were made over the spectral range of 30 cm^{-1} to 45000 cm^{-1} (4 meV–5.58 eV).

One of the main difficulties in developing GaN as an electronic material is the lack of a closely lattice matched substrate. Most of the research on a suitable substrate for GaN was concentrated on sapphire and silicon carbide. Recently alternative substrates such as $LiGaO_2$ and $LiAlO_2$ have been suggested and initial growth experiments on them have been carried out.[159,160] $LiGaO_2$ is closely lattice matched to GaN, having a mismatch of less than 1% in the basal plane lattice constant a.

$LiGaO_2$ is a piezoelectric crystal with 16 atoms per unit cell, which crystallizes in the orthorhombic system with the unit cell parameters: a = 5.402 Å, b = 6.3726 Åand c = 5.007 Åand has $Pna\,2_1$ C_{2v}^9 space-group symmetry.[161] Since there are 16 atoms per unit cell, there are 45 optical phonon modes. Group theory analysis shows that of the 45 phonon modes, 33 are IR active and 12 are Raman active.[162] It has a bandgap of 5 eV. There are four formula units per unit cell and the atoms are arranged in a way that oxygen tetrahedra containing lithium and gallium atoms in the center are alternately edge-linked. Average interatomic Ga-O separation is 1.948 Å and Li-O separation is 1.985 Å.

Fig. A.1 shows the projection of the crystal structure of $LiGaO_2$ on the ab plane. The structure consists of an infinite three dimensional array of tetrahedra having only vertices in common. At the vertices, there are oxygen atoms and at the centers gallium and lithium atoms. Each oxygen is shared among four tetrahedra, two gallium centered and two lithium centered. The same scheme would be obtained if the tetrahedra were drawn by putting the gallium and lithium atoms at the vertices, and the two oxygen atoms at the centers. This shows that in this structure, each atom is tetrahedrally coordinated.[101]

Fig. A.2 and Fig. A.3 show the reflectance and transmittance of a 0.05cm thick $LiGaO_2$ crystal in the far infrared region, for light polarized parallel to a and b axis respectively. Below 200 cm^{-1} fringes appear due to multiple internal reflectance. Between 200 cm^{-1} and 800 cm^{-1}, the crystal is opaque, and the reflectance is dominated by phonon modes. Kramers Kronig analysis of the reflectance spectrum was used to obtain the optical constants in the region of high absorption, where there is no transmittance. In the region of low absorption, the optical constants were obtained by the inversion of the equations for reflectance and transmittance. A Lorentz oscillator model was used to fit the measured data to the model function. Table. A.1 shows the parameters of the Lorentz fit to the reflectance, and the LO and TO phonon frequencies of $LiGaO_2$ crystal.

Fig. A.4 shows the real part of complex conductivity of $LiGaO_2$ crystal in the far infrared region, for light polarized parallel to a and b axis respectively. Low frequency phonon modes are made up of heavier atoms and high frequency modes are made up of lighter atoms. The infrared spectrum of $LiGaO_2$ has 10 well defined phonon modes for light polarized parallel to the a axis, and 11 well defined phonon modes for light polarized parallel to b axis. This shows the correct classification of the phonon modes into the symmetry species. Lithium being lighter than gallium, Table. A 1 Parameters of Lorentz fit to the reflectance of $LiGaO_2$

Oscillators	ω_{pj} (cm^{-1})	ω_j (cm^{-1})	γ_j (cm^{-1})	ω_{TO} (cm^{-1})	ω_{LO} (cm^{-1})
$LiGaO_2$	190	300	6	300	304
a axis	220	314	8	314	322
	520	405	8	405	433
	240	450	8	450	474
	340	501	7	501	543
	170	599	8	599	606
	640	657	2.5	657	706
	125	710	10	710	777
$LiGaO_2$	70	206	1	206	209
b axis	70	251	2	251	253
	150	319	7	318	323
	170	363	4	363	367
	400	432	8	432	445
	250	464	18	464	488
	594	513	8	513	600
	290	652	8	652	706
Thickness=0 05 cm					

phonon modes observed above 550 cm^{-1} were the stretching of the Li-O bonds, the phonon modes observed between 400 cm^{-1} and 550 cm^{-1} were the stretching of the Ga-O bonds and below 400 cm^{-1} were the bending of the Li-O-Ga bonds

Fig A.5 shows the real part of complex dielectric function of $LiGaO_2$ crystal in the far infrared region, for light polarized parallel to a and b axis respectively. Static dielectric constant for light polarized parallel to a and b axis were 7.8 and 6.4 respectively.

$LiAlO_2$ crystallizes in the tetragonal structure with lattice parameters a = b = 5.1687 Å and c = 6.2679 Å. The projection of the crystal structure on the ac plane is shown in Fig A.6. Group theory analysis shows that there are 45 phonon modes of which 28 are IR active and 17 are Raman active. The crystal structure of $LiAlO_2$ is very similar to that of $LiGaO_2$, with each oxygen atom sharing four tetrahedra, two gallium centered and two aluminum centered.

Fig. A.7 and Fig A.8 show the reflectance and transmittance of a 0.05 cm thick $LiAlO_2$ crystal in the far infrared region, for light polarized parallel and perpendicular to c axis respectively. Below 200 cm^{-1} fringes appear due to multiple internal reflectance. Between 200 cm^{-1} and 1,000 cm^{-1}, the reflectance is dominated by phonon modes.

Fig A.9 shows the real part of complex conductivity of $LiAlO_2$ crystal in the far infrared region, for light polarized parallel and perpendicular to c axis respectively. Lithium being lighter than aluminum, the phonon modes observed above 650 cm^{-1} were the stretching of the Li-O bonds, the phonon modes observed between 450 cm^{-1} and 650 cm^{-1} were the stretching of the Ga-O bonds and below 450 cm^{-1} were the bending of the Li-O-Al bonds. Table. A.2 shows the parameters of the Lorentz fit to the reflectance, and the LO and TO phonon frequencies of $LiAlO_2$ crystals.

Fig A.10 shows the real part of complex dielectric function of $LiAlO_2$ crystal in the far infrared region, for light polarized parallel to a and b axis respectively. Static

Table. A.2. Parameters of Lorentz fit to the reflectance of $LiAlO_2$

Oscillators	ω_{pj} (cm^{-1})	ω_j (cm^{-1})	γ_j (cm^{-1})	ω_{TO} (cm^{-1})	ω_{LO} (cm^{-1})
$LiAlO_2$	68	161	2	161	192.4
c axis	289	277	6	277	289
	340	322	3.5	322	339
	280	361	3	361	387
	300	446	4.5	446	468
	420	536	10	536	602
	250	673	30	673	679
	700	799	9	799	841
	100	843	16	843	939
$LiAlO_2$	161.5	276	2	276	283.5
ab plane	350	473	40	473	488.5
	404	510	6	510	539.5
	480	636	12	636	681
	630	780.5	5	780.5	933
Thickness=0.05 cm					

dielectric constant for light polarized parallel and perpendicular to c axis were 6.7 and 8.4 respectively

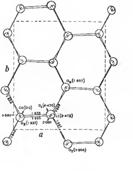

Fig A.1 Projection of the crystal structure of $LiGaO_2$ in the ab plane.

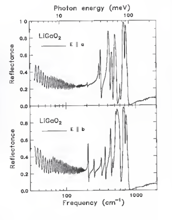

Fig. A 2. Reflectance of a 0.05 cm thick LiGaO$_2$ crystal in the far infrared region, for light polarized parallel to a and b axis respectively

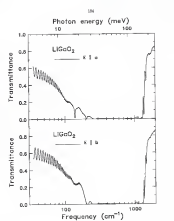

Fig. A.3 Transmittance of a 0.05 cm thick LiGaO$_2$ crystal in the far infrared region, for light polarised parallel to a and b axis

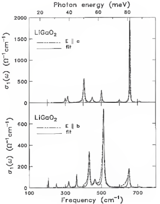

Fig. A.4 Real part of complex conductivity of $LiGaO_2$ crystal in the far infrared region, for light polarized parallel to a and b axis respectively

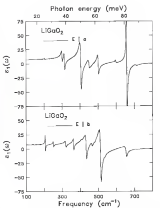

Fig. A 5 Real part of complex dielectric function of $LiGaO_2$ crystal in the far infrared region, for light polarized parallel to a and b axis respectively

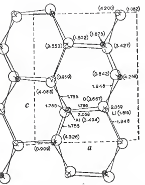

Fig. A 8 Projection of the crystal structure of $LiAlO_2$ in the ac plane.

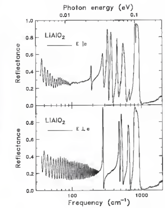

Fig. A.7. Reflectance of a 0.05 cm thick $LiAlO_2$ crystal in the far infrared region, for light polarized parallel and perpendicular to c axis respectively.

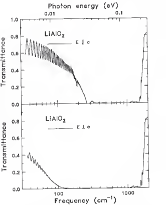

Fig. A.8 Transmittance of a 0.05 cm thick LiAlO$_2$ crystal in the far infrared region, for light polarized parallel and perpendicular to c axis respectively.

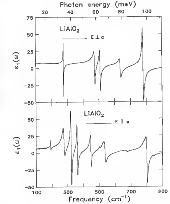

Fig. A 9 Real part of complex conductivity of LiAlO$_2$ crystal in the far infrared region, for light polarized parallel and perpendicular to c axis respectively

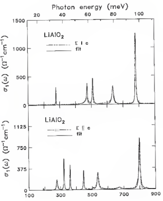

Fig. A 10 Real part of complex dielectric function of LiAlO$_2$ crystal in the far infrared region for light polarized parallel to a and b axis respectively

APPENDIX B

OPTICAL PROPERTIES OF MANGANESE DOPED ZINC SULPHIDE

Manganese doped zinc sulphide (Mn:ZnS) is one of the most studied materials for flat panel displays. ZnS is a semiconductor suitable to be used as host matrix for a large variety of dopants because of its wide energy bandgap. The optical properties of ZnS was discussed in Chapter VII. Mn:ZnS is the most common light-emitting material in thin film electroluminescent displays. Appendix B presents optical properties of thin films of Mn:ZnS deposited on Corning 7059 glass substrate. The optical properties of Corning 7059 glass was discussed in Chapter VII. MOCVD grown thin films of Mn:ZnS on glass substrates were prepared at the University of Florida.

Manganese is the most suitable center for ZnS, and fulfills all the requirements as a center for ZnS. Mn^{2+} can be incorporated in high concentrations into the ZnS lattice, upto complete miscibility.[183,184] It has input excitability with large cross section and inner shell transitions well shielded against electric fields. Mn^{2+} substitutes for the Zn^{2+} in the ZnS lattice, and is isovalent.

The reflectance and transmittance of Mn:ZnS were measured from 30 cm^{-1} to 48,000 cm^{-1}. Fig. B.1 shows the experimental reflectance and transmittance of 0.96 μm thick Mn:ZnS film deposited on glass substrate and the fits to the measured data. Above 2,000 cm^{-1} fringes appear due to multiple internal reflectance from the front and back surface of the film.

Fig. B.2 shows the complex dielectric function and complex conductivity of Mn:ZnS in the far infrared region. The TO and LO phonon frequencies of thin films of Mn:ZnS were 273 cm^{-1} and 349 cm^{-1}, respectively. The TO phonon frequency of Mn:ZnS were the same as that of ZnS. But the LO phonon frequency was slightly higher for Mn:ZnS, compared to that for ZnS (349 cm^{-1} versus 345 cm^{-1}). This close similarity of the LO and TO phonon frequencies of ZnS and Mn:ZnS shows that there is not much stress developed in the thin films due to doping with manganese. This is because Mn^{2+} fulfills all the requirements as a luminescent center for ZnS. Table. B.1 shows the oscillator parameters to the Lorentz fit of reflectance and transmittance and the LO and TO phonon frequencies.

Table B.1 Parameters of oscillator fit to the reflectance and transmittance of thin films of Mn:ZnS deposited on glass substrate.

Oscillators	ω_{pj} (cm^{-1})	ω_j (ω_{TO}) (cm^{-1})	γ_j (cm^{-1})	ω_{LO} (cm^{-1})
Phonon transition	520	273	10	349
Interband	9,000	31,000	1,000	
transitions	5,000	35,000	4,388	
	12,000	40,000	9,117	

ϵ_∞=4.9

Thickness of Mn:ZnS=0.96 μm.

Fig. B.3 shows the refractive index and extinction coefficient in the visible region of Mn:ZnS. Refractive index and extinction coefficient are 2.26 and 0.00179 at 10,000 cm^{-1} and 2.304 and 0.0167 at 25,000 cm^{-1} respectively.

Since Mn:ZnS is a direct bandgap material, extrapolation of $(\alpha h\nu)^2$ to zero, gives the bandgap which was determined at 30,000 cm^{-1} (3.72 eV). The bandgap of the host material, ZnS was 4.03 eV, which was discussed in Chapter VII. The lowest unoccupied molecular orbital for cubic ZnS atoms is from the 4s orbitals and the highest occupied molecular orbital is from the 3p orbitals of the sulphur atoms. Manganese as a substitutional dopant in ZnS and with d^5 configuration is in the same state of ionization (+2) as zinc with d^{10} configuration. Substitution of Mn in ZnS give rise to interactions between s-d (zinc-manganese) and p-d (sulphur-manganese), which results in an exchange interaction potential, and this potential is a perturbation potential.[168]

Substitution of manganese in ZnS changes the bandgap, which is consistent with the results reported.[165–168] The observed shift in bandgap is due to the change in eigenvalues as a result of the perturbation potential. The bandgap of Mn:ZnS should decrease with an increase in manganese concentration, because the bandgap of ZnS is higher than that of MnS. But a higher value for the bangap, relative to that of ZnS was reported.[164]

In the present study, by using a better approach to calculate the bandgap, which was discussed in Chapter III, we noticed that the bandgap actually decreased when ZnS was doped with manganese, as expected. This is shown in Fig. B.4 where $(\alpha h\nu)^2$ is plotted as a function of the incident photon energy.

The photoluminescence of Mn:ZnS was measured by using the Microscope Photometer. The samples were excited using a Xenon lamp, from which a narrow band of excitation wavelength was chosen at 465 nm. Fig. B.5 shows the photoexcitation and emission spectra of Mn:ZnS deposited on a silicon substrate. The yellow peak seen in the emission spectra is due to the radiative transition from the $^4T_1 - {}^6A_1$ energy levels of the manganese ion. Studies done on cubic Mn:ZnS[169] and hexagonal Mn:ZnS[170] show emission peaks at 585 nm and 580 nm respectively.

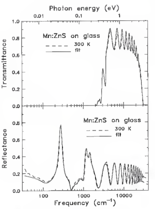

Fig. B.1 Room temperature transmittance, reflectance and fits to the experimental data of Mn:ZnS deposited on glass substrate.

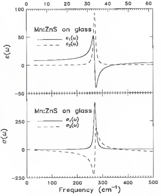

Fig B.2 Complex dielectric function and complex conductivity of Mn:ZnS in the far infrared region.

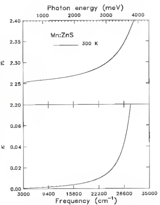

Fig. B 3 Refractive index and extinction coefficient in the visible region of Mn:ZnS

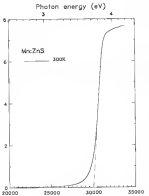

Fig. B 4 $(\alpha h\nu)^2$ as a function of photon energy

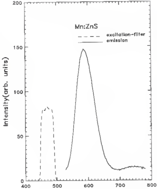

Fig B.5 Photoluminescence spectra of Mn:ZnS when excited with blue light

REFERENCES

1. T.E. Peters, J.A. Baglio, *J. Electrochem. Soc.*, **119**, 230 (1972).

2. G. Blasse, B.C. Grabmaier, *Luminescent Materials*, Springer Verlag (1994).

3. M. Godlewski, M. Leskela, *Critical Review in Solid State and Material Sciences*, **19** 199 (1994).

4. C.N. King, *Int. Conf. on the Sci. and Tech. of Display Phosphors*, 3 (1994).

5. J.C. Manifacier, J. Gasiot, P. Fillard, *J. Phys. E*, **9** (1976).

6. R. Swanepoel, *J. Phys. E*, **16**, 1214 (1983).

7. F. Abeles, M.L. Theye, *Surf. Sci.*, **5**, 325 (1966).

8. J.M. Bennet, M.J. Booty, *Appl. Optics*, **5**, 41 (1968).

9. P.O. Nilsson, *Appl. Optics*, **7**, 435 (1968).

10. J. Nestell, R.W. Christy, *Appl. Optics*, **11**, 643 (1972).

11. S.G. Tomlin, *J. Phys. D*, **2**, 1667 (1968).

12. J.P. Bergogno, B. Lazarides, P. Roche, *Thin Solid Films*, **122**, 209 (1983).

13. R.C. McPhedran, L.C. Botten, D.R. McKenzie, R.P. Netterfield, *Appl. Optics*, **23**, 1197 (1984).

14. E. Elizalde, F. Rueda, *Thin Solid Films*, **122**, 45 (1984).

15. F. Bassani, G.P. Parravicini, *Electronic States and Optical Transitions in Solids*, Pergamon, Oxford (1975).

16 J Meyer-Arendt, *Intro to Classical and Modern Optics, 2nd Edn.*, New Jersey (1984).

17. D P Arndt, R. M. A Azzam J M Bennet, J.P Borgogno, C K Carniglia, W E. Case, J A. Dobrowolski, U J Gibson, T. Tuttlehart, F.C Ho, V A. Hodgkin, W P Klapp, H.A MacLeod E. Pelletier, M K Purvis, D M Quinn, D H Strome, R. Swenson, P.A. Temple, T F Thonn, *Appl Optics*, **23**, 3571 (1984)

18. L Ward et al., *J Phys D*, **2**, 301 (1969)

19 W Hansen, *J Opt. Soc. Am.*, **63**, 793 (1973)

30 E. Dobierzewska-Mozrzymas, S Lewanowicz, J Mozrzymas, *Acta Phys Pol.*, **A41**, 251 (1972)

21. V Kriscunas, V Rinkevicius, *Liet Fiz Rinkinys* , **15**, 447 (1975)

22. J W Allen, *J Magn. Mater.*, **47**, 168 (1985)

23 J Rohler, D Wohlleben, J P Kappler, G Krill, *Phys Lett.*, **103A**, 220 (1984).

24 A. Fujimori, *Phys Rev B* **28**, 2281 (1983)

25. A Bianconi, A Marcelli, M. Tomellini, I. Davoli, *J Magn Mater* , **47**, 209 (1985)

26. P Wachter, H Boppart, *Valence Instabilities*, North Holland, Amsterdam, 145 (1982)

27 W.A. Barrow, R.E Coovert, C N King *SID Digest*, San Francisco, 249 (1984)

28 G L Carr, S Perkowitz, D H Tanner, *Int J Infrared and Millimeter Waves*, **13**, 171 (1985)

29 H Kobayashi, *J Crystal Growth*, **138**, 1019 (1994)

30 T Suyama, K Okamoto, Y Hamakawa, *Appl Phys. Lett.*, **41**, 462 (1982)

31 S Matsumoto, *Electronic Display Devices*, John Wiley and Sons, New York, 182 (1990)

32 K Brennan, *J Appl. Phys* , **64**, 4024 (1988)

33 D Bosman, *Display Engineering, Conditioning, Technologies and Applications*, North Holland (1989)

34 G Steele, E Sussman, *U S Patent* 3, 560, 784 Feb (1971)

35 G Destriau, *J Chem Phys* **33**, 587 (1936)

36 K Hirabayashi, Y Itoh, *J Electrochem Soc* , **129**, 362 (1982)

37 R.E. Halsted, L.R. Koller, *Phys Rev.*, **93**, 349 (1954)

38 J H DeBoer, C.J Dippel, *U S Patent* 1, 954, 691 (1934)

39 W A Thornton, *J Opt Soc Am.*, **30**, 123 (1959)

40 E.J Sussman, R.D Ketchpel, *Final Report JNAIR* no 720903 (1972)

41 T Inoguchi, M Takeda, Y Kakihara, Y Nakata, M Yoshida, *SID Digest*, **5**, 86 (1974)

42. S Mito, C Suzuki, Y Kanatani, M Ise, *SID Digest*, **5**, 86 (1974).

43 T Suntola, J Antson, A Pakkala, S Lindfors, *SID Intern Symp Digest*, 108 (1980)

44 W A Barrow, R.C Coovert, E. Dickey, C N King, C Laakso, S-S Sun, R.T Tuenge R. Wentross, J Kane, *SID Digest*, 761 (1993)

45 D Bosman, *Display Engineering*, North Holland, 223 (1989)

46 G Hass, R.E Thun, *Physics of Thin Films*, **2**, 371 (1963)

47 P D Rack A Naman, P H Holloway, S-S Sun, R.T Tuenge, *MRS Bulletin*, March (1996)

48 Y A Ono, *Electroluminescent Displays*, **1**, 68 (1995)

49 W.E Howard *IEEE Trans on Electron Devices* **ED − 24**, 903 (1977)

50. Y A Ono, *Encyclopedia of Appl Phys*, **5**, VCH Publishers Inc., New York, 1 (1992)

51. H Kobayashi, S Tanaka, V Shanker, M Shiiki, T Kunou, J Mita, H Sasakura, *Phys Stat Solidi* **88**, 713 (1985)

52. S Tanaka, E Deguchi, Y Mikami, M Shiiki, H Kobayashi, *Proc. Int SID Conf*, **28**, 21 (1987)

53. K. Hirabayashi, H Kozawaguchi, E Tsujiyama *Jpn J Appl Phys*, **26**, 1472 (1987)

54. Y A Ono, M Fuyama, K Onisawa, E Tamura, M Ando, *J Appl. Phys*, **66** 5564 (1989)

55. R.T Tuenge, J Kane *SID Digest*, **22**, 279 (1991)

56. R.T Tuenge, *Electroluminescence, Proc. Int. Workshop 6th*, 173 (1992)

57. S Tanaka, K Ohmi, K Yamada, Y Yamano, H. Kobayashi, *Electroluminescence, Proc. Int. Workshop 6th*, 193 (1992)

58. S Tanaka, H Morita, K Yamada, H. Kobayashi, *Proc IDRC*, 137 (1991)

59. R.H Mauch, K O Velthaus, G Hilger, H W Schock, *J Crystal Growth*, **117**, 964 (1992)

60. D Khang, *Appl Phys. Lett.*, **13**, 210 (1968)

61. R. Graeffe, et.al, *Euro Display*, Amsterdam, 84 (1990)

62. S H Sohn, D G Hyun, M Noma, S Hosomi Y Hamakawa, *J Appl Phys*, **72**, 4877 (1992)

63. J.E Bernard, A. Zunger, *Phys Rev. B*, **36**, 3199 (1987)

64. T Taguchi, *Proc. 4th Intern Workshop on Electroluminescence*, Springer proceedings in Physics 38, Springer Heidelberg, (1989)

65. H Kobayashi, *Proc SPIE*, **1910**, 15 (1993)

66 S Tanaka, *J Crystal Growth*, **101**, 958 (1990)

67 A. Hasewaga, A. Yanase, J Phys C *Solid State Phys* , **13**, 1995 (1980)

68 H. Yoshiyama, S H. Sohn, S Tanaka, H Kobayashi *Proc 4th Intern Workshop on Electroluminescence*, Tottori, Springer Heidelberg 38, 48 (1989)

69. N I. Yagubov, T N. Guliev, P G. Rustamov, *Mat Res Bull* , **25**, 271 (1990).

70 R. Eholie, O Gorochov, M Guittard, A. Mazurier, J Flahaut, *Bull Soc Chem. F.*, **3**, 747, (1971)

71 R. Roques, R. Rimet, J P Declercq, G Germain, *Acta Cryst* , **B25**, 555 (1979)

72. F Wooten, *Optical Properties of Solids*, Academic Press, New York (1972)

73 C Kittel, *Introduction to Solid State Physics*, John Wiley and Sons, Inc., New York, (1996)

74 C A. Pan, T P Ma, *Appl Phys Lett.*, **37**, 163, (1980)

75 R.E. Hummel *Electronic Properties of Materials*, Springer Verlag (1985)

76 J A Stratton, *Electromagnetic theory*, McGraw Hill New York (1941)

77 M C Lovell, *Physical Properties of Materials*, Van Nostrand Reinhold Company, 223 (1976)

78 M.L. Cohen, J.R. Chelikowsky, *Electronic Structure and Optical Properties of Semiconductors*, Springer Verlag 43 (1989)

79 H F Wolf, *Semiconductors*, John Wiley and Sons, New York, 52 (1971)

80. M C Lovell, *Physical Properties of Materials*, Van Nostrand Reinhold Company, 247 (1976)

81. P Pringsheim, M Vogel, *Luminescence of Liquids and Solids and its Practical Applications*, Interscience Publishers Inc., New York (1943)

82 G C Guilbault, *Practical Fluorescence Theory Methods and Techniques*, Marcel Decker Inc New York (1973)

83 S G Schulman, *Molecular Luminescence Spectroscopy, Chemical Analysis Series*, John Wiley and Sons, Inc., New York, **77** (1985)

84 J.I Pankove, *Electroluminescence, Topics in Applied Physics Series*, **17**, Springer Verlag, Berlin (1989)

85 O S Heavens, *Optical Constants of Thin Solid Films*, Dover Publications, New York (1965)

86. G R Fowles, *Introduction to Modern Optics*, Holt, Rinehart and Winston, New York (1975)

87 T Timusk, D B Tanner *Physical Properties of High T_c Superconductors*, World Scientific Publishing Co , Singapore, 1, 339 (1989)

88 H E Bennett, J M Bennett, *Precision Measurements in Thin Film Optics* (1967)

89 H E. Bennett, W B Koehler, *J Opt. Soc. Am.*, **50**, 1 (1960)

90 J E Stewart, *Infrared Spectroscopy*, Marcell Dekker Inc., New York, 302 (1970)

91. M I Flik, Z.M Zhang, *J Quant Spectr Rad. Transfer*, **47**, 293 (1992)

92 C.D Porter, D.B Tanner, *Int J Infrared and Millimeter Waves*, **4**, 273 (1983)

93. D.B Tanner, R.P McCall, *Appl Opt.*, **23**, 2363 (1984)

94 P Fellget, *J Phys Radium*, **19**, 187 (1958)

95 R.J Bell *Introductory Fourier Transform Spectroscopy* Academic Press, New York (1972)

96 R.L Henry, D B Tanner, *Infrared Physics*, **19**, 163 (1979)

97 L. Genzel, J Kuhl, *Appl. Opt* , **17**, 3304 (1978)

98. E.D Palik, J.R. Stevenson, *U S Naval Research Laboratory*, NRL Report 6177 (1964)

99 Marshall, *Cathodoluminescence of Geological Materials*, Unwin Hyman Ltd Boston (1988)

100 L Ozawa, *Cathodoluminescence Theory and Applications*, VCH Publishers, New York (1990)

101 C K Jorgensen *Orbitals in Atoms and Molecules*, Academic Press, New York, (1962)

102 D John, D.B Tanner, J Kane, P N Yocom, *Bull Am. Phys Soc*, **41**, 750 (1996)

103 J T Edmond, *Brit. J Appl. Phys*, **17**, 979 (1966)

104 A Vasko, *Phys Stat. Sol.*, **8**, K41 (1965)

105 A Vasko, D Lezal, I Srb, *J Non Crystalline Solids*, **8**, 311 (1970)

106 G Burns, *Solid State Physics*, Fla Academic Press, Orlando (1985)

107 J Pankove, *Phys. Rev Lett*, **4**, 456 (1960)

108 G Gobeli, H Y Fan, *Phys Rev*, **119**, 613 (1960)

109 P Rouard, P Bousquet *Progress in Optics*, **4**, 147, (1963)

110 J A VanVechten, T K Bergstresser, *Phys Rev. B*, **1**, 3351 (1970)

111 D Weaire, *Phys Today*, **24**, 17 (1971)

112 B.M. Brown, D E Brodie, *Can J of Phys*, **50** 2591 (1972)

113 A Morimoto, K. Taniguchi, C Hamaguchi, J Nakai, *J Phys Soc. Jap*, **34**, 79 (1973)

114 G.A Thomas, B K Ng, A.J Millis, R.N Bhatt, R.J Cava, E A Rietman, D W Johnson, G P Espinosa, J M Vandenberg, *Phys Rev B* **36** 846 (1987)

115 D.A. Bonn, J.E Greedan, C V Stager, T Timusk, M G Doss, S L. Herr, K Kamaras, C D Porter, D.B Tanner, J M Tarascon, W R. McKinnon, L H Greene, *Phys Rev B* **35**, 8843 (1987)

116 P D Rack *Ph D Thesis*, University of Florida, 95 (1997)

117, M V Klein, *Optics*, John Wiley and Sons, New York (1970)

118. M Born, E. Wolf, *Principle of Optics*, 6th edition, Pergamon press, Oxford (1980)

119 D.A.G Brubbeman, *Ann Phys (Leipzig)*, **24**, 636 (1935)

120 R. Landauer, *J Appl. Opt* , **23**, 779 (1952)

121 J C M Garnett, *Philos Trans R. Soc. London*, **203**, 385 (1904)

122 J Tauc, *Amorphous and Liquid Semiconductors*, Plenum press, New York (1974)

123 A Weber, P Sutter, H Vonkanel, *J Appl. Phys* , **75**, 7448 (1994)

124 E. Shanthi, V Dutta, A Banerjee, K L. Chopra, *J Appl. Phys* , 51, 6243 (1980)

125 R. Latas, K. Michael, M Scherer, *Jap J Appl. Phys.*, **30**, L149 (1991)

126. M Hohmsel, A Mitwalsky, C Mrotzel, *Phys Stat. Sol A* **123**, 461 (1991)

127 S Ashok, P P Sharma, S.J Fonash, *IEE Trans Electron Devices*, **ED – 27**, 725 (1980)

128 J S Mandes, T Rodriguez, *Thin Solid Films* **66**, 183 (1980)

129 K B Sundaram, G K Bhagavat *J Phys D*, **14**, 921 (1981)

130 T Inagaki, J Najikama, Y Nishimura, *Fujitsu Sci Tech J* , **5**, 235 (1969)

131 E Shanthi, *Ph.D Thesis*, IIT, New Delhi, (1981)

132. J C Manifacier, M DeMurcia, J P Fillard, E Vicario, *Thin Solid Films*, **41**, 127 (1977)

133 A Ya. Kuznetsov, *Sov Phys Solid State*, 2, **30** (1960)

134 H K Muller *Phys Stat. Sol.*, **27**, 723 (1968)

135 R.L Weiher, R. P Ley, *J Appl Phys.*, 37, 299 (1966)

136 A Raza, O.P Agnihotri, B K. Gupta, *J Phys D*, **10**, 1871 (1977)

137 S Noguchi, H Sakata, *J Phys D*, **13**, 1129 (1980)

138. C E Wickersham, J Greene, *Phys Stat Sol. A*, **47**, 329 (1978)

139 K Itoyama, *Jap J Appl Phys* , **17**, 1191 (1978)

140 J C Fan, J F Bachner, *J Electrochem. Soc.*, **112**, 1719 (1975)

141 J C Fan, J Bachner, G H Foley, *Appl. Phys Lett.*, **31**, 773 (1977)

142. H W Lehman, R. Widmer, *Thin Solid Films*, **27**, 359 (1975)

143 K.L Chopra, S Major, K Pandya, *Thin Solid Films*, **102**, 1 (1983)

144 M Just, N Mantzer, I. Blech, *Thin Solid Films*, **48**, L19 (1978)

145 W W Molzen, *J Vacuum Science Tech* , **12**, 99 (1975)

146. R. Pommier, C Gril, J Marucchi, *Thin Solid Films*, **77**, 91 (1981)

147 Y Ohhatta, F Shinokki, S Yoshida, *Thin Solid Films*, **59**, 255 (1979)

148. A S Barker, *Phys Rev.*, **132**, 1474 (1965)

149 Y M Gao, P Wu, J Baglio, K Dwight, A. Wold, *Mater Res Bull* , (**24**, 1215 (1989)

150 A Memon, D H Tanner, *Phys Stat. Sol B*, **127**, 49 (1985)

151 Y M Gao, P Wu, J Baglio, K Dwight, A Wold *Mat Res Bull.*, **24**, 1215 (1989)

152 B W Sanders, A.B Kitai, *J Cryst Growth*, **100**, 405 (1990)

153 J K Furdyna, *J Appl Phys* **64** R29 (1988)

154 R.B Bylsma, W M Bedur, J. Kossut, U Debska, D Yoder-Short, *Phys Rev B*, **33**, 8207 (1986)

155 S Tanaka, H Morita, K Yamada, B Kobayashi *SID Conf*, 137 (1993)

156 Y Kaneko, T Koda, *J Crystal Growth*, **86**, 72 (1988)

157 W Kong, F Fogarty, R. Solanky, *Appl. Phys Lett.*, **66**, 4 (1965)

158 K.O Velthaus, R.H Mauch, H W Schock, *Adv Mater Opt Elec*, 2 (1993)

159 F.A. Ponce, R.D Dupuis, S Nakamura, J.A Edmond, *Mater Res Soc Proc.*, Pittsburg, **395** (1996)

160 J.F Nicholls, B Gallagher, B Henderson, C Trager-Cowan, P G Middleton, K P O'Donnell, T S Cheng, C T Foxon, B H.T Chai, *Mater Res Soc Proc*, Pittsburg, **395** (1996)

161 M Mareno, *Acta Cryst.*, **18**, 481, (1965)

162 D John, H.L. Liu, D B Tanner, B H.T Chai *Bull Am. Phys Soc*, **E187**, 203 (1997)

163 A Juza, G Pascher, *J Chem*, **81**, 285 (1956)

164 R. Nitsce, *J Cryst Growth*, **9**, 238 (1971)

165 B J Schulz, *J Cryst Growth*, **59**, 65 (1982)

166 D Langer, S Ibuki, *Phys Rev*, **138**, A809 (1965)

167 H.E Gumlech, R.L Frogner, J C Shaffer, F E. Williams, *J Chem Phys*, **44**, 3929 (1966)

168 J L Merz, R.T Lynch, *Proc Int Conf II-VI Sem. Compds*, New York, 731 (1967)

169 D Blase, M. Katiyar, A B Kitai, *J Appl. Phys.*, **87**, 1492, (1990)

170 R. Tornqvist *Acta Polytech. Scand*, 143 (1983)

BIOGRAPHICAL SKETCH

Dorothy John was born in the city of Trivandrum, India on Jan. 15, 1964. She received her bachelors degree in applied electronics and instrumentation from the University of Kerala, in 1986. After a brief stint with the Nationals Airport Authority of India at the Bangalore Airport, she returned to academics and completed her masters degree in optoelectronics and laser technology from the Cochin University of Science and Technology, India. She was appointed at the Govt. College of Engineering, Trivandrum as Lecturer through the Kerala State Public Service Commission in 1991.

In 1992, Dorothy came to the University of Florida to pursue a doctoral degree in materials science and engineering. She joined Professor David Tanner's research group in the Physics Department as research assistant, in 1993. Her research involved photoluminescent and optical characterization of phosphors and related materials for electroluminescent displays, in research funded by the Phosphor Technology Center of Excellence (PTCOE).

Dorothy is married to John and they have two children, Aksha and Joshua.

I certify that I have read this study and that in my opinion it conforms to acceptable standards of scholarly presentation and is fully adequate, in scope and quality, as a dissertation for the degree of Doctor of Philosophy

Paul H Holloway

Paul Holloway, Chairman
Professor of Materials Science and Engineering

I certify that I have read this study and that in my opinion it conforms to acceptable standards of scholarly presentation and is fully adequate, in scope and quality, as a dissertation for the degree of Doctor of Philosophy

David B Tanner, Cochairman
Professor of Physics

I certify that I have read this study and that in my opinion it conforms to acceptable standards of scholarly presentation and is fully adequate, in scope and quality, as a dissertation for the degree of Doctor of Philosophy

R. E. Hummel

Rolf Hummel
Professor of Materials Science and Engineering

I certify that I have read this study and that in my opinion it conforms to acceptable standards of scholarly presentation and is fully adequate, in scope and quality, as a dissertation for the degree of Doctor of Philosophy

Joseph H Simmons
Professor of Materials Science and Engineering

I certify that I have read this study and that in my opinion it conforms to acceptable standards of scholarly presentation and is fully adequate, in scope and quality, as a dissertation for the degree of Doctor of Philosophy.

Rajiv Singh
Associate Professor of Materials Science and Engineering

I certify that I have read this study and that in my opinion it conforms to acceptable standards of scholarly presentation and is fully adequate, in scope and quality, as a dissertation for the degree of Doctor of Philosophy.

Zhuomin Zhang
Assistant Professor of Mechanical Engineering

This dissertation was submitted to the Graduate Faculty of the College of Engineering and to the Graduate School and was accepted as partial fulfillment of the requirements for the degree of Doctor of Philosophy.

August 1997

Winfred M. Phillips
Dean, College of Engineering

Karen A. Holbrook
Dean, Graduate School